

# Dark photon search via $D^{*0} \rightarrow D^0 A'$ at Belle experiment

**Kindo Haruki**

*School of High Energy Accelerator Science*

*Department of Particle and Nuclear Physics*

*The Graduate University for Advanced Studies, SOKENDAI*



**SOKENDAI**



A thesis submitted for the degree of  
Doctor of Philosophy

December 2021

## Abstract

Existence of invisible massive matter, called Dark Matter, is evident from astronomical observations. Origin of Dark Matter, in the form of elementary particles, is one of the main unanswered questions of astronomy and physics. Despite numerous efforts over decades, such Dark Matter particle is not observed yet.

In this thesis, we focus on Dark Matter in MeV scale which is called Dark Photon, a part of Dark Matter model called Hidden Sector hypothesis, and is predicted to have mixing with Standard Model photon. If the Dark Photon is the lightest particle in Hidden Sector, then Dark Photon becomes Dark Matter, but Dark Photon can also decay into a lighter dark particle. Even if Dark Photon can decay, Dark Photon still be a probe for the Hidden Sector.

We use  $D^{*0} \rightarrow D^0 A' (\rightarrow e^+ e^-)$  decay in data accumulated by Belle experiment to search for the Dark Photon. A process  $D^{*0} \rightarrow D^0 A'$  may occur by a mixing between  $\gamma$  and  $A'$  in  $D^{*0} \rightarrow D^0 \gamma$ . The mass difference between  $D^{*0}$  and  $D^0$  is 142 MeV, so this is suitable to search for MeV scale Dark Photon.

$D^{*0}$  is produced in the hadronization of  $c\bar{c}$  pair. The data taken in Belle experiment on  $\Upsilon(4S)$  resonance is  $711 \text{ fb}^{-1}$  and includes  $1.9 \times 10^9$  of  $c\bar{c}$  events. To reconstruct the events of  $D^{*0} \rightarrow D^0 A' (\rightarrow e^+ e^-)$  and  $D^{*0} \rightarrow D^0 \gamma$ , we used three decay modes of  $D^0$ ;  $D^0 \rightarrow K^- \pi^+$ ,  $D^0 \rightarrow K^- \pi^+ \pi^0$ , and  $D^0 \rightarrow K^- \pi^+ \pi^- \pi^0$ . The reconstructed  $D^0$  meson is combined with a pair of electron and positron or  $\gamma$  to reconstruct  $D^{*0}$ . After the reconstruction of  $D^{*0}$ ,  $A'$  is reconstructed from the pair of electron and positron. If  $A'$  exists, the distribution of  $m_{A'}$  should have a peak at finite mass, not 0. Using the  $D^{*0} \rightarrow D^0 \gamma$  decay as the normalization mode, we measure the ratio  $R$  between  $D^{*0} \rightarrow D^0 \gamma$  and  $D^{*0} \rightarrow D^0 A'$ .

The  $m_{A'}$  distributions of three  $D^0$  decay modes are fitted simultaneously, using the ratio  $R$  as a common parameter. Since the mass of  $A'$  is unknown, mass scan over  $12 < m_{A'} < 120 \text{ MeV}/c^2$  is performed. No significant evidence of Dark Photon is found and upper limits of the order of  $10^{-4}$  are set on the ratio  $R$ .

Dark Photon is not observed in this analysis. But, a new upper limit is set to  $D^{*0}$  mode.

# Contents

<b>1</b>	<b>Introduction</b>	<b>4</b>
<b>2</b>	<b>Physics Motivation</b>	<b>6</b>
2.1	Standard model . . . . .	6
2.2	Dark sector hypothesis . . . . .	7
2.2.1	Features and candidates of Dark Matter . . . . .	7
2.2.2	Hidden sector hypothesis . . . . .	9
2.2.3	Theories of Dark Photon . . . . .	10
2.3	Previous search for Dark Photon at low energy scale . . . . .	10
2.3.1	Beam dump experiments . . . . .	11
2.3.2	Collider experiments . . . . .	12
2.4	Beryllium anomaly . . . . .	13
2.5	Search for dark photon by $D^{*0} \rightarrow D^0 A'$ decay . . . . .	14
<b>3</b>	<b>Belle experiment</b>	<b>16</b>
3.1	KEKB accelerator . . . . .	16
3.1.1	The structure of LINAC . . . . .	16
3.1.2	Main rings . . . . .	17
3.1.3	The interaction point . . . . .	18
3.1.4	Magnets to control the beams . . . . .	18
3.2	Belle spectrometer . . . . .	19
3.2.1	Silicon Vertex Detector . . . . .	20
3.2.2	Central Drift Chamber . . . . .	22
3.2.3	Aerogel Cherenkov Counter . . . . .	24
3.2.4	Time of Flight Counter . . . . .	26
3.2.5	Electromagnetic Calorimeter . . . . .	27
3.2.6	$K_L/\mu$ detector . . . . .	28
3.3	Trigger and Data Acquisition . . . . .	29
<b>4</b>	<b>Event Processing and Monte Carlo Simulation</b>	<b>32</b>
4.1	Data sets . . . . .	32
4.2	Event processing framework . . . . .	32
4.3	Event reconstruction . . . . .	33

4.3.1	Charged particle tracking . . . . .	33
4.3.2	Neutral particle reconstruction . . . . .	34
4.3.3	Particle Identifications . . . . .	35
4.4	Hadronic event selection . . . . .	40
4.5	MC simulation . . . . .	40
4.5.1	Event generation . . . . .	40
4.5.2	Detector simulation . . . . .	41
4.5.3	The sample types of background MC . . . . .	42
4.5.4	Tracing the MC informations . . . . .	42
<b>5</b>	<b>Signal Reconstruction</b>	<b>43</b>
5.1	Signal mode $D^{*0} \rightarrow D^0 A'$ . . . . .	43
5.1.1	Signal and normalization modes . . . . .	43
5.1.2	Measurement of $R$ . . . . .	44
5.1.3	Decay length of $A'$ . . . . .	44
5.2	Signal MC Samples . . . . .	45
5.3	Signal Event Reconstruction . . . . .	45
5.3.1	Criteria for particle identification . . . . .	45
5.3.2	$D^0$ reconstruction . . . . .	46
5.3.3	$D^{*0}$ reconstruction . . . . .	47
5.4	Background Suppression . . . . .	48
5.4.1	FoM for the optimization of selection criteria . . . . .	49
5.4.2	Contamination of $D^{*+} \rightarrow D^0 \pi^+$ . . . . .	50
5.4.3	Contamination of $D^{*0} \rightarrow D^0 + \pi^0/\gamma$ . . . . .	52
5.4.4	Mass constraint vertex fit on $D^{*0}$ . . . . .	53
5.5	Best candidate selection . . . . .	55
5.6	Selection summary . . . . .	56
5.7	The reconstruction of normalization mode $D^{*0} \rightarrow D^0 \gamma$ . . . . .	57
5.7.1	$D^0$ reconstruction . . . . .	57
5.7.2	$D^{*0}$ reconstruction . . . . .	58
5.8	The background $D^{*0} \rightarrow D^0 e^+ e^-$ process . . . . .	58
5.8.1	The decay of $D^{*0} \rightarrow D^0 e^+ e^-$ in the Standard Model . . . . .	58
5.8.2	Differences from the signal mode . . . . .	59
<b>6</b>	<b>Estimation of signal yield by MC simulation</b>	<b>61</b>
6.1	Signal shape and efficiencies . . . . .	61
6.2	Background estimation . . . . .	61
6.3	Extraction of signal yield . . . . .	63
6.4	Fit stability . . . . .	63
6.4.1	Toy MC . . . . .	63
6.4.2	Validation with Toy MC method . . . . .	64
6.4.3	Check of fit stability . . . . .	64
6.5	Yield estimation of $D^{*0} \rightarrow D^0 \gamma$ . . . . .	65

6.6	Branching fraction calculation by the simultaneous fit in MC . . . . .	67
6.7	$A'$ mass dependence of parameters . . . . .	69
<b>7</b>	<b>Systematic Uncertainty</b>	<b>74</b>
7.1	Breakdown of the systematics . . . . .	74
7.2	The efficiencies of $e^+e^-$ . . . . .	75
7.3	$\gamma$ finding efficiency . . . . .	75
7.4	$e^+e^-$ vertex selection efficiency . . . . .	75
7.5	$\chi^2$ probability selection efficiency . . . . .	76
7.6	Summary of proportional systematics . . . . .	79
<b>8</b>	<b>Data Analysis</b>	<b>80</b>
8.1	Reconstruction of $D^0$ in data . . . . .	80
8.2	The yield of the normalization mode in data . . . . .	81
8.3	Results for data . . . . .	82
8.3.1	Reconstruction of $D^{*0}$ and $A'$ . . . . .	82
8.3.2	Result of simultaneous fit to the data . . . . .	83
8.4	Upper limit with systematic uncertainties . . . . .	86
<b>9</b>	<b>Result and discussion</b>	<b>88</b>
9.1	Mass scan for data . . . . .	88
9.2	Discussion . . . . .	88
<b>10</b>	<b>Conclusion</b>	<b>92</b>
<b>A</b>	<b>Appendix</b>	<b>94</b>
A.1	Efficiency of charged particle selection . . . . .	94
A.2	The PDF of $D^{*0} \rightarrow D^0 e^+ e^-$ mode . . . . .	94

# Chapter 1

## Introduction

The existence of Dark Matter, the invisible matter which interacts with matter in the universe through the gravitational force, is predicted from astronomical observations and cosmological theories.

The first indication of Dark Matter was seen in discrepancies in the movement of celestial objects between observation and theoretical prediction. In early 1930s, J. H. Oort measured the movement of stars in Milky Way Galaxy using Doppler shift and found that their velocities are high enough to escape from the gravitational force made by all visible objects in the galaxy [1]. F. Zwicky also found that the total mass of a galaxy in Coma cluster predicted from its luminosity was a few percent of the mass calculated from the virial theorem and the movement of stars in the galaxy [2], [3]. However, these results were not considered to be important at that time.

About 40 years later, V. C. Rubin and her colleagues studied the relation between the velocities of stars and the distance from galactic center for 60 isolated galaxies [4]. The velocity should decrease as the distance increases, if the source of gravity is only from visible stars and interstellar gases. But the velocity is observed to have a flat distribution.

The observations above can be explained by a hypothesis that there are invisible and massive matter broadly in galaxies, which dominate the mass of galaxies. This invisible and massive matter is called Dark Matter, and it is one of the major problems in astronomy and physics.

After this hypothesis is proposed, many experiments have tried to find Dark Matter. Collider experiments such as LHC experiments [5] and Belle II [6] search for Dark Matter candidates to be produced in the particle reactions at the highest energy and at the highest luminosity. Another approach is to detect elastic scattering of dark matter particles of nuclei. The search has been performed by experiments such as DAMA [7], XENON [8], and CDMS [9]. Despite these efforts, Dark Matter is not observed yet.

The energy region of the previous search was mainly focused on the high energy range from GeV to TeV order which is favored especially Weakly Interacting Massive Particles (WIMPs) models including supersymmetry as a candidate. WIMP is one of the most studied candidate of Dark Matter and its mass is predicted not to be significantly higher than  $m_{\text{weak}} \sim 10 \text{ GeV} - \text{TeV}$ . However, 7 TeV  $pp$  collision in LHC shows negative results of the searches for WIMPs.

In contrast, the models less than GeV scale Dark Matter like Dark Sector, axion etc. are not well explored. The mass of axion (less than  $\mu\text{eV}/c^2$ ) is too small to search in collider experiments, but Dark Sector ( $\text{keV}/c^2$  -  $\text{GeV}/c^2$ ) is reachable.

Dark Sector is predicted to have its own symmetries and structure like Standard Model and particles in Dark Sector are predicted to have mixing with the counterparts in Standard Model, for example, the Dark Photon has mixing with Standard Model photon. The feature that Dark Sector is not just an extension of the Standard Model, but has its own symmetries, is both an advantage and a disadvantage of Dark Sector. Most Dark Sector models don't give solutions for the other problems of Standard Model like strong CP problem which can be solved by axion. At the same time, the feature enables to explain the density difference between the visible and dark matters. For the mass region of Dark Sector, a new possibility is proposed in 2012 by the observation of excited Beryllium nucleus [10], which is a new particle at  $17 \text{ MeV}/c^2$  mixing with Standard Model photon, called  $X(17)$ . Given the feature of  $X(17)$  of mixing with SM photon, Dark Photon is a possible candidate to explain it.

The search for Dark Photon, suggested by the Beryllium experiment has been carried out for the decay of light particles only with  $u$ ,  $d$ , and  $s$  quarks. For example, the NA48/2 experiment at CERN SPS searches for  $\pi^0 \rightarrow \gamma A' (\rightarrow e^+e^-)$  [11]. The searches using heavier quarks ( $c$  and  $b$ ) are done by the LHCb experiment only in high mass region ( $> \text{GeV}/c^2$ ). However, all the previous searches show negative results.

The Belle experiment is one of the collider experiments to search physics beyond the Standard Model. The Belle experiment had been operated from 1999 to 2010 and the integrated luminosity is about  $1 \text{ ab}^{-1}$ . The sample accumulated by the Belle experiment includes  $\mathcal{O}(10^9)$  events of  $B\bar{B}$  and similar amount of  $q\bar{q}$  ( $q = u, d, s, c$ ). The high statistics sample can be utilized for the search of Dark Photon which is considered to be rarely produced.

One of the advantages of Belle experiment compared to previous experiments is that  $c$  quark can be used as the source of Dark Photon. Another advantage is that Belle is an  $e^+e^-$  collider experiment where the reaction is much clean and the reachable mass range is lower than that of LHCb which is a  $pp$  collider experiment.

In this thesis, the analysis is performed using the  $D^{*0}$  mesons in the Belle data. Dark Photon is searched for in the decays of  $D^{*0}$  where the search in the low mass scale in the range of 10 to 100  $\text{MeV}/c^2$  is possible.

# Chapter 2

## Physics Motivation

Here, we review Standard Model and the hypotheses of Dark Matter, and discuss the detection method of our search.

### 2.1 Standard model

Standard Model (SM) describes the behavior of the elementary particles and fundamental interactions based on the gauge invariance of the  $U(1)_Y \times SU(2)_L \times SU(3)_c$  group. Standard Model includes 12 fermions, 4 gauge bosons, and 1 Higgs boson.

Table 2.1: Summary of the fermions. S, B, L, and Q are spin, baryon number, lepton number, and electric charge, respectively.

	1st gen.	2nd gen.	3rd gen.	S	B	L	Q
Quarks	$u$	$c$	$t$	$\frac{1}{2}$	$\frac{1}{3}$	0	$+\frac{2}{3}$
	$d$	$s$	$b$	$\frac{1}{2}$	$\frac{1}{3}$	0	$-\frac{1}{3}$
Leptons	$e$	$\mu$	$\tau$	$\frac{1}{2}$	0	1	-1
	$\nu_e$	$\nu_\mu$	$\nu_\tau$	$\frac{1}{2}$	0	1	0

The fermions are summarized in table 2.1. There are 12 fermions consisting of 6 quarks and 6 leptons. Both compose 3 generations. And there are 4 fundamental; gravitational, electromagnetic, strong, and weak interactions. All the quarks and leptons except the neutrinos couple with the electromagnetic interaction. While quarks couple with strong and weak interactions, leptons couple with only weak interaction. Bosons in the SM are listed in table 2.2 which intermediate the interactions. The gauge bosons mediate the interactions; photons for electromagnetic, weak bosons for weak, and gluons for strong interactions.

Higgs boson discovered in 2012 by ATLAS [12] and CMS [13] experiments at Large Hadron Collider (LHC) is considered to be the origin of particle mass through the Higgs mechanism.

Standard Model successfully explains the nature of this universe. However, not all the problems are solved by SM. For example, the neutrino oscillation [14] shows that the neutrinos

Table 2.2: Summary of the bosons. S and Q are spin and electric charge.

		S	Q
Photon	$\gamma$	1	0
Weak boson	$\begin{pmatrix} W^+ \\ W^- \end{pmatrix}$	1	$\begin{pmatrix} +1 \\ -1 \end{pmatrix}$
Weak boson	$Z^0$	1	0
Gluon	$g$	1	0
Higgs boson	$\phi$	0	0

have mass, although they are massless particles in the SM.

The baryogenesis is also an unsolved problem. Only baryons are observed in our universe, while in the SM, baryons and anti-baryons are, with a few exceptions, always produced as a pair so that the baryon number is conserved. To explain this contradiction, Sakharov proposed three conditions in 1967, requiring baryon number violation, violations of charge conjugation symmetry and charge conjugation parity symmetry (C and CP violation), and a departure from thermal equilibrium [15]. The CP violation described in Kobayashi-Maskawa theory [16] is one of the exceptions to the baryon number conservation, but it is several orders of magnitude smaller than what explains the baryogenesis.

Another example is Dark Matter (DM) and Dark Energy. As mentioned in the previous chapter, from the cosmology and astronomy view point, observations of the celestial objects like motions of galaxies suggest invisible and gravitational matters. In recent years, the existence of DM has been reinforced by further observations of gravitational lensing. The Dark Energy is a hypothetical energy which accelerates the expansion of the universe against the gravity of Standard Model Matters and Dark Matters. In this universe, the fraction of Standard Model matters is only 5% while the others are 25% of Dark Matter and 70% of Dark Energy.

To explain Dark Matter and Dark Energy, a new theory beyond SM (BSM) is necessary.

## 2.2 Dark sector hypothesis

In this section, we focus on the theoretical explanation of Dark Matter, one of the hypotheses called Dark Sector. First, we review the features of Dark Matter and major hypotheses. Then, the theory of Dark Sector is introduced.

### 2.2.1 Features and candidates of Dark Matter

In the particles of Standard Model, we may consider neutrinos as a candidate of DM. In Standard Model, neutrinos are assumed to be massless particles, but actual observations show that they do have mass. The fact that they couple only to weak interaction and have mass makes them candidates for "hot" Dark Matter [17]. However, astronomical observations

demonstrated that the total mass of neutrinos in the universe is not enough to explain Dark Matter. WMAP made the full sky temperature and polarization map (Fig. 2.1) based on seven years observation of microwave from the space between the celestial objects [18]. The data are fitted with the minimal six-parameter  $\Lambda$ CDM model, and the parameter indicating the density of neutrino in the universe  $\Omega_\nu h^2$  is favored to be smaller than 0.014 at 95% C.L. while the density parameter of Dark Matter  $\Omega_c h^2$  is  $0.1109 \pm 0.0056$  where  $\Omega_i$  is the ratio of actual density to the critical density  $\rho_c = 8.5 \times 10^{-27} \text{ kg/m}^3$  and  $h$  is reduced Hubble parameter  $h = H_0/100$ . The result indicates the total mass of neutrino is less than 15% of Dark Matter.

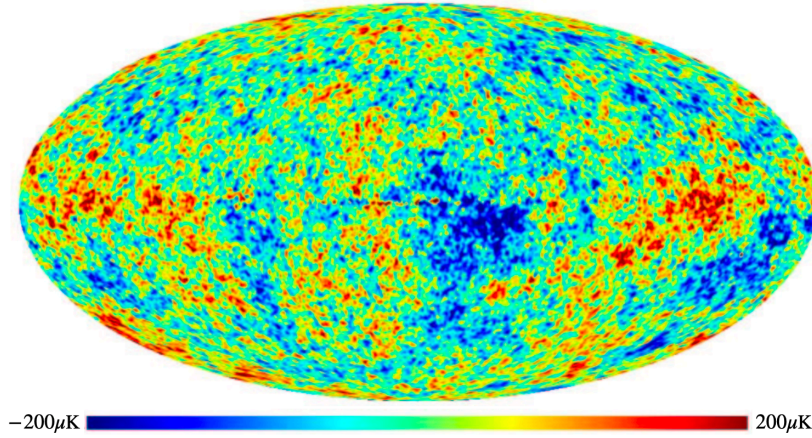


Figure 2.1: The temperature map of CMB based on 7 years observation of WMAP [19].

Since the particles in Standard Model can not explain Dark Matter, Standard Model needs extension to include Dark Matter particles. Many theoretical models are proposed and candidates of Dark Matter are included in each model with suitable interaction. There is a wide range of theoretical hypotheses.

An example is the SuperSymmetry (SUSY) model. It is an extension of Standard Model by adding a new symmetry between bosons and fermions [20], and it introduces new fundamental particles called superpartners (sparticles) as shown in Fig. 2.2. If supersymmetry is unbroken, Standard Model particles and their superpartners have the same mass and quantum numbers except spin. The symmetry is supposed to be broken spontaneously and sparticles can have different mass. The sparticles decay into the lighter sparticles in short time. Only the lightest particle (Lightest SParticle, LSP) can be stable. Candidates of LSP are the mixtures of neutral superpartners called neutralinos; bino+neutral wino or photino+zino. If the neutralino is the lightest sparticle, it can be a candidate of Dark Matter at a low mass scale (sub-TeV/ $c^2$ ).

Another example is an axion. The axion is proposed to solve the strong-CP problem by R. Peccei and H. Quinn in 1977 [22]. The new symmetry (called Peccei-Quinn symmetry) keeps axion to be massless. The spontaneous breaking of Peccei-Quinn symmetry makes axion massive at  $\mu\text{eV}/c^2$  order. Axion couples with SM via the electromagnetic interaction weakly and can be a candidate of Dark Matter.

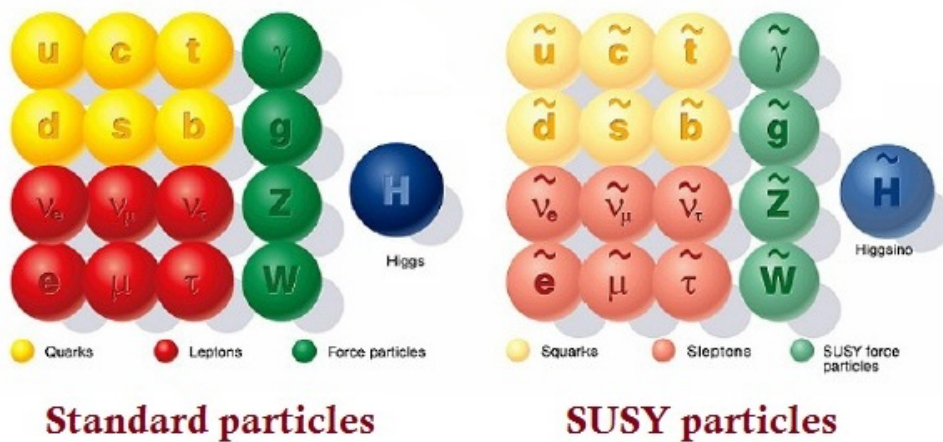


Figure 2.2: The table of superpartners. Standard Model particles are in left, and corresponding superpartners with “ $\sim$ ” symbols on top are in right [21].

### 2.2.2 Hidden sector hypothesis

The Hidden Sector hypothesis has a long history, going back to the idea of the existence of left-handed and right-handed protons ( $p_L$  and  $p_R$ ) in the parity symmetry breaking [23]. The hidden sector is a collection of particles similar to Standard Model which has their own symmetries independent of Standard Model. The particles in the hidden sector do not

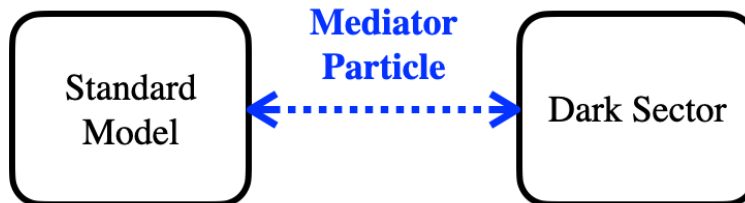


Figure 2.3: The concept of Dark Sector. Independent collections of particles are connected by a lighter mediator particle.

interact with Standard Model particles directly, but there are some portals acting as indirect interaction; scalar, vector, and neutrino. The scalar portal connects Standard Model Higgs to the hidden sector particles, while the vector portal to photons, and neutrino portal to neutrinos.

The target of our analysis is this photon interacting through the vector portal called Dark Photon ( $A'$ ) as shown in Fig. 2.4. Dark Photons are produced by annihilation of Dark Sector particles and couple to Standard Model bosons. Note that the mass of Dark Photon is unknown and allowed to be in from  $\text{neV}/c^2$  to  $\text{TeV}/c^2$  scale. The hidden sector is also favored by the string theory [24] and the other BSM like asymmetric dark matter [25].

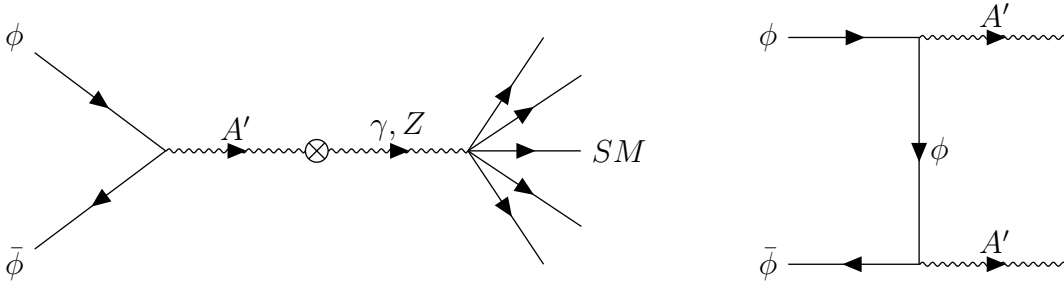


Figure 2.4: The annihilation of Dark Sector particle  $\phi$  into the vector mediator  $A'$  which couples to Standard Model bosons for: (A) regardless of the relation between  $m_\phi$  and  $m_{A'}$  on the left; and (B)  $m_\phi > m_{A'}$  on the right. The cross dot vertex shows the kinetic mixing.

### 2.2.3 Theories of Dark Photon

Dark Photon  $A'$  is a new abelian  $U(1)$  gauge boson mediating a new force and coupling very weakly to electrically charged particles through the "kinetic mixing" [26].

The coupling of  $A'$  to electromagnetic current  $J_{EM}^\mu$  produced by the kinetic mixing is written as

$$\mathcal{L} \supset -\frac{1}{4}F'_{\mu\nu}F'^{\mu\nu} + \frac{1}{2}m_{A'}^2 A'_\mu A'^\mu + \epsilon e A'_\mu J_{EM}^\mu \quad (2.1)$$

where  $F_{\mu\nu}$  is electromagnetic tensor,  $m_{A'}$  is the mass of  $A'$  and  $\epsilon$  is the mixing parameter. The interaction between Standard Model electromagnetic current and Dark Photon is in the third term, that is suppressed by the mixing parameter  $\epsilon$  and the electron charge  $e$ .

Key parameters of Dark Photon are its mass  $m_{A'}$  and the mixing parameter  $\epsilon$  that gives the actual coupling between  $A'$  and Standard Model bosons ( $\gamma$  and  $Z$ ) and vector mesons ( $\rho$ ,  $\phi$  and  $\omega$ ). The both parameters are not constrained by theories because the vector portal is a four-dimensional operator and unsuppressed at any high mass scale.

The mass of Dark Photon which arises via Higgs mechanism can be  $\text{MeV}/c^2$  -  $\text{GeV}/c^2$  or higher with  $\epsilon \sim 10^{-8} - 10^{-3}$ , which is favored by SUSY [27], [28]. The mass in the order of  $\text{meV}/c^2$  is also allowed when the mass arises via Stückelberg mechanism with  $\epsilon \sim 10^{-12} - 10^{-3}$ , which is favored by string theories [29]. Recently, the mass limit is extended down to  $10^{-20}$   $\text{eV}/c^2$  order [30]

## 2.3 Previous search for Dark Photon at low energy scale

Current constraints from previous experiments are summarized in Fig. 2.5.

There are two kinds of experiments which give the constraints shown in Fig. 2.5; the beam dump experiments (in the left bottom region) and the others (in the top region). The difference is in the generation mechanism of Dark Photon, which is shown later.

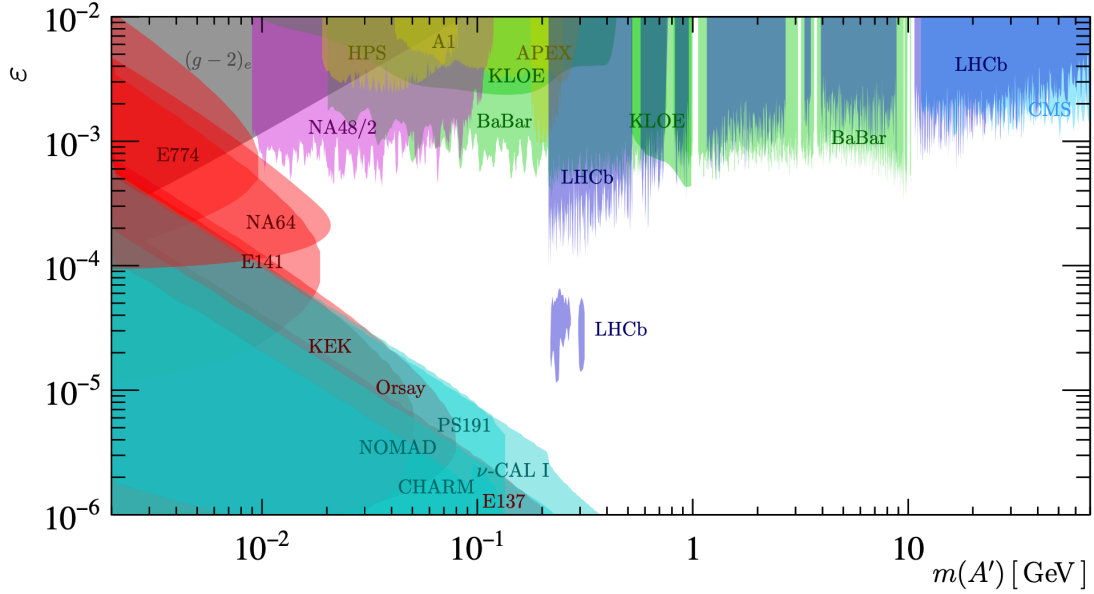


Figure 2.5: Current experimental constraints at 90% C.L. of  $\epsilon$  as a function of  $m_{A'}$  [31]. Red and cyan show the proton and electron beam dump [32]–[42], grey shows the magnetic moment of electron  $(g - 2)_e$  [43], green shows  $e^+e^-$  colliders [44]–[46], blue shows  $pp$  colliders [31], magenta shows meson decays [11], and yellow shows the electron on fixed target experiments.

### 2.3.1 Beam dump experiments

In the beam dump experiments, Dark Photon is generated by bremsstrahlung of electron or proton similar to Standard Model photon. The concept of beam dump experiments is illustrated in Fig. 2.6, which is focused on the displaced decay. The principle is same in all experiments.

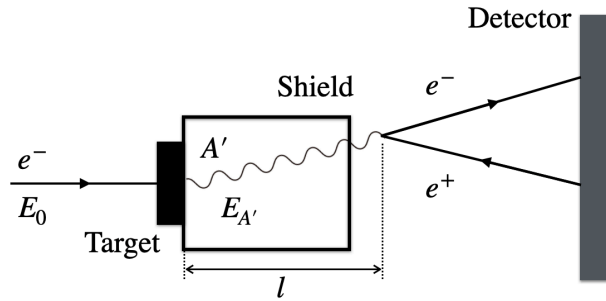


Figure 2.6: The concept picture of electron beam dump experiments.

The advantage of this type experiment is that it is possible to gain much larger statistics with a high luminosity beam, which allows the search region to reach down to  $\epsilon = 10^{-7}$ . However, a thick shield to stop the beam is required before the detector, and only  $A'$  with a long decay length can be detected. It limits the search region only to the left bottom in Fig. 2.5.

### 2.3.2 Collider experiments

Another type of Dark Photon search is to study the decay of Standard Model particles produced in the collider experiments. The concepts of collider experiments are illustrated in Fig. 2.7, which can detect both of the prompt and displaced decays. Dark photons can be produced either by a beam collision directly (case *a* in Fig. 2.7) or by a decay of SM particles produced in the beam collision (case *b* in Fig. 2.7).

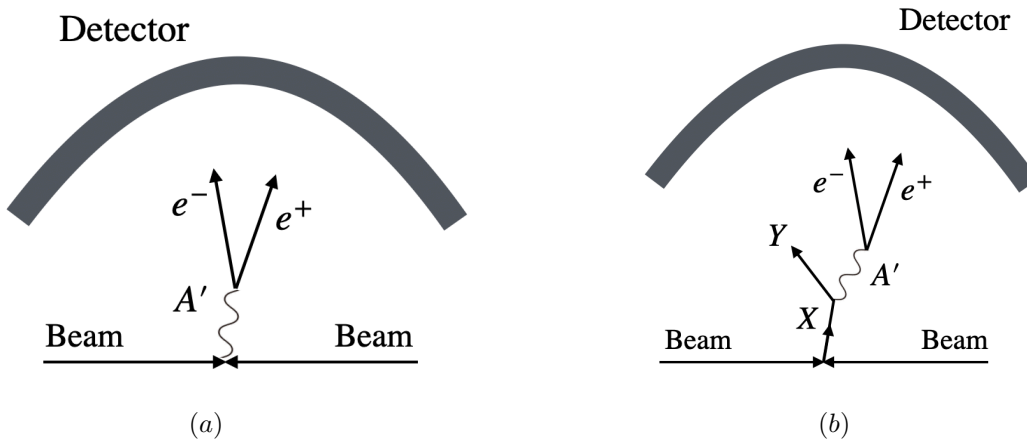


Figure 2.7: The concept picture of collider experiments; (a) Dark Photon is produced from beam collision directly, (b) Dark Photon is a daughter particle of the products of collision.

NA48/2 is a fixed target experiment at CERN SPS, searching for  $\pi^0 \rightarrow \gamma A' (\rightarrow e^+ e^-)$  [11]. It is not a collider experiment, but the generation mechanism is the same as the case *b* in Fig. 2.7, so it is described here. The protons at 400 GeV/*c* injected in a Beryllium target generate a charged kaon beam. The search is performed using  $K^\pm \rightarrow \pi^\pm \pi^0$  and  $K^\pm \rightarrow \pi^0 \mu^\pm \nu$  decays. The upper limit of  $\epsilon$  is given in the region of  $8 \text{ MeV}/c^2 < m_{A'} < 120 \text{ MeV}/c^2$  and is the most stringent in  $9 < m_{A'} < 70 \text{ MeV}/c^2$ .

BaBar is an  $e^+e^-$  collider experiment at SLAC and the search for  $e^+e^- \rightarrow \gamma A' (\rightarrow l^+ l^-)$  ( $l = e, \mu$ ) is performed [44]. The search region is from 20 MeV/ $c^2$  to 10.2 GeV/ $c^2$  and BaBar gives the most stringent limits for over 70 MeV/ $c^2$  region.

KLOE is an  $e^+e^-$  collider experiment in LNF and searches for  $\phi \rightarrow \eta A' (\rightarrow e^+ e^-)$ ,  $e^+e^- \rightarrow \gamma A' (\rightarrow e^+ e^-)$ , and  $e^+e^- \rightarrow \gamma A' (\rightarrow \pi^+ \pi^-)$  [45], [46]. The search region is in 527 - 987 MeV/ $c^2$  and KLOE improves the results of BaBar in 700 MeV/ $c^2$  - 1GeV/ $c^2$  region.

LHCb is a  $pp$  collider experiment in CERN and search for inclusive  $pp \rightarrow A'$  [31]. Since proton is a composite particle, there are many production processes of  $A'$  as summarized in Fig. 2.8. The mothers of  $A'$  are vector mesons ( $\eta, \omega, \rho$ , and  $\phi$ ) and  $u\bar{u}$  pair below 1 GeV/ $c^2$ .  $A'$  decay modes used for the search are summarized in Fig. 2.9. The search region of LHCb is over 210 MeV/ $c^2$ , because only  $A' \rightarrow \mu^+ \mu^-$  process is used. LHCb gives the stringent limit in 210 - 800 MeV/ $c^2$  region.

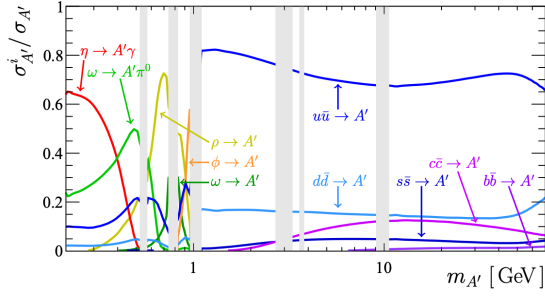


Figure 2.8: Dark Photon production fractions for the important processes at LHCb from [47]

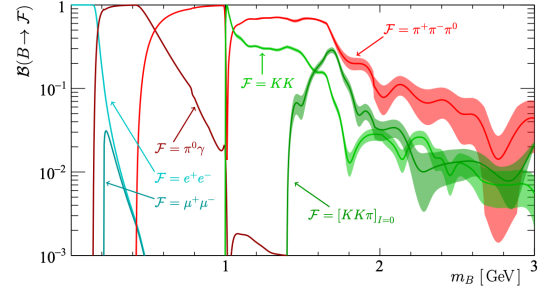


Figure 2.9: Dark Photon decay fractions below  $3 \text{ GeV}/c^2$  at LHCb from [47]. Note that  $A'$  is called as "B-boson" and  $m_{A'}$  is written as  $m_B$  here.

## 2.4 Beryllium anomaly

In 2012, A. Krasznahorkay *et al.* observed a strange phenomena in excited Beryllium nucleus with Atomki spectrometer [10], which indicates an unknown particle  $X$  in  ${}^8\text{Be}^* \rightarrow {}^8\text{Be} + X$ .

The sketch of the experiment is shown in Fig. 2.10. Lithium nucleus exposed in the proton beam are turned into excited Beryllium nucleus  ${}^8\text{Be}^*$ , which subsequently decays into the ground state of Beryllium  ${}^8\text{Be}$  and  $X$ .  $X$  decays into an electron-positron pair. The experiment measures the opening angle  $\theta$  and invariant mass  $m_{ee}$  of the electron-positron pair which is produced by the internal pair creation (IPC) from  $\gamma$  emitted in the transition from excited state to ground state of Beryllium nucleus.

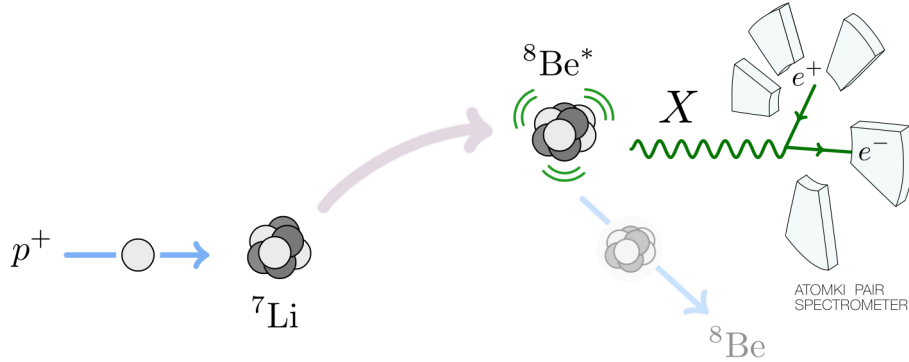


Figure 2.10: Sketch of the Atomki spectrometer and its experiment.

This IPC is ruled by the electric and magnetic parities and angular momentum. For all the electric and magnetic transition in SM, the spectra of opening angles and invariant masses of the electron-positron pairs are known to be monotonically decreasing.

Their result shows a bump in  $\theta$  spectrum (Fig. 2.11). The source of the bump is considered to be an interference between the non-resonant and resonant states, but found it cannot be explained by the known physics effects.

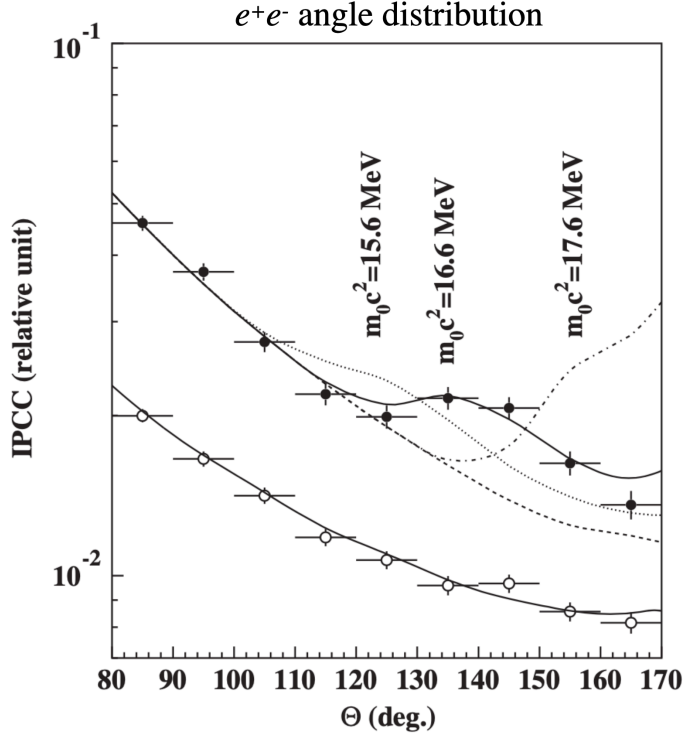


Figure 2.11: The spectrum of the electron-positron opening angle  $\theta$  in Ref. [10]. The closed circle are  $|y| \leq 0.5$  results and the open circle are  $|y| > 0.5$  results where  $y = \frac{E_{e^-} - E_{e^+}}{E_{e^-} + E_{e^+}}$ . For the black dots, the dashed line is SM expectation and the solid line is  $m_X = 16.6 \text{ MeV}/c^2$  expectation.

The bump can be explained if a massive particle  $X$  is produced in the Beryllium nuclei with low velocity and decays into an electron-positron pair. With the fixed IPC backgrounds, they find the best fit mass and the branching fraction on  $X$  are given to be

$$m_X = 16.7 \pm 0.35(\text{stat}) \pm 0.5(\text{sys}) \text{ MeV}/c^2 \quad (2.2)$$

$$\frac{\Gamma(^8\text{Be}^* \rightarrow ^8\text{Be}X)}{\Gamma(^8\text{Be}^* \rightarrow ^8\text{Be}\gamma)} B(X \rightarrow e^+e^-) = 5.8 \times 10^{-6}. \quad (2.3)$$

This new particle, called  $X(17)$ , couples to a Standard Model photon weakly and is a candidate of Dark Photon.

## 2.5 Search for dark photon by $D^{*0} \rightarrow D^0 A'$ decay

We use  $D^{*0} \rightarrow D^0 A'$  decay to search for Dark Photon in this analysis.

A decay  $D^{*0} \rightarrow D^0 A'$  can occur through the mixing between  $\gamma$  and  $A'$  in  $D^{*0} \rightarrow D^0 \gamma$ . The mass difference  $\Delta m \equiv m_{D^{*0}} - m_{D^0}$  is  $142 \text{ MeV}/c^2$ , and it is suitable to search for  $\text{MeV}/c^2$  scale Dark Photon including  $X(17)$ .

Note that charge-conjugate states are always implied through this thesis.

Since Dark Photon couples to  $J_{EM}^\mu$  with the mixing parameter  $\epsilon$  (Eq. 2.1), the matrix element of  $D^{*0} \rightarrow D^0 A'$  can be written in a similar way to that in the SM decay:

$$\langle D^{*0} | \epsilon J_{EM}^\mu | D^0 \rangle = \epsilon \mu_{eff}(k^2) \epsilon^{\mu\alpha\beta\lambda} v_\alpha k_\beta \epsilon_\lambda \quad (2.4)$$

where  $v_\alpha$  is the four momentum of  $D^{*0}$ ,  $k_\beta$  is the momentum flowing out of the current, and  $\epsilon_\lambda$  is the polarization of  $D^{*0}$ , and  $\mu_{eff}$  is the effective dipole moment depending on  $k$ . The value of  $\mu_{eff}$  can be determined by heavy meson chiral perturbation theory [48]. Since  $\Delta m^2 < \Lambda_{QCD}^2$  where  $\Lambda_{QCD}$  is the energy scale of QCD and  $\Lambda_{QCD} = 213 \pm 9$  MeV [49],  $\mu_{eff}$  can be treated as a constant in the range of  $k^2 < \Delta m^2$ . From Eq. 2.4, the decay width of  $D^{*0} \rightarrow D^0 A'$  is given as

$$\Gamma(D^{*0} \rightarrow D^0 A') = \epsilon^2 \frac{\alpha_{EM}}{3} \mu_{eff}^2 (\Delta m^2 - m_{A'}^2)^{3/2}. \quad (2.5)$$

assuming  $m_{A'}, \Delta m_D \ll m_D$ . The matrix element of  $D^{*0} \rightarrow D^0 \gamma$  is the same as that in Eq. 2.1, and the decay width of  $D^{*0} \rightarrow D^0 \gamma$  can be written as

$$\Gamma(D^{*0} \rightarrow D^0 \gamma) = \frac{\alpha_{EM}}{3} \mu_{eff}^2 \Delta m^3. \quad (2.6)$$

Taking the ratio of these decays, the mixing parameter  $\epsilon$  can be related to the ratio as

$$R = \frac{\Gamma(D^{*0} \rightarrow D^0 A')}{\Gamma(D^{*0} \rightarrow D^0 \gamma)} = \epsilon^2 \left(1 - \frac{m_{A'}^2}{\Delta m^2}\right)^{3/2} \quad (2.7)$$

where the constants  $\alpha_{EM}/3$  and the dipole moment  $\mu_{eff}$  are canceled. Therefore, we can obtain the value of  $\epsilon$  by measuring the ratio  $R$ .

In this analysis, we focus on the determination of the ratio  $R$  shown in Eq. 2.7 using the data accumulated by Belle experiment.

# Chapter 3

## Belle experiment

This study is based on the data taken in the Belle experiment at the KEKB accelerator.

We introduce the KEKB accelerator (Sec. 3.1), the Belle spectrometer (Sec. 3.2), and the trigger and data acquisition system of the Belle experiment (Sec. 3.3).

### 3.1 KEKB accelerator

KEKB accelerator is an asymmetric electron-positron collider located at KEK in Tsukuba, Japan. KEKB was operated from 1999 to 2010 [50], [51]. The electrons and positrons are accelerated to 8.0 GeV and 3.5 GeV respectively by the LINear ACcelerator (LINAC). They are injected into the main ring and are collided at the interaction point (IP) in the Belle spectrometer. The collision energy is mainly tuned to 10.58 GeV, the energy of the  $\Upsilon(4S)$  resonance that decays into a  $B$  meson pair.

KEKB is called "B-factory" because it produces large number of  $B$  mesons. The  $B$  meson pairs are generated with Lorentz boost  $\beta\gamma = 0.425$  because of the asymmetric energy. This enables the  $B$  mesons to fly about 0.2 mm before their decays.

KEKB accelerator produces not only  $\Upsilon(4S)$  but also  $e^-e^+ \rightarrow q\bar{q}$  ( $q = u, d, s, c$ ) and  $e^-e^+ \rightarrow l^-l^+$  ( $l = \mu, \tau$ ).

The components of KEKB are shown in Fig. 3.1. KEKB consists of two main rings for electrons and positrons and one LINAC. The 8.0 GeV/ $c$  electron ring is called HER, while the 3.5 GeV/ $c$  positron ring is called LER. Both rings are constructed in the existing TRISTAN tunnel whose circumference is 3km.

#### 3.1.1 The structure of LINAC

The schematic view of the LINear ACcelerator (LINAC) is shown in Fig. 3.2. LINAC has 8 sectors; A, B, C, 1, 2, 3, 4, 5, but only sectors A to sector 3 are shown in Fig. 3.2. The sectors with numbers are the regular sectors. Each regular sector has 8 acceleration units and each acceleration unit includes four 2 m accelerator sections. The accelerator sections in each unit are S-band (2856 MHz) RF cavities and are driven by one klystron [53]. Sector A has a pre-injector to produce intense single bunches. It also includes double sub-harmonic

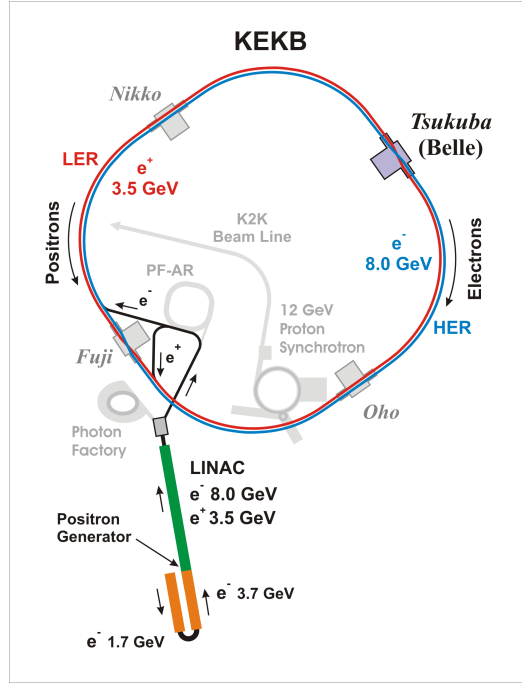


Figure 3.1: Picture of KEKB and LINAC.

bunchers (SHBs) for bunch compression, followed by three accelerator units. The frequencies of SHBs are  $1/25$  and  $1/5$  of the accelerator sections, 114 and 571 MHz. The electron pulse beam from the gun is compressed by each SHB and shaped as bunches. Through acceleration sectors B, C, and 1, electrons are injected to sector 2 which is the positron generator section. To achieve 8.0 GeV energy, 50 MW klystrons are used for the accelerator sections. The number of acceleration units is 57. The average gain of one unit is 160 MeV and the full LINAC energy without beam loading is about 9 GeV. The extra energy above 8 GeV are used to compensate for any gain loss due to defective units, energy-spread adjustment, or energy tuning.

### 3.1.2 Main rings

The accelerated electrons and positrons are injected into HER and LER respectively through the beam transport lines and are stored in the main rings. The interaction point is placed in Tsukuba experimental hall where the electron and positron beams collide at a finite angle of  $\pm 11$  mrad. The Belle spectrometer is installed in the interaction point.

The two main rings of KEKB are located side by side horizontally, because vertical bending of the beams tends to increase the vertical beam emittance. As a consequence, the length of rings are different between outer and inner side. In order to make the circumference of HER and LER precisely equal, a crossing point is made in Fuji experimental hall located at the opposite side of Tsukuba hall. In Tsukuba-Oho-Fuji section, HER is located in the outer side and LER is located in the inner side. In the other section, Fuji-Nikko-Tsukuba,

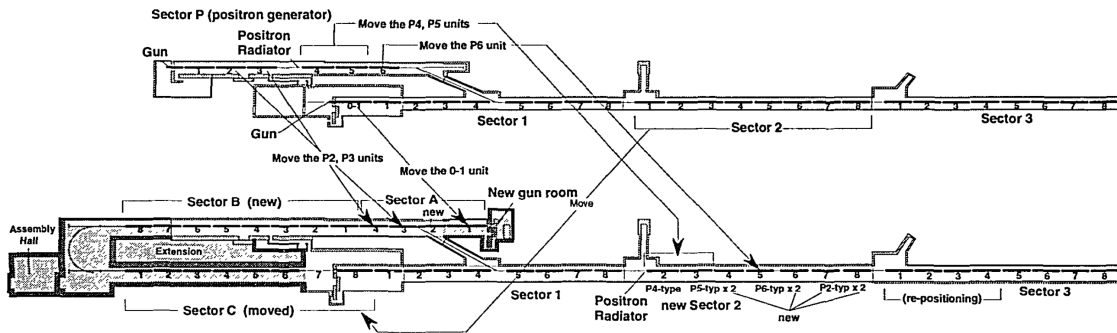


Figure 3.2: The bottom shows the structure of LINAC. The top is the old LINAC at TRISTAN, and the components of which are reused in the present LINAC. Note that LINAC continues on the right side of the picture. [52]

the location of two rings are opposite. The straight sections at Nikko and Oho are used for RF cavities for HER. The wigglers for LER are also placed at those straight sections. They reduce the longitudinal dumping time of LER from 43 ms to 23 ms which is the same as the dumping time of HER. RF cavities for LER are placed in the straight section at Fuji. These RF cavities are equipped to compensate for the energy loss.

### 3.1.3 The interaction point

The interaction point adopt a finite-angle crossing scheme at KEKB. The electron and positron beams collide with an angle of  $\pm 11$  mrad to avoid parasitic collisions. Since the separation bend magnets are not needed, the design of synchrotron light masks and a round vertex vacuum chamber at the interaction point becomes much less complex. Moreover, the absence of the separation bend magnet reduces the synchrotron radiation near the interaction point significantly. The room created by the scheme is used for a cryostat containing one superconducting solenoid and final-focus quadrupole magnets.

### 3.1.4 Magnets to control the beams

In the main rings, magnets are placed to manage the beam orbit. First are dipole magnets to bend the beams in the arc sections between the experimental halls and crossing point in Fuji. There are 114 dipole magnets in HER and 171 in LER. Second are quadrupole magnets to focus and keep the beam in the beam line. There are 452 quadrupole magnets in HER and another 452 in LER. Third are sextuple magnets for the chromaticity correction in the beam line. There are 104 sextuple magnets in HER and another 104 in LER. Forth are steering correction magnets to correct the vertical orbit. They are installed adjacent to each individual quadrupole magnet. There are 450 correction magnets in HER and another 450 in LER. The last is wiggler magnets only used in LER to control the radiation damping time. There are 154 wiggler magnets.

## 3.2 Belle spectrometer

The Belle spectrometer is a multi purpose  $4\pi$  detector to detect the decay of particles, in particular B mesons [54].

The spectrometer need to measure the particle trajectory, the energy, and the particle identification (PID) in whole  $4\pi$  region with a high efficiency.

A schematic view of the Belle spectrometer is shown in Fig. 3.3. Silicon Vertex Detector (SVD) placed just outside of the beam pipe detects particle trajectories precisely to reconstruct B meson decay vertices (Sec. 3.2.1). Central Drift Chamber (CDC) provides tracking information for charged particles, and it also works as a part of PID system (Sec. 3.2.2). The PID devices placed outside of CDC are Aerogel Cherenkov Counters (ACC) (Sec. 3.2.3) and Time-Of-Flight counters (TOF) (3.2.4). CsI crystals are used as Electromagnetic Calorimeter (ECL) for the energy measurement (Sec. 3.2.5). KLM is a detector to reconstruct  $K_L$  and  $\mu$  (Sec. 3.2.6). A super conducting solenoid is placed between ECL and KLM and provides a 1.5 T magnetic field in all inner detectors.

The detector covers from  $17^\circ$  to  $150^\circ$  in the polar angle. Extreme Forward Calorimeter (EFC) is placed in the smaller-angle region to extend the coverage of electron and photon detection for physics processes such as  $B \rightarrow \tau\nu$ . The parameters of each detectors are summarized in table 3.4.

Belle spectrometer accumulated the data in the 11 years of KEKB operation. The peak luminosity reaches  $2.1 \times 10^{34} \text{ cm}^{-2}\text{s}^{-1}$  and the total integrated luminosity is  $1040 \text{ fb}^{-1}$ .

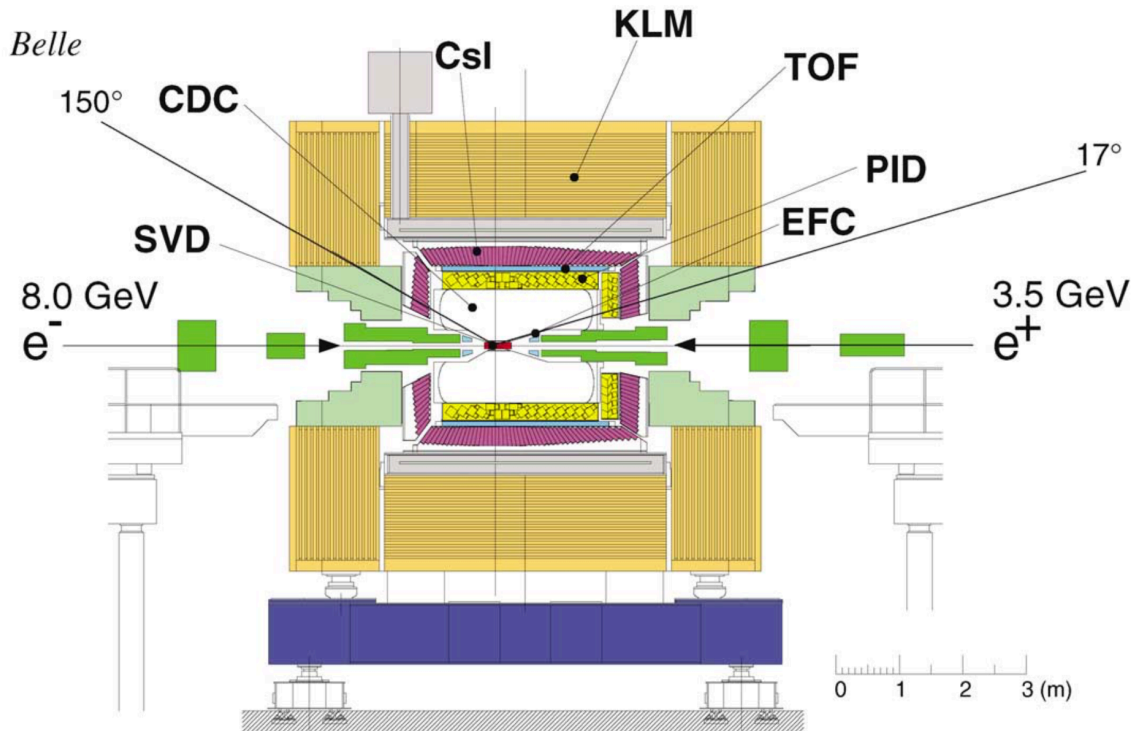


Figure 3.3: The side view of the Belle detector [54].

Figure 3.4: The performance parameters of the detectors [54].

Detector	Type	Configuration	Readout	Performance
Beam pipe	Beryllium double wall	Cylindrical, $r = 20$ mm $0.5/2.5/0.5$ (mm) = Be/He/Be		He gas cooled
EFC	BGO	Photodiode readout segmentation: $32$ in $\phi$ ; $5$ in $\theta$	$160 \times 2$	RMS energy resolution: $7.3\%$ at $8$ GeV $5.8\%$ at $3.5$ GeV
SVD	Double-sided Si strip	Chip size: $57.5 \times 33.5$ mm <sup>2</sup> Strip pitch: $25$ (p)/ $50$ (n) $\mu$ m $3$ layers: $8/10/14$ ladders	$\phi$ : $40.96$ k $z$ : $40.96$ k	$\sigma_{A_z} \sim 80$ $\mu$ m
CDC	Small cell drift chamber	Anode: $50$ layers Cathode: $3$ layers $r = 8.3$ – $86.3$ cm $-77 \leq z \leq 160$ cm	$A$ : $8.4$ k $C$ : $1.8$ k	$\sigma_{r\phi} = 130$ $\mu$ m $\sigma_z = 200$ – $1400$ $\mu$ m $\sigma_{p_t}/p_t = 0.3\% \sqrt{p_t^2 + 1}$ $\sigma_{dE/dx} = 6\%$
ACC	Silica aerogel	$960$ barrel/ $228$ end-cap FM-PMT readout		$N_{p.e.} \geq 6$ $K/\pi$ separation: $1.2 < p < 3.5$ GeV/ $c$
TOF	Scintillator	$128$ $\phi$ segmentation $r = 120$ cm, $3$ -m long	$128 \times 2$	$\sigma_t = 100$ ps $K/\pi$ separation: up to $1.2$ GeV/ $c$
TSC		$64$ $\phi$ segmentation	$64$	
ECL	CsI (towered structure)	Barrel: $r = 125$ – $162$ cm End-cap: $z = -102$ cm and $+196$ cm	$6624$ $1152$ (F) $960$ (B)	$\sigma_E/E = 1.3\%/\sqrt{E}$ $\sigma_{pos} = 0.5$ cm/ $\sqrt{E}$ ( $E$ in GeV)
KLM	Resistive plate counters	$14$ layers ( $5$ cm Fe + $4$ cm gap) $2$ RPCs in each gap	$\theta$ : $16$ k $\phi$ : $16$ k	$\Delta\phi = \Delta\theta = 30$ mr for $K_L$ $\sim 1\%$ hadron fake
Magnet	Supercon.	Inner radius = $170$ cm		$B = 1.5$ T

### 3.2.1 Silicon Vertex Detector

Silicon Vertex Detector (SVD) is placed at the most inner part of Belle spectrometer.

One of the major goals of Belle experiment is to observe time-dependent CP violation in  $B$  mesons. For the SVD, the vertex detector of Belle,  $\sim 100\mu$ m resolution is required to determine the vertices of  $B$  mesons to observe the CP violation. In the asymmetric collision of electrons and positrons, the  $B$  mesons are generated with a Lorentz boost of  $\beta\gamma = 0.425$  along z-axis in Lab frame, so that B mesons decay in flight with a flight length of  $100$  micron. It enables to measure the difference in decay time between  $B$  and  $\bar{B}$ ,  $\Delta t$ , which shows the time-dependent CP violation through the displacement of decay vertices  $\Delta z$ , as  $\Delta t \sim \Delta z/\beta\gamma c$ . In addition, the high precision of track detection is useful for the analysis of  $D$  mesons,  $\tau$  and the other physics because it reduce the combinatorial backgrounds by distinguish the sources of particles.

At the beginning of Belle experiment (1999-2003),  $3$  layer SVD (SVD1, Fig. 3.5) is installed. The operation of SVD1 is successful, but the radiation tolerance of readout electronics limits the efficiency. After  $5$  years operation, the signal-to-noise ratio of the inner

most layer degrades by about 30%. In 2003, SVD1 is upgraded to 4 layer SVD (SVD2, Fig. 3.6) with radiation hard readout chips to regain the efficiency. The integrated luminosities collected with SVD1 and SVD2 are  $141 \text{ fb}^{-1}$  and  $458 \text{ fb}^{-1}$  for  $\Upsilon(4S)$ , respectively .

SVD employs double-sided silicon detector (DSSD). The size of DSSD is about  $8 \times 3 \text{ cm}^2$  for SVD2 while  $6 \times 3 \text{ cm}^2$  for SVD1. The strip pitches of SVD2 (SVD1) are 73-75 (50)  $\mu\text{m}$  on p-side and 50-65  $\mu\text{m}$  on n-side. The strips are stretched so that they are perpendicular to each other, p-side in the  $z$  direction and n-side in the  $\phi$  direction. The DSSDs are mounted on ladders. The ladders are placed around beam pipe cylindrically (Fig. 3.5) to cover  $2\pi$  for  $\phi$  and  $17^\circ \sim 150^\circ$  ( $23^\circ \sim 139^\circ$ ) for  $z$ -axis.

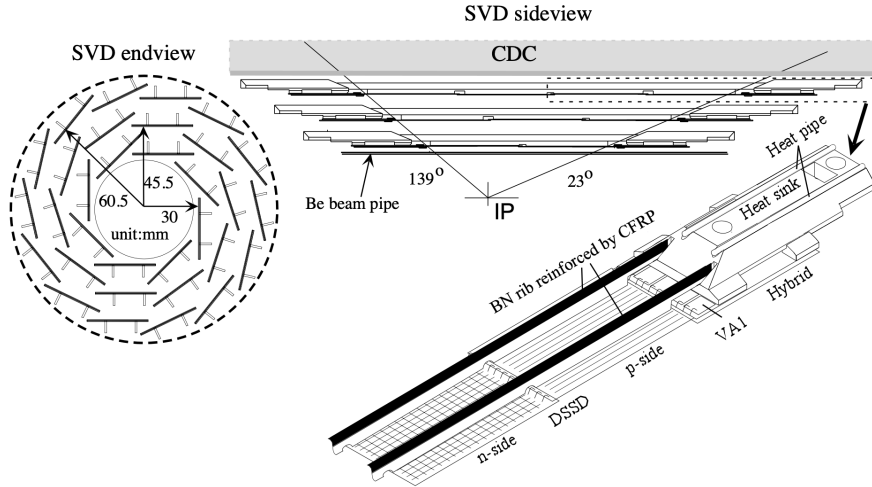


Figure 3.5: The structure of SVD1 [54]. Left: The end view of SVD shows the cylindrical structure of the ladders which covers  $2\pi$  of  $\phi$ . Right top: The side view of SVD shows the coverage of SVD1 in  $z$ -axis, from  $23^\circ$  to  $139^\circ$ . Right bottom: The schematic view of the ladder and DSSD.

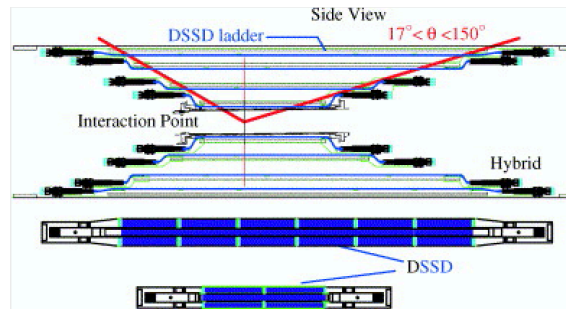


Figure 3.6: The structure of SVD2. The side view of SVD shows the 4 layers and the coverage of SVD2 in  $z$ -axis, from  $17^\circ$  to  $150^\circ$ .

The resolution of SVDs is shown in Fig. 3.7. The resolution is estimated by cosmic ray muons recorded during collision run. SVD1 achieves  $100 \mu\text{m}$  resolution except low-momentum region. That degradation is improved in SVD2 and  $100 \mu\text{m}$  resolution is achieved in all momentum region. Track matching with CDC also shows higher than 95% (Fig. 3.8).

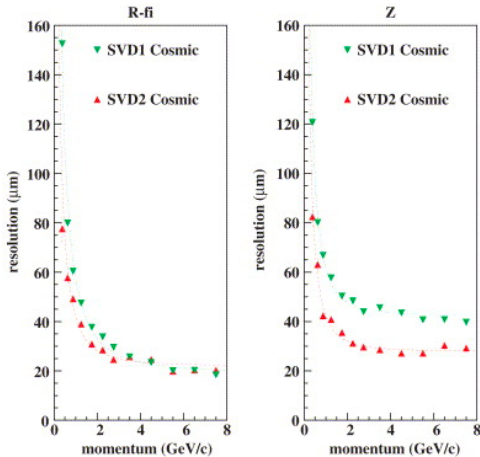


Figure 3.7: The resolution of SVD1 and SVD2 using cosmic ray. Left is for  $\phi$  and right is for  $z$  direction.

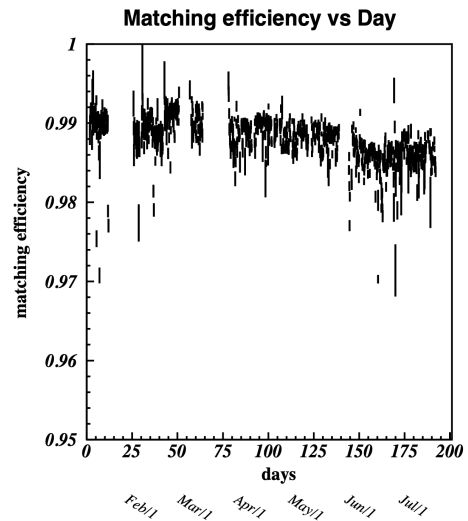


Figure 3.8: The track matching between SVD1 and CDC as a function of the date of data taking.

### 3.2.2 Central Drift Chamber

Central Drift Chamber (CDC) is designed to find charged tracks, measure their momentum, and provide  $dE/dx$  information for PID. CDC has a cylindrical shape with a diameter of 88 cm and a length of 2.2 m containing gas and 50 layers of sense wires with field wires to detect tracks, which covers from  $17^\circ$  to  $150^\circ$  region along  $z$ -axis (Fig. 3.9).

The wires are placed as shown in Fig. 3.10 and 3.11. The field wires are placed around the sense wires in a square. The distance between the layers is from 15.5 to 17 mm and the drift distance is from 8 to 10 mm (Fig. 3.11). Gold-plated tungsten wires with  $30 \mu\text{m}$  diameter and aluminum wires with  $126 \mu\text{m}$  diameter are used for sense wires and field wires, respectively. A high voltage of 2.3 kV is applied to the sense wires while the field wires are connected to the ground. Each of 2 - 6 layers of the sense wires constructs two kinds of super layers which are axial super layers along  $z$ -axis and small-angle stereo super layers with  $40 - 75 \text{ mrad}$  to  $z$ -axis. The axial super layers and stereo super layers are piled up alternately to have  $z$ -measurement capability. In addition, at an early stage during SVD1, there are 7.4 mm wide cathode strips which are placed perpendicularly to  $z$ -axis in the inner cylinder of the chamber and between second and third layers (Fig. 3.10) to provide  $z$ -coordinate measurement in the innermost of CDC.

The gas is a mixture of 50% He and 50% ethane whose  $Z$  is lower than argon-based gases. The low- $Z$  minimizes the Coulomb scattering contribution to the momentum resolution and backgrounds from synchrotron radiation because of its smaller photo-electric cross section. The radiation length of the gas is 640 m and the drift velocity saturates at  $4 \text{ cm}/\mu\text{s}$ . This condition is important for square celled chamber because the electric field has large uniformity.

The sense wires are connected to Charge ( $Q$ ) to Time Converter (QTC) module through Radeka-type preamp, shaper, and discriminator. The QTC output is a digital pulse whose

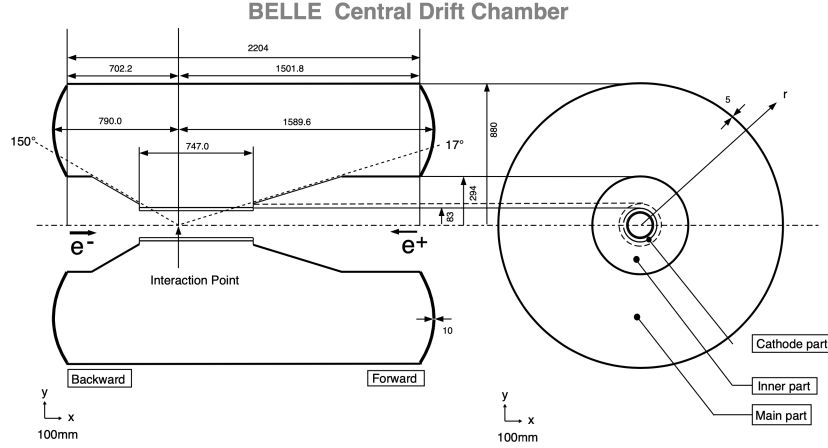


Figure 3.9: The overview of CDC structure [54]. The unit of length in figure is mm.

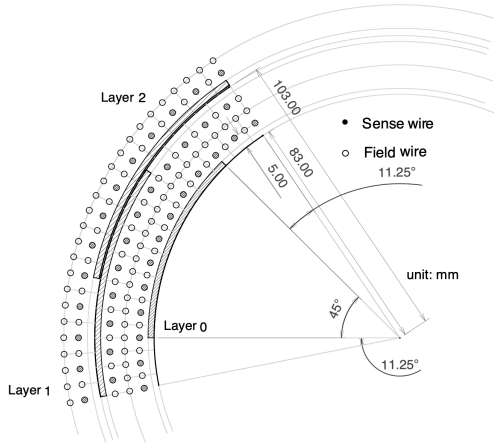


Figure 3.10: The first to third layers of CDC. The closed circles are sense wires and the open circles are field wires. Lined squares are cathode strips.

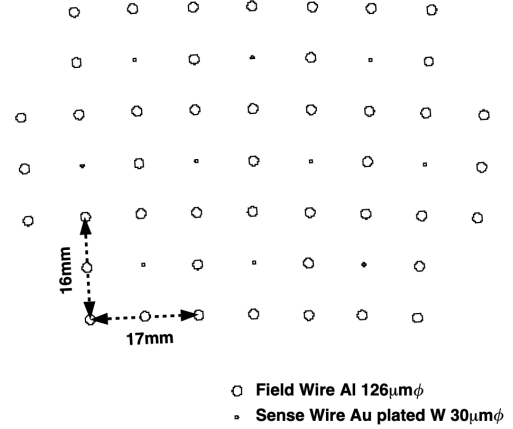


Figure 3.11: The wire configuration of CDC. The dots are sense wires and the open circles are field wires. The field wires make squares surrounding each sense wire.

leading-edge and width correspond to the drift time and pulse height, respectively. The output of QTC is read by multi-hit TDC.

The measurement of momentum is done from the track curvature with the relation

$$p = qBr \quad (3.1)$$

where  $p$  [GeV] is the transverse momentum,  $q$  [ $0.3/e$ ] is the track charge where  $e$  is the elementary charge,  $B$  [T] is the magnetic field, and  $r$  [m] is the radius of the track curvature. The resolution of momentum is evaluated by cosmic muons through the IP. The momentum of a muon before and after passing through the IP are measured independently. The measured momentum are compared as shown in Fig. 3.12. For higher momentum, the resolution becomes worse due to the smaller curvature.

The  $dE/dx$  measurement is based on the charges obtained by the sense wires. The energy deposit of a track on each sense wire shows long-tailed Landau distribution. To avoid the

occasional large fluctuation, the largest 20 % outputs are discarded. The energy loss is calculated by the truncated-mean method from the remaining distribution. The resolution is about 5 % and the scatter plot shows the separation of  $K$ ,  $\pi$ ,  $p$ , and  $e$  clearly (Fig. 3.13).

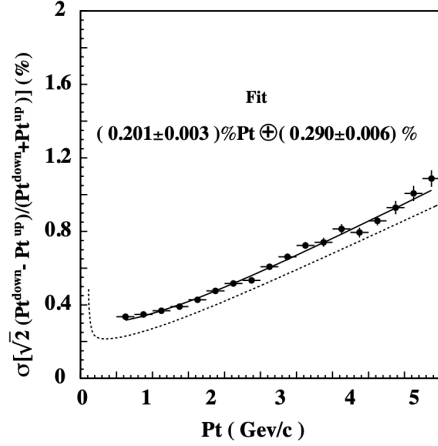


Figure 3.12: The resolution of momentum for cosmic muons on transverse momentum  $P_t$  [54].

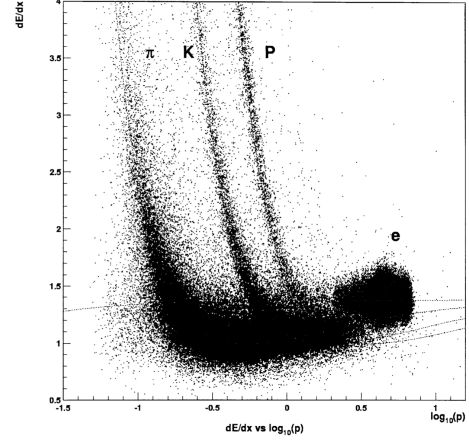


Figure 3.13: The truncated mean of  $dE/dx$  on momentum observed in collision data [54].

### 3.2.3 Aerogel Cherenkov Counter

Aerogel Cherenkov Counter (ACC) is a PID device for the  $K\pi$  separation in higher momentum region. Particles with momentum below 1.2 GeV/ $c$  can be identified by CDC and TOF (shown later). ACC is employed to extend the coverage in higher momentum region.

ACC is a threshold type Cherenkov counter. If the particle velocity satisfies the condition

$$\beta > \frac{1}{n} \quad (3.2)$$

where  $n$  is refractive index, Cherenkov light is emitted. When  $n$  is set at 1.01, ACC can separate  $K/\pi$  in the 1.0 - 3.5 GeV/ $c$  momentum range, since the Cherenkov light is emitted for pions with the momentum above 1.0 GeV/ $c$ , while not for kaons with the momentum below 3.5 GeV/ $c$ .

The structures of ACC is shown in Fig. 3.14. ACC uses the silica-aerogel as the radiator. The silica-aerogel is a porous material made from a gel of  $\text{SiO}_2$  by supercritical drying where its refractive index can be controlled by its density. The aerogel is shaped as tiles and contained in a  $12 \times 12 \times 12 \text{ cm}^3$  aluminum box. The PhotoMultiplier Tubes (PMTs) are also mounted in the box for the detection of Cherenkov radiation. The aluminum boxes are placed outside of CDC to cover the polar angle of  $17 - 127^\circ$ . Refractive indices of aerogels are tuned to maximize the  $K\pi$  separation in each polar angle. For the detection of Cherenkov radiation, ACC employs fine-mesh PMTs with three different diameters for each refractive index aerogel to get uniform response in the magnetic field. The configurations of each PMT and aerogel is shown in the left of Fig. 3.14. The gain of PMTs is about  $10^8$  ( $10^3$ ) at 2500V

in the perpendicular (parallel) magnetic field. The signals from PMTs are received by the pre-amplifier and sent to TDC through QTC. The light yield is measured by the charge output.

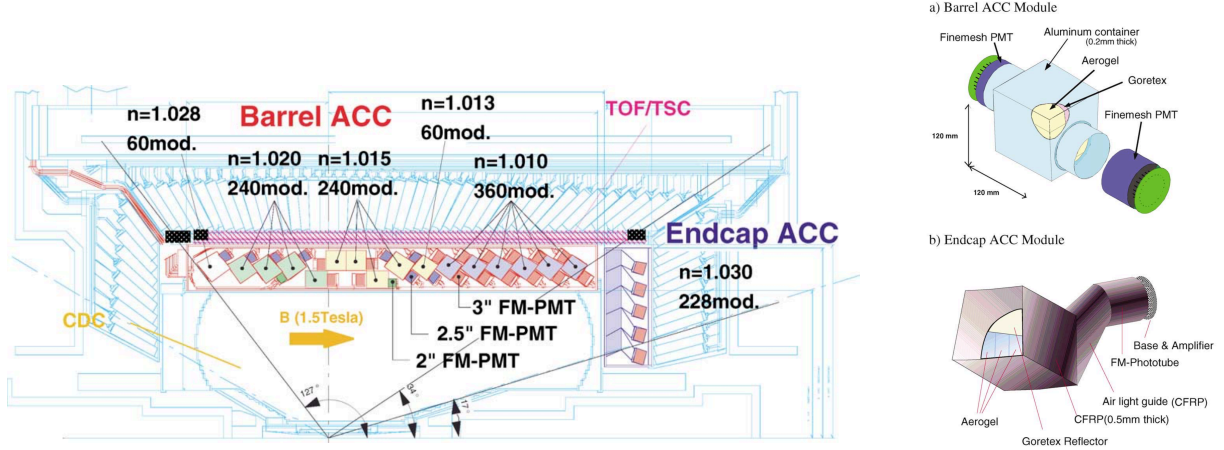


Figure 3.14: The structure of whole ACC and each module in barrel and endcap [54].

Figure 3.15 shows the separation of electrons and pions obtained in  $e^+e^- \rightarrow e^+e^-e^+e^-$  and  $K_s \rightarrow \pi^+\pi^-$  processes. The electron identification efficiency is estimated to be higher than 90% with a 0.2 - 0.3 %  $\pi$  fake rate. Figure 3.16 shows the  $K/\pi$  separation performance obtained by the combined analysis of CDC, TOF and ACC. In the momentum region of 0.5-4.0 GeV/c, the kaon identification efficiency is more than 80% with a pion fake rate less than 10%.

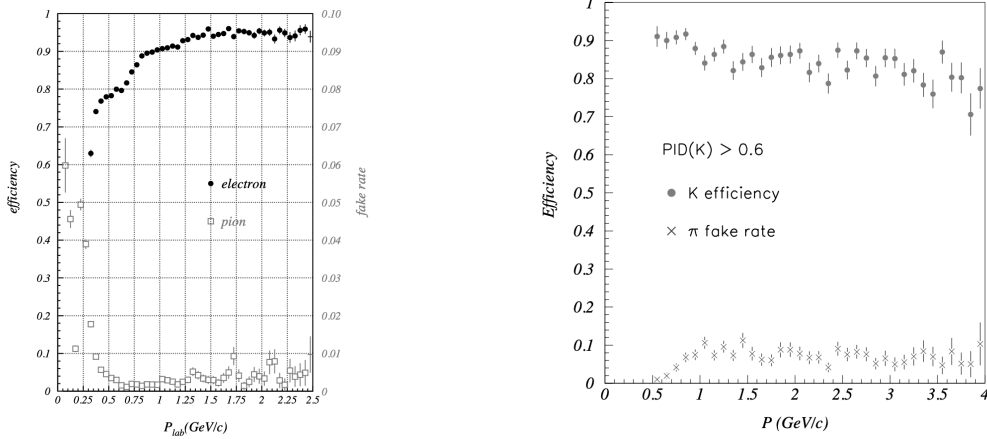


Figure 3.15: The electron efficiency on momentum. Note the different scales for the efficiency and fake rate [54].  
 Figure 3.16: The  $K\pi$  separation by joint PID of CDC, TOF and ACC on momentum [54].

### 3.2.4 Time of Flight Counter

Time Of Flight counter (TOF) system is a PID device using plastic scintillation counters. TOF system is placed outside of CDC and ACC (Sec. 3.2.3). For a 1.2 m flight path, the time of flight measurement with 100 ps time resolution can identify kaons from pions below 1.2 GeV/c. In addition to the particle identification function, TOF also can provide the fast timing signal which is used for the generation of trigger signal. For this purpose, additional thin scintillation counters called Trigger Scintillation Counters (TSC) are mounted between ACC and TOF.

Figure 3.17 shows the structure of TOF and TSC. The TOF system consists of 127 TOFs are 64 TSCs. The size of scintillators is  $4 \times 6 \times 255 \text{ cm}^3$  for TOF and  $0.5 \times 12 \times 263 \text{ cm}^3$  for TSC. The polar angle coverage is in  $34 - 120^\circ$ . There is a 1.5 cm gap between TOFs and TSCs to prevent electrons generated by the photon conversion in TSC from entering into TOF. A 1.5 cm gap in 1.5 T magnetic field is enough to isolate the electrons produced in TSCs and those backgrounds in TSCs are rejected by taking coincidence between TOFs and TSCs.

The scintillators are Bicron, BC408. The light propagation velocity and attenuation length measured by cosmic muons are  $14.4 \text{ cm}/\mu\text{s}$  and 3.9 m, respectively. PMTs are the fine-mesh type PMT made by Hamamatsu, with 2 inch diameter and 24 stage of 2000 mesh/inch dynode. The PMT has a gain of  $3 \times 10^6$  at 2800 V in 1.5 T magnetic field. For TOF, 2 PMTs are placed at each end of scintillator with a 0.1 mm gap. For TSC, one PMT is glued to the light guide. The readout consists of QTC and TDC. The timing of signal leading edge is measured by TDC, and the pulse-height dependence of signal timing (time walk) is corrected by the charge output measured by QTC.

The resolution of TOF system is measured by cosmic muons (Fig. 3.18). The weighted average of output in both end of TOF shows the resolution less than 0.1 ns which is enough to separate kaons from pions below 1.2 GeV/c (Fig. 3.19).

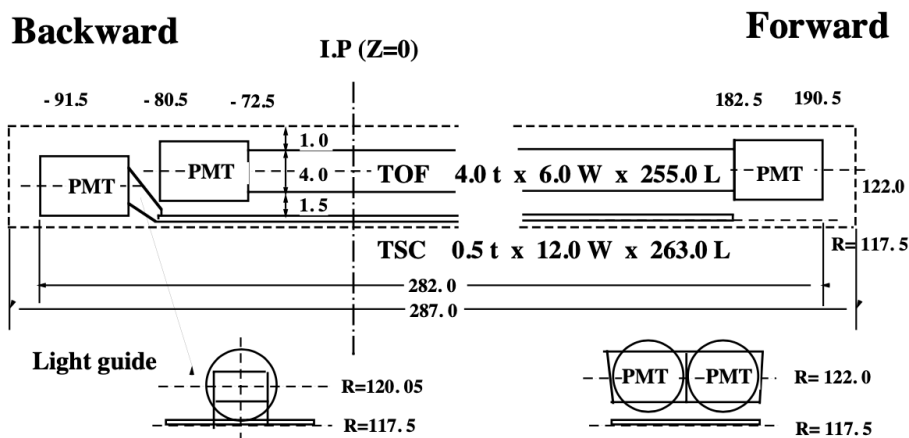


Figure 3.17: The structure of TOF and TSC [54].

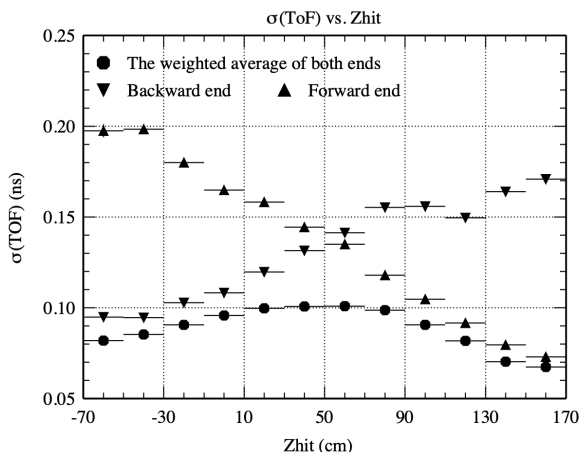


Figure 3.18: The timing resolution of TOF on z-axis [54].

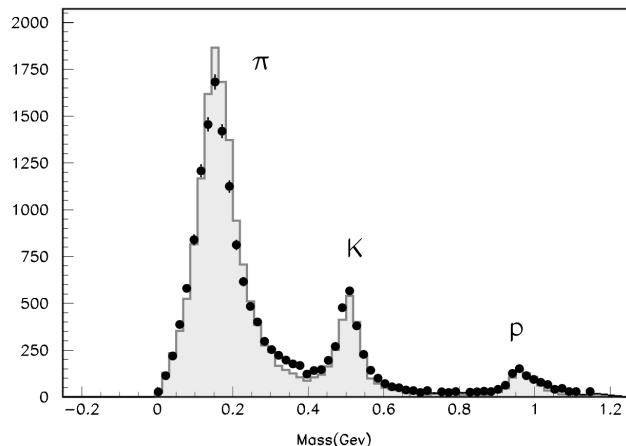


Figure 3.19: The particle separation below 1.2 GeV/c in collision data [54].

### 3.2.5 Electromagnetic Calorimeter

Electromagnetic CaLorimeter (ECL) is placed outside of TOF.

The main function of ECL is to measure the photon energy in a high efficiency with a good position resolution. The position resolution is also needed to distinguish two photons from  $\pi^0 \rightarrow \gamma\gamma$  and detect the  $\pi^0$  up to 4 GeV/c.

The other function of ECL is to identify electrons by measuring energy deposit of electromagnetic shower in ECL. The PID for electrons primarily depends on measurements of momentum by CDC and energy deposit by ECL. For the electron, the momentum ( $p$ ) and energy ( $E$ ) are expected to be equal, namely  $E/p = 1$ , not for the other particles.

To achieve the required efficiency and resolution, ECL is composed of high segmented CsI crystals with silicon photodiodes. The structure of ECL is shown in Fig. 3.20. The number of crystals are 6624 in barrel, 1152 in forward endcap, and 960 in backward endcap, respectively. The crystals are tapered and placed pointing the interaction point with a small tilt angles ( $1 \sim 4^\circ$ ) to avoid photons escaping from the gap of crystals.

Each crystal has a tower like shape (Fig. 3.21) with a size of  $55 \times 55 \text{ mm}^2$  for front face and  $65 \times 65 \text{ mm}^2$  for back face in barrel region. In the endcap region, the size is varied from 44.5 mm to 70.8 mm for the front endcap while from 54 mm to 82 mm for the backend. The height is 30 cm for all crystals. The radiation length of CsI(Tl) is 1.86 cm. Those sizes are determined by the requirement to contain 80% of total energy deposit of a photon injected in the center of the crystal. Each crystal is wrapped with 200  $\mu\text{m}$  Goretex teflon and then covered with 25  $\mu\text{m}$  aluminum and mylar for light and electrical shielding.

For the photodiodes, Hamamatsu S2744-08 is chosen whose size is  $10 \times 20 \text{ mm}^2$ . Two photodiodes are glued to each crystal (Fig. 3.21) and preamplifiers are mounted on the back face. The signals from two photodiodes amplified by the preamp are sent to a shaper and summed. The summed signal is sent to a charge-to-time (Q-to-T) converter, LeCroy MQT300A, and TDC, LeCroy 1877S multi-hit TDC.

The performance evaluated by Bhabha-scattering events in Belle shows that the energy

## BELLE CsI ELECTROMAGNETIC CALORIMETER

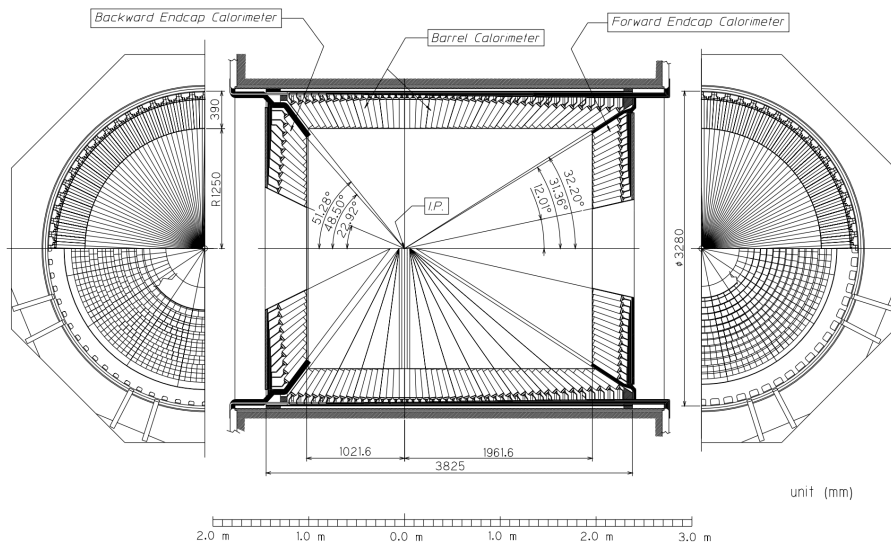


Figure 3.20: The overview of ECL structure [54].

resolution is about 4% at 100 MeV and 1.6% at 8 GeV.

### 3.2.6 $K_L/\mu$ detector

The  $K_L$  and muon detector (KLM) is placed at the most outer side of Belle spectrometer. The function of KLM is to identify  $K_L$  and  $\mu$  in the momentum range above 0.6 GeV/c. The barrel part covers the polar angle of 45 - 125° region and the endcap part extends the coverage to 20 - 155°.

The detector consists of 15 and 14 super layers of glass-resistive plate counters (RPC) sandwiched with iron absorbers for the barrel and endcap part, respectively. Interacting with the iron layers,  $K_L$  produces hadron shower. The shower is tracked by the detector layers and the direction of the  $K_L$  track is reconstructed from the shower shape. Muons less interact with iron absorbers and are identified when all detector layers have hits.

An RPC module consists of parallel electrode plates with a high resistivity ( $> 10^{10}\Omega\text{cm}$ ) and a gas mixture (65% of HFC-134a, 30% of argon, and 8% of butane-silver) filled in the gap of the plates. A couple of RPC layers compose a super layer of KLM in which the layers are placed to cover the inefficient region of each other (Fig. 3.22). A HV is applied to both electrodes,  $-3.5$  kV to cathode and  $+4.7(+4.7)$  kV to barrel (endcap) part. When a charged particle transverses the plates, it makes a discharge which is localized by the high resistivity of the plates and the quenching characteristics of the gas. The discharge makes a current on the readout strips placed on the both plates which is approximately 5 mA or  $1 \mu\text{A}/\text{m}^2$  of the RPC area. KLM has 3800 readout strips in total and they records the location and time of discharges. The readout strips are connected to VME based discriminators. The signal is time-multiplexed to obtain the location and timing by the multi-hit TDC.

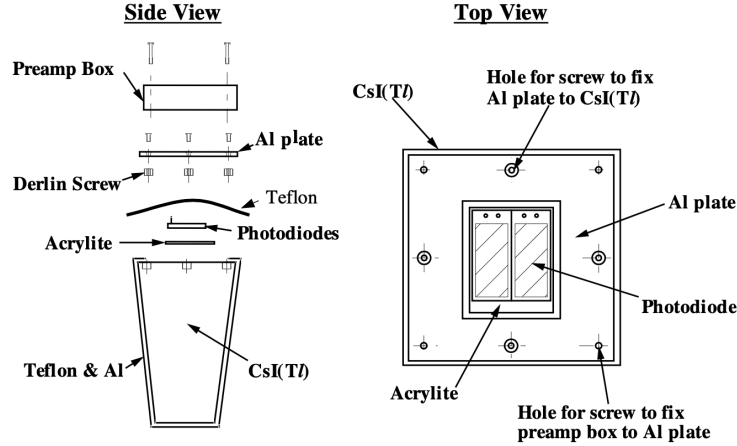


Figure 3.21: The assembly of crystal and photodiodes [54].

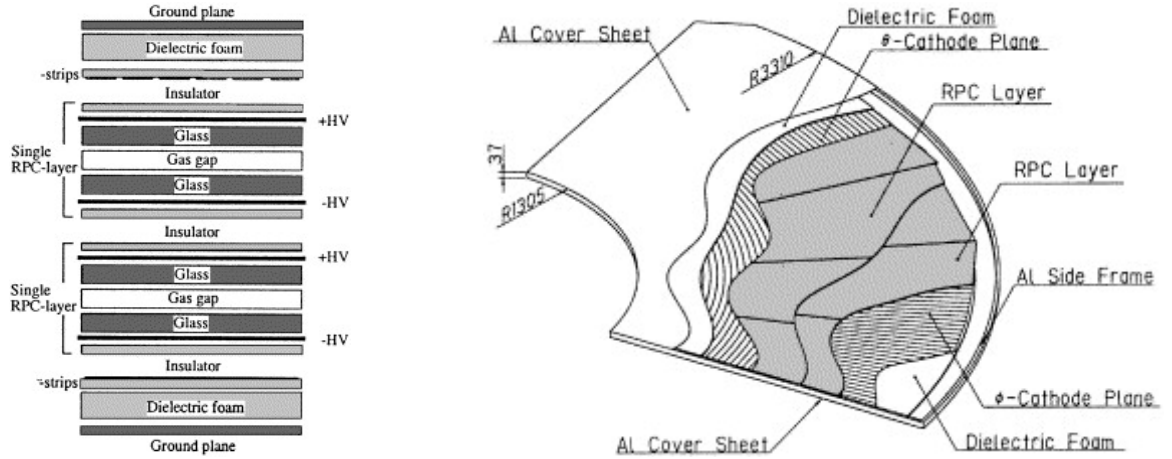


Figure 3.22: The structure of layers of KLM [55].

In the cosmic ray test, a single layer of RPC shows more than 90% efficiency, and, a super layer shows more than 98% in average. The identification efficiency for muons in  $e^+e^- \rightarrow \mu^+\mu^-$  is estimated to be more than 90% and the fake rate of pions in  $K_S^0 \rightarrow \pi^+\pi^-$  is less than 2% for the momentum range above 1 GeV/c.

### 3.3 Trigger and Data Acquisition

The data acquisition system (DAQ) collects signals from all sub-detectors and processes them into an event data. The overview of DAQ is shown in Fig. 3.23. As described in previous sections, most of sub-detectors use Charge ( $Q$ ) to Time Converter (QTC) and Time to Digital Converter (TDC) for the readout. Data from each TDC are collected and combined by the event builder. The combined event data are selected in the event building farm (EFARM) and processed by the reconstruction farm (RFARM). Selected events are recorded in the tape

library.

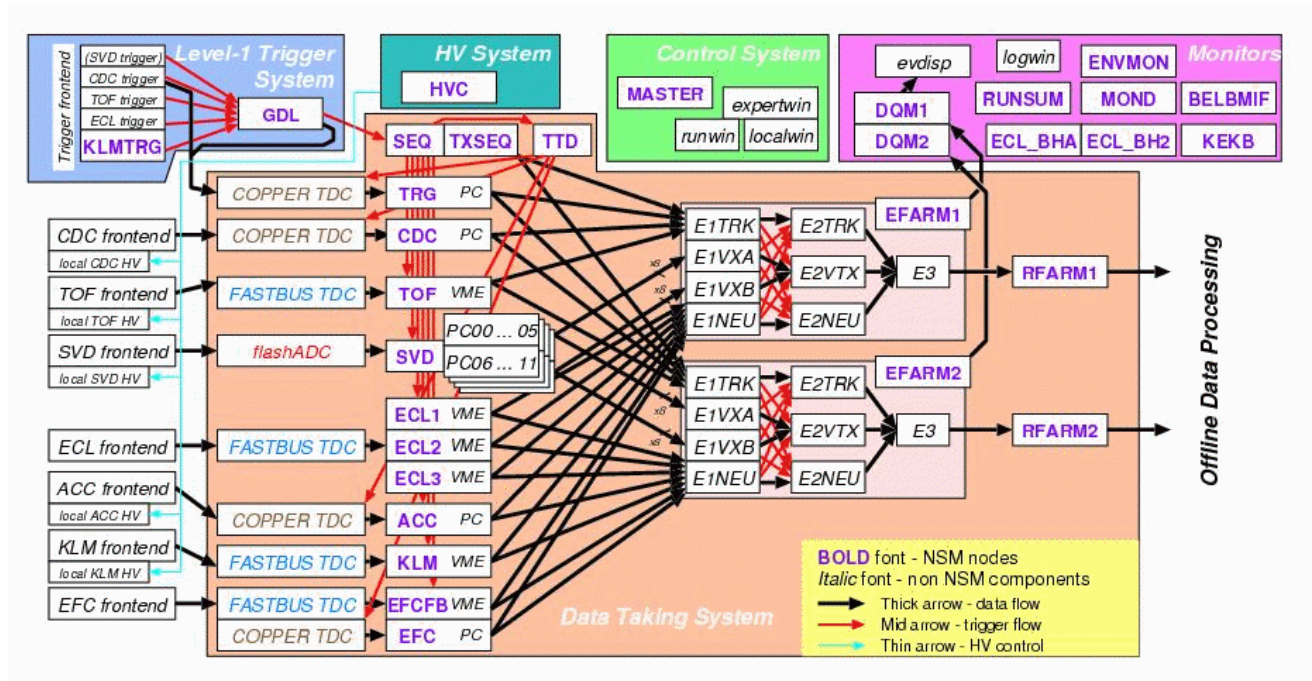


Figure 3.23: The overview of DAQ system [56].

The requirement for the data acquisition system (DAQ) is to record the event data up to 500Hz with a dead time less than 10%. To achieve the requirements, the trigger consists of 3 steps called Level 1 (L1), Level 3 (L3), and Level 4 (L4) triggers.

The L1 trigger which is applied before event building is a combination of hardware triggers in CDC, TOF, ECL, KLM and EFC. Each sub-detector generates sub-trigger signal and they are combined and judged by the global decision logic. Events must satisfy at least one of L1 trigger conditions; (1) there exist three or more tracks in CDC, (2) a total energy sum in ECL is more than threshold (to veto Bhabha and cosmic events), (3) four or more energy clusters exist in ECL. In addition, the other trigger conditions are prepared for different event types such as Bhabha scattering and  $e^+e^- \rightarrow \tau^+\tau^-$  etc. The total rate of L1 trigger is typically 200 Hz in early period and reaches 400 Hz when the luminosity becomes high.

The event data are built and processed by the event building farm where the L3 trigger is performed. The L3 trigger is a software trigger based on the fast track fitting in the event building farm. It requires at least one track comes from the interaction point with  $|dr| < 5$  cm. The L3 trigger reduces the background by half, keeping more than 99 % of hadronic events.

The events passed L3 trigger are processed by the reconstruction farm where the full event reconstruction is performed, and sent to the storage system. For the further reduction of background events, the software trigger, Level 4, is applied in the offline processing. The L4 trigger is based on the precise track fitting results given by the reconstruction farm. L4 requires at least one track with the transverse momentum  $p_t > 300$  MeV/c comes from the

interaction point as  $|dr| < 1.0$  cm and  $|dz| < 4.0$  cm. The L4 trigger reduces backgrounds to 20 %, keeping 98% of hadronic events.

After triggers, the stored events are skimmed for each analysis mode. A skim for hadronic events is following conditions and we use this skim for our analysis; (1) three or more charged tracks with  $p_t > 0.1$  GeV/ $c$ ,  $|dr| < 2.0$  cm, and  $|dz| < 4.0$  cm, (2) the total visible energy,  $E_{vis}$ , which is defined by sum of charged tracks' momenta and sum of clusters' energies is  $E_{vis} > 0.2\sqrt{s}$ , (3) at least two energy clusters on ECL region  $-0.7 < \cos\theta < 0.9$ , (4) the energy sum  $0.18 < E_{sum}/\sqrt{s} < 0.8$ ,(5) the average of clusters on ECL less than 1 GeV.

# Chapter 4

## Event Processing and Monte Carlo Simulation

The target decay of this analysis is  $D^{*0} \rightarrow D^0 A'$  (Sec. 2.5) which is produced in the hadronization of  $c\bar{c}$  pair. The data taken on  $\Upsilon(4S)$  resonance includes  $1.9 \times 10^9$   $c\bar{c}$  events with  $B\bar{B}$  and the other continuum processes ( $e^+e^- \rightarrow u\bar{u}, d\bar{d}, s\bar{s}$ ).

In this chapter, we describe the data set accumulated in 11 years operation of Belle experiment (Sec. 4.1), the software framework for the processing (Sec. 4.2), the data processing procedure (Sec. 4.3), the pre-selection of hadronic events (Sec. 4.4), and the Monte Carlo simulation (Sec. 4.5).

### 4.1 Data sets

There are several types of data sets taken on the resonances of  $\Upsilon(4S)$  and  $\Upsilon(5S)$ , the other  $\Upsilon(nS)$  resonances, and off resonance.

In this analysis, we use the full data set recoded by Belle experiment in 1999 - 2010 at  $\Upsilon(4S)$  resonance which is equivalent to  $711 \text{ fb}^{-1}$ . The  $e^+e^-$  collision in Belle experiment produce five kinds of quark pairs ( $u\bar{u}, d\bar{d}, s\bar{s}, c\bar{c}$  and  $b\bar{b}$ ) classified in following categories:

1. **Uds continuum events** : the lighter quarks events than  $c$  which come from the reaction  $e^+e^- \rightarrow u\bar{u}, d\bar{d}$ , and  $s\bar{s}$ .
2. **B meson decays** : the events with  $e^+e^- \rightarrow \Upsilon(4S)$  and  $\Upsilon(4S) \rightarrow B\bar{B}$ .
3.  **$c\bar{c}$  events** : all the  $c\bar{c}$  events, including the signal of  $D^{*0} \rightarrow D^0 A'$ .

### 4.2 Event processing framework

We use the analysis framework named *basf2* which is developed for Belle II experiment [57].

There is a framework named *basf* developed to analyze the data of Belle experiment. *basf2* is the revised version for the Belle II experiment. *Basf* and *basf2* are the framework to

process event data by reading a data file. The processing is performed by executing a chain of functional modules sequentially, where each module is coded in C++ with an interface to external libraries like ROOT, Geant4, Geant3, and EvtGen. Python is used as the steering script of basf2.

In the analysis, raw data unpacker and digitizer modules for each detector are first called to convert the raw data into detector hits. The event reconstruction is performed with the hit information, and finally four momentum and species of detected particles in the events are obtained. They are written to disk files at the end of processing event by event. In the later term of the experiment, the reconstruction processing is performed in real time by the reconstruction farm.

The reconstruction output are written in the Belle format, which cannot be handled by the native basf2 framework. A framework to convert Belle data into Belle2 format named B2BII is developed, which is a combination of modules on basf2 to read Belle data and set up appropriate processing environment. The analysis here is performed using the B2BII framework.

## 4.3 Event reconstruction

The signal from Belle spectrometer have to be converted to four momentum and particle species of detected particles to be used in the physics analysis. The conversion algorithm is called as the event reconstruction. It consists of three steps, 1) Charged particle tracking, 2) Neutral particle reconstruction, and 3) Particle identification (PID). In this section, we show the detailed procedure in each step.

### 4.3.1 Charged particle tracking

The trajectory of charged particle is reconstructed using the signal from SVD and CDC. The Belle detector is placed in a uniform magnetic field of 1.5 Tesla formed by the solenoid coil for the measurement of particle momentum. The particle trajectory in the magnetic field can be modeled by a helix. The non-uniformity of the magnetic field can distort the helix, but that effect is negligible except in the very forward and backward regions (Fig. 4.1).

The reconstruction of particle trajectories is done in following steps [58] :

1. Hit signals are reconstructed in each detectors; CDC and SVD.
2. Track finding is done in CDC using the helix trajectory model (TRASAN).
3. The matching of CDC track and SVD hit by Kalman filter method to determine the trajectory near IP (TRAK).
4. Rejection of noise-like tracks and extrapolation of tracks to outer detectors.

CDC hits are examined and clusterized to form a track by a software called TRASAN which uses the Hough transform algorithm [59]. The hits are then fitted with SVD hits

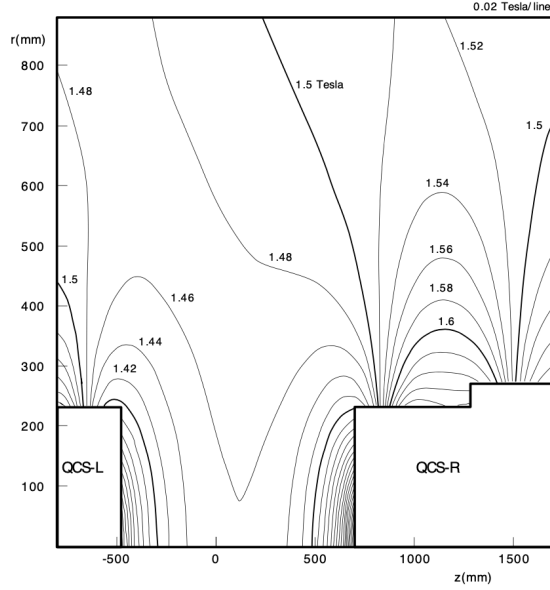


Figure 4.1: The magnetic field distribution near the interaction point.  $+z$  is taken to be anti-parallel to momentum vector of positron beam and  $r$  is perpendicular to  $z$  in the radial direction.[58]

together by Kalman filter algorithm [60] (called TRAK) and the particle trajectory is reconstructed in the helix parameters.

### Track finding in CDC

The trajectory in the  $r$ - $\phi$  plane is obtained using the sense wire signals in axial layers along  $z$ -axis (Sec. 3.2.2). The signal of sense wires in stereo layers, which are displaced from the  $z$ -axis direction, are then combined to form a track in the  $z$ - $\phi$  plane. This result in a three-dimensional hit map, fitted by a helix trajectory model using Hough algorithm [61].

### CDC track - SVD hit matching

The reconstructed tracks are then matched with SVD hits in three steps. The first step is to search for SVD hits associated with the track extrapolated from CDC. Next, all possible 3D track vectors are created by combining the hits, and the vectors which do not come from the IP ( $|dr| > 1\text{cm}$  or  $|dz| > 2\text{cm}$ ) are excluded. Finally, all the remaining track vectors are combined to the CDC track and fitted by helix model using the Kalman filtering [62]. The vector with the highest quality ( $\chi^2$ -probability) is chosen.

### 4.3.2 Neutral particle reconstruction

The neutral particles do not make signals in tracking detectors. To reconstruct those particles, ECL clusters are used. A cluster is the energy deposition in a certain region of the calorimeter

by the electromagnetic and hadron shower processes. The procedure to reconstruct the position and energy of the deposition is called "ECL clustering" [63].

The clustering consists of two steps; the seed search and the energy clustering. The seed search begins with the crystal with the highest energy, and the neighboring crystals are excluded from the seed search. Figure 4.2 shows an image of hits in the array of crystals. First, the crystal with 280 MeV is defined as a seed. The neighboring eight crystals (70, 150, 40, 90, 35, 175, 55, and 125 MeV) are excluded from the seed search, and then the crystal with the second highest energy (circled 150 MeV one, not the 175 MeV one) is defined as the second seed. Note that all seeds must have energies above a threshold and the energy of the crystal between the two seeds (125 MeV one) must be lower than the energies of the seeds.

After the seed is defined, the energy of cluster is calculated by adding energies of  $3 \times 3$  (called  $E_{3 \times 3}$  or  $E9$ ) and  $5 \times 5$  (called  $E_{5 \times 5}$  or  $E25$ ) crystals. If there are crystals shared by two seeds, the energies excluding those crystals ( $E_{3 \times 3}^{excl}$  and  $E_{5 \times 5}^{excl}$ ) are also calculated. Then, the ratios of  $Pure_1 = E_{3 \times 3}^{excl}/E_{3 \times 3}$  and  $Pure_2 = E_{5 \times 5}^{excl}/E_{5 \times 5}$  are calculated to determine the extent to which the energy sum is taken. The cluster with  $Pure_2 > 0.95$  is identified as a lone cluster. The cluster with  $Pure_1 > 0.99$  and not identified as a lone cluster is regarded as an isolated cluster. If the two seeds are separated each other by one crystal and they are not included in a lone cluster nor in an isolated cluster, they are identified as merged clusters. The others are identified as separated clusters. The cluster energy is calculated with  $5 \times 5$  crystals for lone clusters,  $3 \times 3$  for isolated and each of merged clusters.

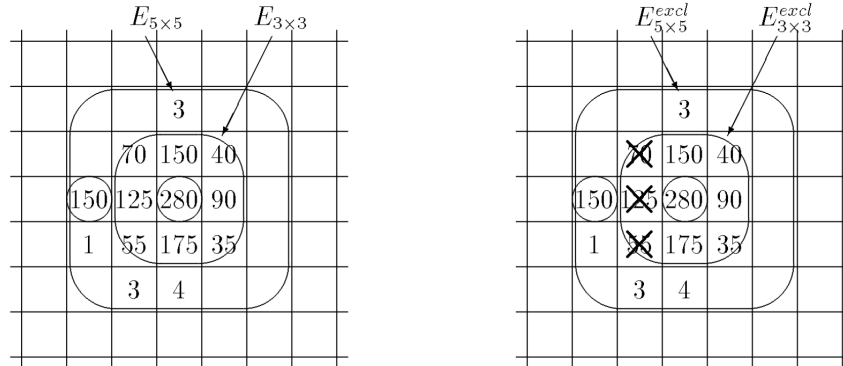


Figure 4.2: The image of seed search and clustering. The squares show the crystals and the numbers are energy depositions on each crystal in MeV [63].

For each cluster, the energy sum ( $E_{sum}$ ) and the position of cluster ( $\theta$  and  $\phi$ ) are calculated.

### 4.3.3 Particle Identifications

The particle species of a reconstructed track is then identified. The procedure is called as the Particle Identification (PID). The tracks are charged and long-lived particles;  $e$ ,  $\mu$ ,  $p$ , charged kaons, and charged pions. The role of PID is to categorize the tracks into one of

the species. The PID is based on likelihoods calculated from the signals in the detectors and probability density functions prepared for each particle beforehand.

In this analysis, the charged final state particles of concern are kaon, pion, and electron. The derivation of the likelihood from the detector hits are discussed as below.

### $K/\pi$ Identification

The kaons and pions are identified using the hit signal in ACC, the  $dE/dx$  measurement by CDC, and the time of flight by TOF. The likelihoods are calculated in each detector and then combined as

$$L_i = L_i^{ACC} \times L_i^{CDC} \times L_i^{TOF} \quad (4.1)$$

where  $i$  is the particle species ( $e$ ,  $\mu$ ,  $p$ ,  $K$ , and  $\pi$ ).

The calculation schemes are different in each detector depending on the type of detector signal. The likelihood calculations are as follows.

#### The likelihood in ACC

ACC is a threshold type Cherenkov counter where the refractive indices are optimized for  $K/\pi$  separation, so that only  $\pi$  emits Cherenkov light. The likelihood is determined by the number of detected photo-electron ( $N_{pe}$ ). The PDF is determined using the MC simulation (Fig. 4.3).

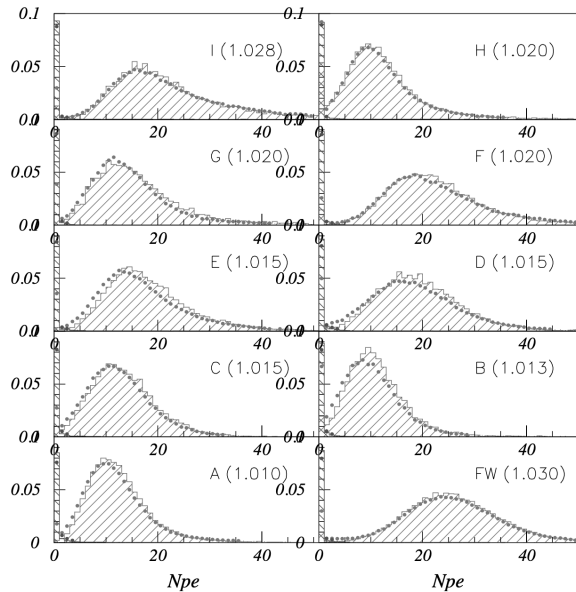


Figure 4.3: The number of photo-electron ( $N_{pe}$ ) for each refractive indices [64].

## The likelihood in CDC

The likelihood of CDC is defined by the energy loss  $dE/dX$  assuming Gaussian distribution for the PDF as

$$L_i = e^{-\chi_i^2/2} \prod_{l=1}^{ndf} 2\pi\sigma_{dE/dx} \quad (4.2)$$

where  $\sigma_{dE/dx}$  is the  $dE/dx$  resolution of CDC and  $\chi_i^2$  is defined as

$$\chi_i^2 = (dE/dx)_{meas.} - (dE/dx)_i \sigma_{dE/dx}^2 \quad (4.3)$$

where  $(dE/dx)_{meas.}$  is the measured  $dE/dx$ ,  $(dE/dx)_i$  is the expected  $dE/dx$ , and  $i$  is the particle species [64].

## The likelihood in TOF

The likelihood of TOF is defined by the time of flight  $t$  assuming Gaussian distribution for the PDF as

$$L_i = e^{-\chi_i^2/2} \prod_{l=1}^{ndf} 2\pi\sigma_{TOF}. \quad (4.4)$$

Since TOF uses PMTs on the two ends of the detector,  $\chi_i$  is defined as the time difference  $\Delta_i^k = t_{meas.}^k - t_i^k$  where  $k = 0, 1$  indicates PMT on two ends of the counter.  $\chi_i$  is written as

$$\chi_i^2 = \Delta_i^T E^{-1} \Delta_i \quad (4.5)$$

where  $\Delta$  is a vector whose elements are  $\Delta^k$  and  $E$  is a  $2 \times 2$  error matrix [64].

## Likelihood ratio method

For every charged tracks, the likelihoods assuming the particle is a kaon or a pion is calculated as  $L_K$  and  $L_\pi$ . Then  $K$  and  $\pi$  mesons are identified by a likelihood ratio of  $K$  and  $\pi$  mesons. The  $K$  likelihood ratio is defined as

$$R(L_K) = \frac{L_K}{L_K + L_\pi} \quad (4.6)$$

where  $L_K$  and  $L_\pi$  is  $K$  likelihood and  $\pi$  likelihood. The likelihood ratio for pions  $R(L_\pi)$  is defined similarly

$$R(L_\pi) = \frac{L_\pi}{L_K + L_\pi}. \quad (4.7)$$

Note that  $R(L_i)$  is 0.5 when the track can not be distinguished and the likelihood ratios are always  $R(L_K) + R(L_\pi) = 1$ .

## **Electron Identification**

In case of electrons, the identification of electrons and positrons are performed based on the  $dE/dx$  measurement by CDC,  $E/p$  matching and shower shape in ECL, and hit signal in ACC. All parameters are modeled by the PDFs and the likelihood method is used for the identification, as in the case of kaons and pions.  $dE/dx$  is treated in exactly the same as that in  $K/\pi$  identification. And the others are as follows [65].

### **The likelihood in ECL**

The likelihood in ECL is defined by two observables;  $E/p$  ratio and  $E9/E25$ .

$E/p$  is the ratio of energy of the particle to its momentum. In the case of the electron, the ratio of mass to energy approaches 1 because the electron deposits almost all its energy in ECL while the mass is negligible compared to the energy. In the case of hadrons, the energy deposition in ECL is partial since the interaction length of hadrons is much longer than the radiation length of electrons and the energy loss by the hadronic interaction is not linearly converted into the light yield. Figure 4.4 shows the distributions of  $E/p$  for electrons and pions. Since the distribution is different, the PDF is prepared for each particle. The electron distribution is modeled as

$$f(x) = (1 - E) \times A \times \exp[-12(x - B\sigma)^2] + E \times A \times \exp[-12(x - BF)^2] \quad (4.8)$$

where  $\sigma$  is  $C + D(x - B)$  if  $x < B$ , and is  $C$  if  $x > B$ . The parameters with capital letters A to F are obtained using MC and  $e^+e^- \rightarrow e^+e^-e^+e^-$  events. The pion distribution of  $E/p$  are modeled by triple Gaussian + linear functions.

The other observable  $E9/E25$  is defined as the ratio of deposited energy in the  $3 \times 3$  crystals to the  $5 \times 5$  crystals of a reconstructed energy cluster (Sec. 4.3.2). Electromagnetic and hadronic showers have different shapes in both of the transverse and the longitudinal directions. The quantity  $E9/E25$  indicates the shower shape in the transverse direction. A higher value of  $E9/E25$  means that the shower is narrow and electromagnetic shower like. A lower value of  $E9/E25$  means thick and hadron-like shower. Figure 4.5 shows the distributions of  $E9/E25$  for electrons and pions. The distribution for electrons shows a peak  $\sim 0.95$  with a smaller low-side tail than that of pions. Those distributions are also modeled in the function,

$$g(x) = A \times \exp[-12(x - BC + D(x - B))^2]. \quad (4.9)$$

For pions, the distribution is in

$$h(x) = g(x) + \text{Gaussian} \quad (4.10)$$

where the parameters with capital letters A to D are fixed beforehand using by MC and  $e^+e^- \rightarrow e^+e^-e^+e^-$  events.

### **The likelihood in ACC**

The likelihood in ACC is defined using the light yield in ACC. In ACC, the threshold of Cherenkov light of electrons is a few MeV, while that of pion is  $0.5 \text{ GeV}/c \sim 1.0 \text{ GeV}/c$

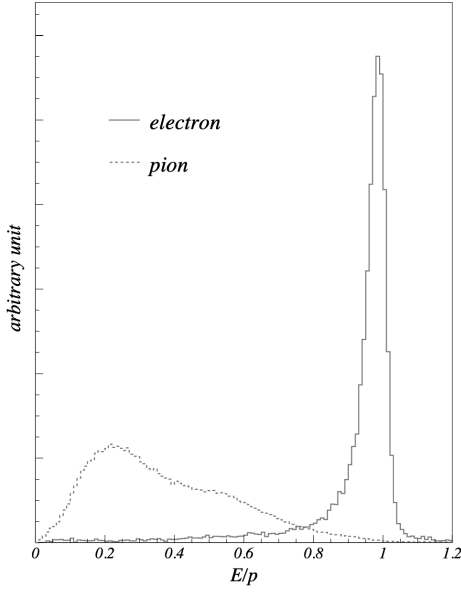


Figure 4.4: The distributions of  $E/p$  for electrons and pions. The solid line shows electrons and the broken line shows pions[65].

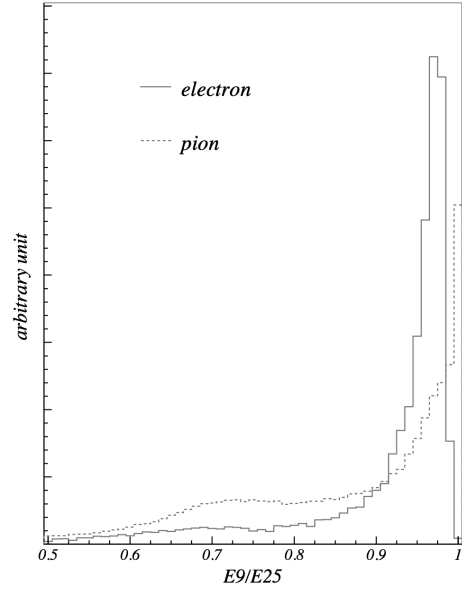


Figure 4.5: The distributions of  $E9/E25$  for electrons and pions. The solid line shows electrons and the broken line shows pions[65].

which depends the refractive indices. The light yield in ACC can be used to distinguish electrons from the other particles. The likelihood is calculated from the MC simulation for 20 different velocity ranges [65].

### The likelihood ratio method

The selection scheme is the same for the electrons and positrons [65]. Likelihood ratio  $R(L_e)$  is calculated using electron likelihood  $L_e$  and non-electron likelihood  $L_{\bar{e}}$  as

$$R(L_e) = \frac{L_e}{L_e + L_{\bar{e}}}. \quad (4.11)$$

The electrons and positrons are identified when the likelihood of the track has more than 0.1. The condition is looser than that used for kaons and pions because of the difference in the detection technique.

### $\gamma$ identification and calculation of four momentum

The identification of  $\gamma$  is done by examining the energy cluster detected in ECL. Two parameters are used to identify a  $\gamma$  in the clusters. One is the energy sum of the cluster ( $E_{sum}$ ) and the other is  $E9/E25$ .

$E9/E25$  is the same observable used in the electron identification. Higher  $E9/E25$  means that the particle is  $\gamma$ -like because it is considered to be electromagnetic showers. The showers induced by the other neutral particles like  $\pi^0$  show lower  $E9/E25$ .

The four-momentum of  $\gamma$  is also calculated from  $E_{sum}$  assuming the  $\gamma$  comes from IP.

## $\pi^0$ reconstruction

$\pi^0$  is reconstructed from two  $\gamma$ s with the selection above. The invariant mass is calculated for all combinations of  $\gamma$  are tried and  $\pi^0$  candidates selected when the mass is within the mass window. The four momentum is calculated from the mass constraint vertex fitting by kfitter using the energies of  $\gamma$ . Then, the candidates are stored as the Belle standard  $\pi^0$  list.

## 4.4 Hadronic event selection

The hadronic events used for this analysis are selected with following criteria [66].

- The number of charged tracks  $nTrk$  is  $nTrk \geq 3$ . The visible energy of tracks and photons  $E_{vis}$  is  $E_{vis} \geq 0.2\sqrt{s}$ .
- The energy sum of ECL in  $17^\circ < \theta < 150^\circ$  region  $E_{sum}$  is  $0.18 < E_{sum}/\sqrt{s} < 0.8$ .
- The number of cluster in  $-0.7 < \cos\theta < 0.9$  region of ECL  $nECL$  is  $nECL > 1$ .
- The average cluster energy of ECL  $E_{sum}/nECL$  is  $E_{sum}/nECL < 1$  GeV.
- The conditional heavy jet mass (described in [67])  $HJM$  is  $HJM/E_{vis} > 0.25$  or  $HJM > 1.8$  GeV.
- The sum of momentum of tracks and photons in  $z$  direction  $P_z$  is  $|P_z| < 0.5\sqrt{s}$ .
- The position of prime vertex  $(r, z)$  calculated from the tracks and kfitter is  $r < 1.5$  cm and  $|z| < 3.5$  cm.

## 4.5 MC simulation

For the data analysis, the event data obtained with the simulation are needed to be compared with the real data. The simulated events are generated using Monte Carlo (MC) method with the event generator which simulates the physics process and then passed through the detector simulation. The data are then fed into the same event reconstruction chain as described above. The MC simulations are designed to provide one-to-one correspondence to the actual experiments, and reflect all the conditions in the operation of experiment like beam status and detector settings of the actual data sets. The total amount of simulated data sets is equivalent to  $4266 \text{ fb}^{-1}$ .

### 4.5.1 Event generation

To simulate particle decays in the electron-positron annihilation ( $Uds$ ,  $c\bar{c}$ , and  $B\bar{B}$ ), we use following generation and simulation packages. The events with  $B\bar{B}$  pair are generated by EvtGen [68] and  $B$  meson decay is produced based on the given decay table. For the  $q\bar{q}$  events, the initial quark pair generated in EvtGen is hadronized by PYTHIA.

## EvtGen

EvtGen is an event generator for simulations of high energy physics experiments specialized to simulate  $B$  meson decay [68]. EvtGen simulates the decay of particles following the given decay table considering the particle properties and kinematics. The feature of EvtGen is using decay amplitudes, instead of probabilities, to simulate the decays. It allows to simulate the angular and time-dependent correlations.

For example, when simulating the decay  $B \rightarrow D^* \tau \bar{\nu}$ ,  $D^* \rightarrow D \pi$ , and  $\tau \rightarrow \pi \nu$ , the decay amplitude can be written as

$$A = \sum_{\lambda_{D^*} \lambda_{\tau}} A_{\lambda_{D^*} \lambda_{\tau}}^{B \rightarrow D^* \tau \bar{\nu}} \times A_{\lambda_{D^*}}^{D^* \rightarrow D \pi} \times A_{\lambda_{\tau}}^{\tau \rightarrow \pi \nu} \quad (4.12)$$

where  $\lambda_{D^*}$  and  $\lambda_{\tau}$  are the states of spin degrees of freedom of the  $D^*$  and  $\tau$ . EvtGen calculates the probabilities from the amplitudes. First, the decay of  $B$  is considered and the probability is calculated with kinematics as

$$P_B = \sum_{\lambda_{D^*} \lambda_{\tau}} |A_{\lambda_{D^*} \lambda_{\tau}}^{B \rightarrow D^* \tau \bar{\nu}}|^2. \quad (4.13)$$

Then, the spin density of  $D^*$ , the probability for  $D^*$ , the probability of  $\tau$ , in that order, are calculated according to the given matrix. The spin and kinematics of the decay are treated based on the given matrix.

In EvtGen framework, the decay matrix is implemented as a "Decay model". Various models are pre-implemented such as specific CP violating channels, Dalitz decay models, mixing, and semi-leptonic form factor models. The other models can be implemented as user-coded modules.

The table of decay chain and models for each decay used in the Belle experiment are based on the decay table of PDG ?? and revised by the Belle generator task force.

## PYTHIA

PYTHIA takes care of hadronization of quarks using the string fragmentation model [69]. The quark pairs ( $u\bar{u}$ ,  $d\bar{d}$ ,  $c\bar{c}$ , and  $s\bar{s}$ ) produced in the  $e^+e^-$  annihilation process initially by EvtGen are fed into PYTHIA and hadrons are formed by the string fragmentation. The hadrons are fed back to EvtGen and decayed following the implemented models.

### 4.5.2 Detector simulation

The particles generated by the event generator are then fed into the detector simulation using GEANT3 package [70].

GEANT3 is a toolkit to simulate the behavior of particles passing through matter in the detector. It gives the detector signal for the particles traversing the detector. It provide the passage of particle and the signal generation in the detectors.

In GEANT3, particles are managed in units of distance, called steps, in material whose three-dimensional position and size are predefined. For an incoming particle, according to its type and four vector, the reaction of the particle as it travels a unit distance is simulated. The probability of decay or scattering at each step is calculated, and if decay occurs, the daughter particles are created with proper four momentum and particle species assigned. If scattering occurs, the four momentum of particle are updated.

The energy loss in the material is calculated considering the ionization and bremsstrahlung. The light emission by Cherenkov and scintillation processes is also simulated based on the various physics models.

### Simulation of signal generation

For GEANT3, the detector is defined as a special part of materials which records the incoming particles or optical photons. Each detector refers to the recorded informations and individually calculate what signal it produces. For example, the cathode of PMT is defined as the special part, and when scintillation or Cherenkov light is incident on it, PMT outputs a signal pulse according to a predefined formula.

### 4.5.3 The sample types of background MC

As mentioned at the beginning of this section, there are three types of MC samples ( $B\bar{B}$ ,  $uds$ , and  $c\bar{c}$ ). These are distinguished by the hadronization from the initial state, as described in the section of PYTHIA.

For  $B\bar{B}$  sample,  $\Upsilon(4S)$  is generated at rest and then decayed by PYTHIA and EvtGen. The  $uds$  and  $c\bar{c}$  are continuum samples from the virtual photon, where the production rate is set to the cross section ratio at 10.58 GeV. In both cases, after hadronization, the samples are decayed by EvtGen according to the Belle decay table.

### 4.5.4 Tracing the MC informations

In the MC simulation, the initial particle decay is processed by EvtGen, and further decays and detection are simulated by GEANT3. The full decay chain is recorded for all generated particles so that we can check whether the tracks used in the reconstruction are correctly reconstructed and identified or not. Using the information, we can check the correctness of the reconstruction.

# Chapter 5

## Signal Reconstruction

For the measurement of  $R$  ratio (Eq. 2.7), the reconstruction of decays of  $D^{*0} \rightarrow D^0 A'$  and  $D^{*0} \rightarrow D^0 \gamma$  is required. The decays are reconstructed using the pions, kaons, electrons (positrons) and gammas, identified as written in the previous chapter. The decay of  $D^{*0}$  into  $D^0 e^+ e^-$  can be the major background to the signal mode since the final state is the same.

In this chapter, we show the reconstruction process of signal events and criteria to exclude the background events based on MC simulations. The details of the signal mode and the parameters to identify the decay are described in Sec. 5.1. The Monte Carlo simulation of the signal decay is given in Sec. 5.2. The reconstruction of the decay is described in Sec. 5.3. Sec. 5.4 describes the method to suppress backgrounds with the detailed criteria. The final candidate selection is written in Sec. 5.5, and the selection is summarized in Sec. 5.6. The reconstruction of the normalization mode is given in Sec. 5.7. The contamination by  $D^{*0} \rightarrow D^0 e^+ e^-$  is mentioned in Sec. 5.8.

### 5.1 Signal mode $D^{*0} \rightarrow D^0 A'$

In this analysis, the dark photon  $A'$  is searched for in the decay  $D^{*0} \rightarrow D^0 A'$ .  $A'$  is supposed to decay to a pair of an electron and a positron. The SM process  $D^{*0} \rightarrow D^0 \gamma$  is used as a normalization mode.

#### 5.1.1 Signal and normalization modes

Around 27% of  $e^+ e^- \rightarrow c\bar{c}$  events includes  $D^{*0}$ .

To reconstruct the decay  $D^{*0} \rightarrow D^0 A'$ , three decay modes of  $D^0$  mesons are used:  $D^0 \rightarrow K^- \pi^+$ ,  $D^0 \rightarrow K^- \pi^+ \pi^0$ , and  $D^0 \rightarrow K^- \pi^+ \pi^- \pi^+$ . The branching fractions of these decays are shown in table 5.1. The sum of these branching fractions are  $26.6 \pm 0.5\%$ .

$D^{*0} \rightarrow D^0 \gamma$  is one of the main decay modes of  $D^{*0}$  and its branching fraction is  $35.3 \pm 0.9\%$  [71].

Table 5.1: The branching fractions of the  $D^0$  decays used for the reconstruction [71].

Mode	Branching fraction
$D^0 \rightarrow K^- \pi^+$	$3.950 \pm 0.031 \%$
$D^0 \rightarrow K^- \pi^+ \pi^0$	$14.4 \pm 0.5\%$
$D^0 \rightarrow K^- \pi^+ \pi^- \pi^+$	$8.23 \pm 0.14\%$

### 5.1.2 Measurement of $R$

The branching fractions of the signal and normalization mode are written using the number of observed signal events  $N_{\text{sig}}$  and  $N_\gamma$  as

$$\text{B}(D^{*0} \rightarrow D^0 A') = \frac{N_{\text{sig}}}{N_{D^{*0}} e_{\text{sig}}} = \frac{N_{\text{sig}}}{2L\sigma_{D^{*0}} \mathcal{B} e_{\text{sig}}} \quad (5.1)$$

$$\text{B}(D^{*0} \rightarrow D^0 \gamma) = \frac{N_{D^{*0}\gamma}}{N_{D^{*0}} e_{D^{*0}\gamma}} = \frac{N_{D^{*0}\gamma}}{2L\sigma_{D^{*0}} \mathcal{B} e_{D^{*0}\gamma}} \quad (5.2)$$

where  $e_{\text{sig}}$  and  $e_{D^{*0}\gamma}$  are the detection efficiencies for the signal  $D^{*0} \rightarrow D^0 A'$  and  $D^{*0} \rightarrow D^0 \gamma$ , respectively,  $L$  is the integrated luminosity,  $\sigma_{D^{*0}}$  is the production cross section of  $D^{*0}$ , 2 is  $e$  charge conjugate factor, and  $\mathcal{B}$  is the  $D^0$  sub decay branching fraction to each mode.

Since the reconstruction procedure of  $D^0$  in these two decays is common, most of the systematics in the  $D^0$  reconstruction can be cancelled out by taking the ratio

$$R = \frac{\text{B}(D^{*0} \rightarrow D^0 A')}{\text{B}(D^{*0} \rightarrow D^0 \gamma)}. \quad (5.3)$$

$R$  can be written as

$$R = \frac{N_{\text{sig}}}{N_{D^{*0}\gamma}} \frac{e_{D^{*0}\gamma}}{e_{\text{sig}}}. \quad (5.4)$$

The relation between the ratio  $R$  and the mixing parameter  $\epsilon$  depends on the theory of dark-SM mixing. For example, if we assume kinetic mixing, the relationship is

$$R = \epsilon^2 \left( 1 - \frac{m_{A'}^2}{(\Delta m)^2} \right) \quad (5.5)$$

where  $\Delta m$  is the square mass difference between  $D^{*0}$  and  $D^0$ , 142 MeV.

### 5.1.3 Decay length of $A'$

In this analysis,  $A'$  is assumed to decay promptly. The decay length depends on the energy in lab frame  $E_{A'}$ , the mixing parameter  $\epsilon$  and the mass  $m_{A'}$  [72].

$$l_{A'} \sim 8 \text{ cm} \frac{E_{A'}}{1 \text{ GeV}} \left( \frac{10^{-4}}{\epsilon} \right)^2 \left( \frac{10 \text{ MeV}}{m_{A'}} \right)^2. \quad (5.6)$$

The energy of  $A'$  from  $D^{*0} \rightarrow D^0 A'$  process in Belle is sub-GeV. The decay length  $l_{A'}$  in Belle spectrometer is estimated to be less than 10  $\mu\text{m}$ , for  $\epsilon \sim 10^{-3}$  and  $m_{A'} > 10 \text{ MeV}$ .

## 5.2 Signal MC Samples

In order to simulate the signal  $D^{*0} \rightarrow DA'$  events, we generate  $e^+e^- \rightarrow c\bar{c}$  events and select events that include  $D^{*0}$  after hadronization by PYTHIA.  $D^{*0}$  is forced to decay into the signal mode by EvtGen. The mass of  $A'$  is set to  $20\text{MeV}/c^2$  in the nominal signal MC samples, signal samples with other  $A'$  mass are also generated for the mass scan analysis as discussed in Chapter 9.

We produce 1,000,000  $c\bar{c}$  events for each sub decay mode of  $D^0$ . The numbers of the obtained signal events are summarized in table 5.2. Assuming  $R = 10^{-6}$ , each sample is equivalent to the luminosity of  $5.5 \times 10^2 \text{ ab}^{-1}$  for  $D^0 \rightarrow K^-\pi^+$  mode,  $1.6 \times 10^2 \text{ ab}^{-1}$  for  $D^0 \rightarrow K^-\pi^+\pi^0$  mode, and  $2.7 \times 10^2 \text{ ab}^{-1}$  for  $D^0 \rightarrow K^-\pi^+\pi^-\pi^+$  mode.

Table 5.2: The numbers of events of the signal MC for 20 MeV  $A'$

Mode	The number of events in signal MC
$D^0 \rightarrow K^-\pi^+$	244,036
$D^0 \rightarrow K^-\pi^+\pi^0$	259,417
$D^0 \rightarrow K^-\pi^+\pi^-\pi^+$	262,707

## 5.3 Signal Event Reconstruction

The reconstruction of  $D^{*0} \rightarrow D^0A'$  is performed in the following steps.

$D^0$  mesons are reconstructed from kaons and pions ( $K^-\pi^+$ ,  $K^-\pi^+\pi^0$ , and  $K^-\pi^+\pi^-\pi^+$ ). They are combined with a pair of electron and positron candidates and the invariant mass of  $D^{*0}$  is calculated. The details are given in following subsections.

### 5.3.1 Criteria for particle identification

The charged tracks are selected by applying following conditions:  $dr < 1 \text{ cm}$  and  $|dz| < 5 \text{ cm}$ . For electrons and positrons,  $|d0| < 0.1 \text{ cm}$  is applied instead of  $dr$  and  $dz$ , where  $|d0|$  is the closest distance to the origin of Belle spectrometer.

Kaons are identified with the criteria  $R(L_K) > 0.6$ ; pions with  $R(L_\pi) > 0.6$ . Electrons and positrons are identified with  $R(L_e) > 0.1$ .

Following selections are applied to photons: the energy cluster is not associated with the tracks,  $E9/E25 > 0.9$ , and  $E_{\text{sum}} > 50 \text{ MeV}$  (barrel) or  $E_{\text{sum}} > 100 \text{ MeV}$  (endcap). Figures 5.1 and 5.2) show the distributions of  $E9/E25$  and  $E_{\text{sum}}$ .

For  $\pi^0$ , Belle standard selection described in Sec. 4.3.2 is applied. Figure 5.3 shows the reconstructed  $\pi^0$  mass and fit result to a Gaussian in the  $D^0 \rightarrow K^-\pi^+\pi^0$  decay. We require  $121 \text{ MeV}/c^2 < m_{\pi^0} < 149 \text{ MeV}/c^2$  for the mass selection (Fig. 5.4). We also require the momentum of  $\pi^0$  to be larger than  $0.4 \text{ GeV}/c$  as shown in Fig. 5.5 and Fig. 5.6.

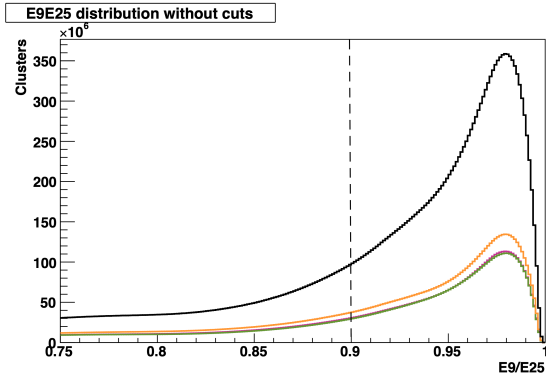


Figure 5.1:  $E9/E25$  distribution of photons from  $\pi^0$  in  $D^0 \rightarrow K^-\pi^+\pi^0$  mode. Orange shows  $uds$ , purple shows  $charm$ , and green shows  $B\bar{B}$ . The dashed lines show the cut values.

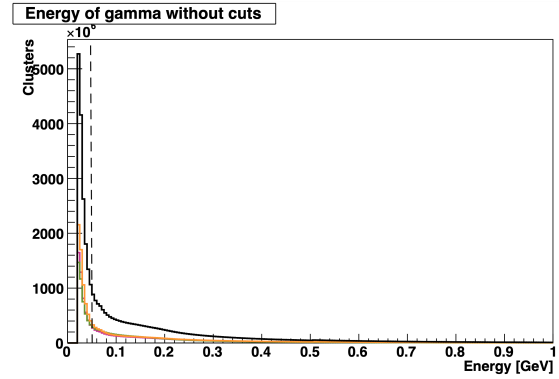


Figure 5.2:  $E_{\text{sum}}$  distribution of photons from  $\pi^0$  in  $D^0 \rightarrow K^-\pi^+\pi^0$  mode. Orange shows  $uds$ , purple shows  $charm$ , and green shows  $B\bar{B}$ . The dashed lines show the cut values.

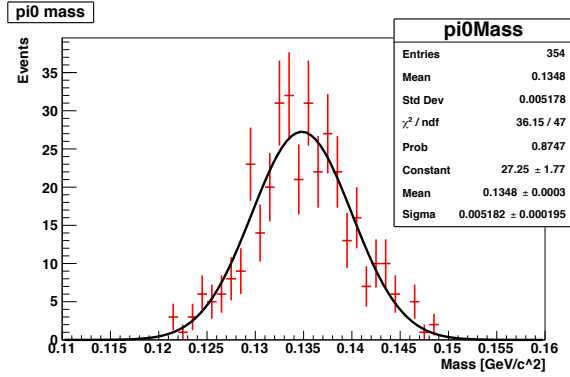


Figure 5.3:  $\pi^0$  mass distribution of  $D^0 \rightarrow K^-\pi^+\pi^0$  mode in the signal MC with all reconstruction and selections. The distribution is fit by the sum of a Gaussian and a linear function.

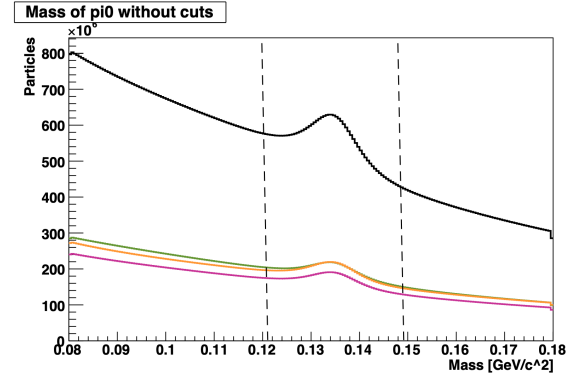


Figure 5.4:  $\pi^0$  mass distribution of  $D^0 \rightarrow K^-\pi^+\pi^0$  mode. Orange shows  $uds$ , purple shows  $charm$ , and green shows  $B\bar{B}$ . The dashed lines show the cut values.

### 5.3.2 $D^0$ reconstruction

$D^0$  mesons are reconstructed using three decay modes:  $D^0 \rightarrow K^-\pi^+$ ,  $D^0 \rightarrow K^-\pi^+\pi^0$ , and  $D^0 \rightarrow K^-\pi^+\pi^-\pi^+$ .

The invariant mass distributions for the reconstructed  $D^0$  for the signal MC samples are shown in Fig 5.7, 5.9, and 5.11. The distribution is fitted by a sum of a Gaussian and a linear functions. We require that the invariant mass is within  $3\sigma$  of the Gaussian distribution, i.e.  $1.850 \text{ GeV}/c^2 < m_{D^0} < 1.881 \text{ GeV}/c^2$  for  $D^0 \rightarrow K^-\pi^+$  mode,  $1.829 \text{ GeV}/c^2 < m_{D^0} < 1.895 \text{ GeV}/c^2$  for  $D^0 \rightarrow K^-\pi^+\pi^0$  mode, and  $1.848 \text{ GeV}/c^2 < m_{D^0} < 1.880 \text{ GeV}/c^2$  for  $D^0 \rightarrow K^-\pi^+\pi^-\pi^+$  mode.

The invariant mass distributions for background MC are shown in Fig. 5.8, Fig. 5.10 and Fig. 5.12.

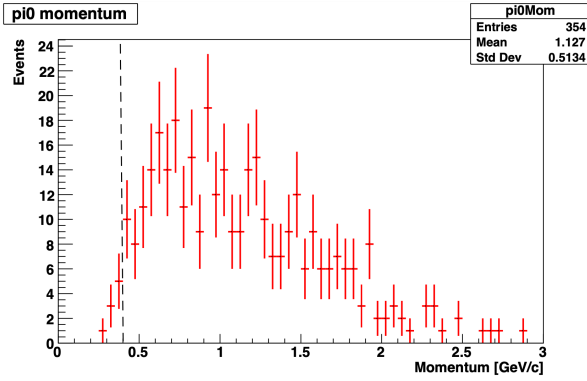


Figure 5.5:  $\pi^0$  momentum distribution of  $D^0 \rightarrow K^- \pi^+ \pi^0$  mode in final result of signal MC with all reconstruction and selections.

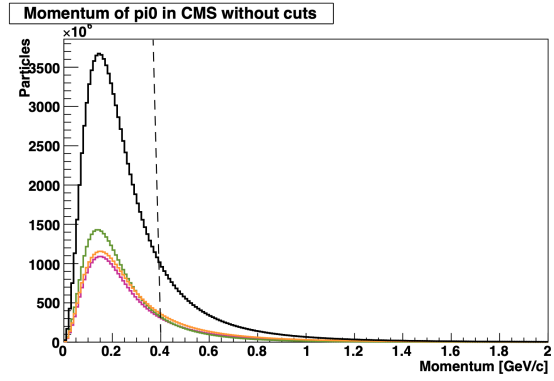


Figure 5.6:  $\pi^0$  momentum distribution in  $D^0 \rightarrow K^- \pi^+ \pi^0$  mode. Orange shows  $uds$ , purple shows  $charm$ , and green shows  $B\bar{B}$ . The dashed lines show the cut values.

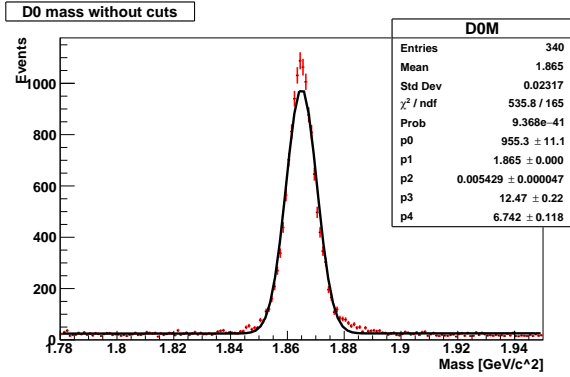


Figure 5.7:  $D^0$  mass distribution of  $D^0 \rightarrow K^- \pi^+$  mode. Red lines show Signal MC distribution and black line shows the fit result by the sum a Gaussian and linear function.

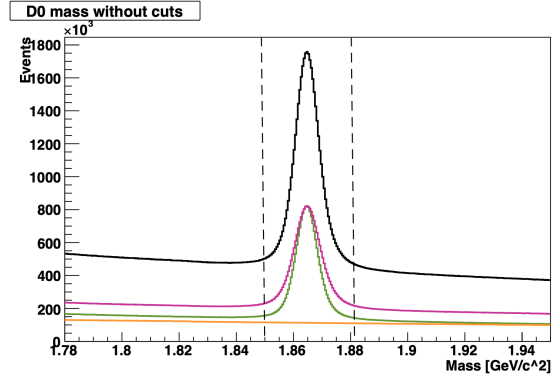


Figure 5.8:  $D^0$  mass distribution in  $D^0 \rightarrow K^- \pi^+$  mode. Orange shows  $uds$ , purple shows  $charm$ , and green shows  $B\bar{B}$ . The dashed lines show the cut values.

### 5.3.3 $D^{*0}$ reconstruction

After the reconstruction of  $D^0$ , a  $D^{*0}$  meson is reconstructed from the  $D^0$  meson and a pair of  $e^+$  and  $e^-$ . Using the four momentums of reconstructed  $D^0$  meson and selected  $e^+$  and  $e^-$ , the CMS momentum ( $p_{D^{*0}}$ ) and invariant mass ( $m_{D^{*0}}$ ) of  $D^{*0}$  are calculated.

First, the momentum selection is applied to exclude backgrounds from  $B\bar{B}$  events.  $D^{*0}$  mesons are also produced in the  $B$  meson decays, however, they are not used in this analysis since their momentum is low and it is difficult to separate them from the background contamination as shown in Fig. 5.14 - 5.18. The  $D^{*0}$  mesons with  $p_{D^{*0}} > 2.5$  GeV/ $c$  are selected in all three  $D^0$  subdecays.

We use the mass difference between  $D^{*0}$  and  $D^0$  mesons ( $\Delta m \equiv m_{D^{*0}} - m_{D^0}$ ) instead of the mass of  $D^{*0}$  for selection, because the uncertainty is cancelled in  $\Delta m$ .

Figure 5.19, 5.20, and 5.21 show the  $\Delta m$  distributions of  $K^- \pi^+$  mode,  $K^- \pi^+ \pi^0$  mode,

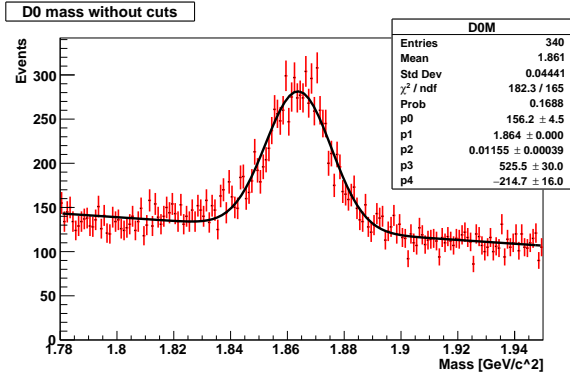


Figure 5.9:  $D^0$  mass distribution of  $D^0 \rightarrow K^-\pi^+\pi^0$  mode. Red lines show Signal MC distribution and black line shows the fit result by the sum a Gaussian and linear function.

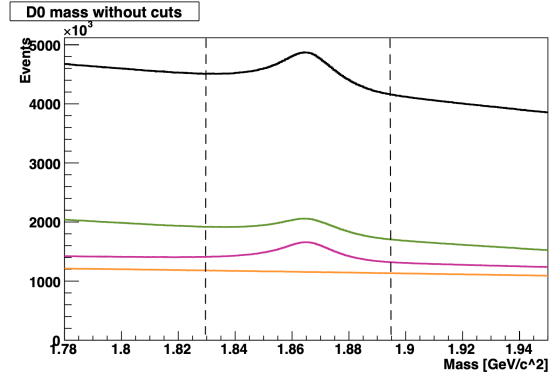


Figure 5.10:  $D^0$  mass distribution in  $D^0 \rightarrow K^-\pi^+\pi^0$  mode. Orange shows  $uds$ , purple shows  $charm$ , and green shows  $B\bar{B}$ . The dashed lines show the cut values.

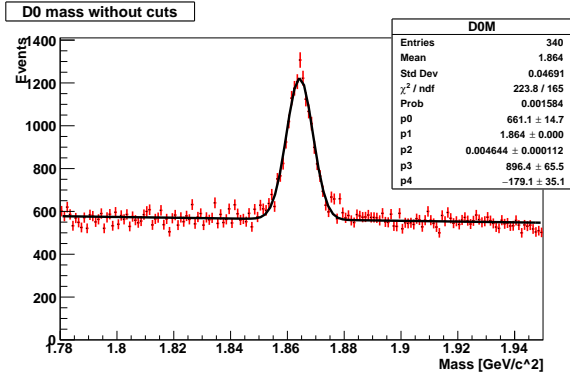


Figure 5.11:  $D^0$  mass distribution of  $D^0 \rightarrow K^-\pi^+\pi^-\pi^+$  mode. Red lines show Signal MC distribution and black line shows the fit result by the sum a Gaussian and linear function.

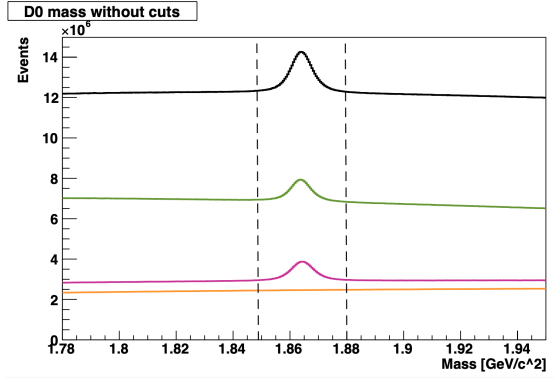


Figure 5.12:  $D^0$  mass distribution in  $D^0 \rightarrow K^-\pi^+\pi^-\pi^+$  mode. Orange shows  $uds$ , purple shows  $charm$ , and green shows  $B\bar{B}$ . The dashed lines show the cut values.

and  $K^-\pi^+\pi^-\pi^+$  mode, respectively. We apply  $134.6 \text{ MeV}/c^2 < \Delta m < 150.8 \text{ MeV}/c^2$  to all the modes, which corresponds to  $3\sigma$  of the signal peak.

The selection criteria on  $D^{*0}$  are summarized in table 5.3.

## 5.4 Background Suppression

After the reconstruction, following selections are applied on  $D^{*0}$  candidates to suppress the background: charged  $D^{*0}$  veto,  $ee$  vertex, and  $\chi^2$  of mass constraint vertex fit.

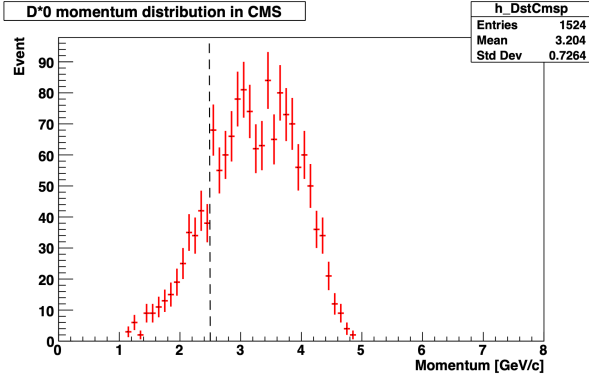


Figure 5.13:  $p_{D^{*0}}$  distribution of  $D^0 \rightarrow K^- \pi^+$  mode in signal MC. The dashed lines show the cut values.

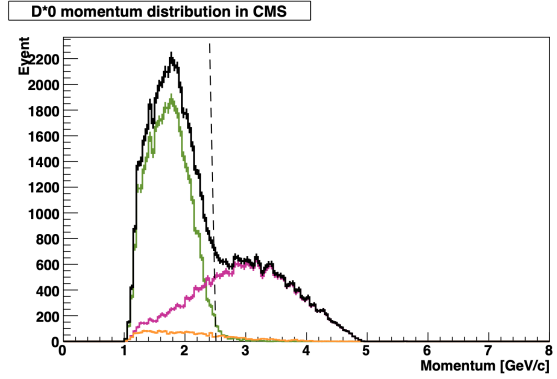


Figure 5.14:  $p_{D^{*0}}$  distribution of  $D^0 \rightarrow K^- \pi^+$  mode. Orange shows  $uds$ , purple shows  $charm$ , and green shows  $B\bar{B}$ . The dashed lines show the cut values.

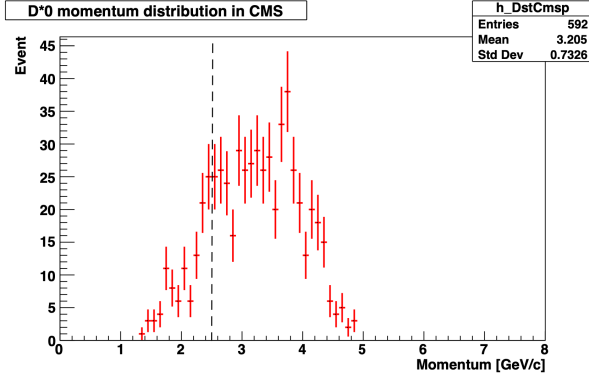


Figure 5.15:  $p_{D^{*0}}$  distribution of  $D^0 \rightarrow K^- \pi^+ \pi^0$  mode in signal MC. The dashed lines show the cut values.

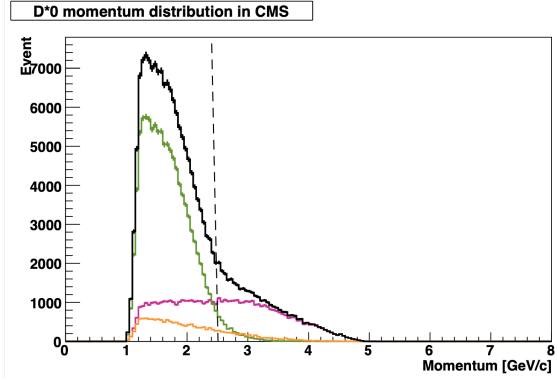


Figure 5.16:  $p_{D^{*0}}$  distribution of  $D^0 \rightarrow K^- \pi^+ \pi^0$  mode. Orange shows  $uds$ , purple shows  $charm$ , and green shows  $B\bar{B}$ . The dashed lines show the cut values.

### 5.4.1 FoM for the optimization of selection criteria

For each selection, we optimize the criteria by maximizing the figure of merit (FoM) defined as

$$\text{FoM} = \frac{e_{\text{sig}}}{a/2 + \sqrt{N_{\text{bkg}}}} \quad (5.7)$$

where  $e_{\text{sig}}$  is the signal efficiency,  $a$  is the number of sigmas corresponding to the significance and  $N_{\text{bkg}}$  is the number of events of background MC in the signal region [73]. In this analysis,  $a$  is set to 3.

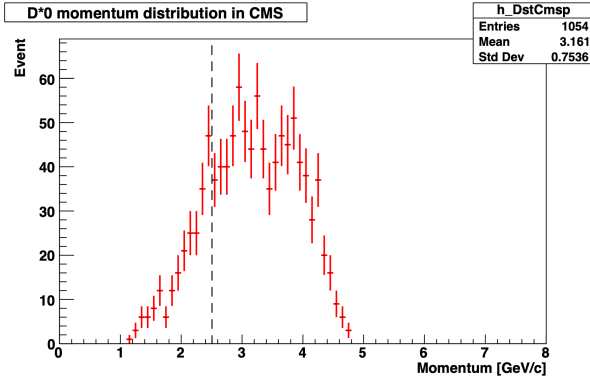


Figure 5.17:  $p_{D^{*0}}$  distribution of  $D^0 \rightarrow K^- \pi^+ \pi^- \pi^+$  mode in signal MC. The dashed lines show the cut values.

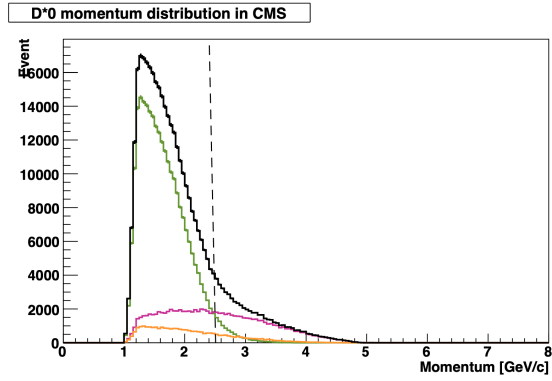


Figure 5.18:  $p_{D^{*0}}$  distribution of  $D^0 \rightarrow K^- \pi^+ \pi^- \pi^+$  mode. Orange shows  $uds$ , purple shows  $charm$ , and green shows  $B\bar{B}$ . The dashed lines show the cut values.

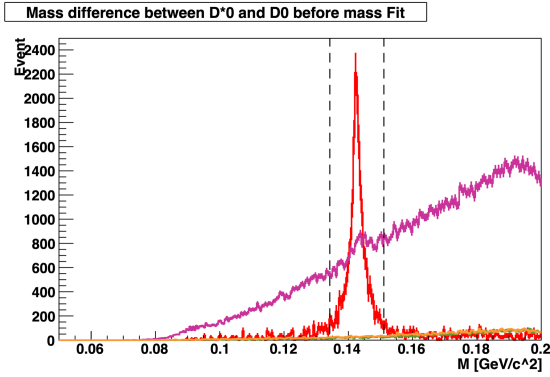


Figure 5.19:  $\Delta m$  distribution of  $D^0 \rightarrow K^- \pi^+$  mode. Red line shows scaled signal MC, orange shows  $uds$ , purple shows  $charm$ , and green shows  $B\bar{B}$ . The dashed lines show the cut values.

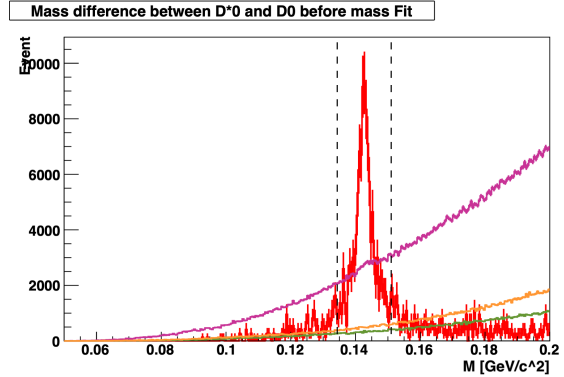


Figure 5.20:  $\Delta m$  distribution of  $D^0 \rightarrow K^- \pi^+ \pi^0$  mode. Red line shows scaled signal MC, orange shows  $uds$ , purple shows  $charm$ , and green shows  $B\bar{B}$ . The dashed lines show the cut values.

## 5.4.2 Contamination of $D^{*+} \rightarrow D^0 \pi^+$

### Backgrounds from charged $D^*$

The process  $D^{*+} \rightarrow D^0 \pi^+$  becomes background when  $\pi^+$  is mis-identified as  $e^+$  and an additional electron in the event is picked up as illustrated in Fig. 5.22. To reject this background,  $D^*$  hypothesis mass  $m_{D^{*+}(D^0 \pi^+)}$  is calculated assigning  $\pi^+$  mass to an  $e^+$  track used in the reconstruction of  $D^{*0}$ .

The distributions of  $m_{D^{*+}}$  are shown in the left plot of Fig. 5.23 - 5.25. The backgrounds have peaks at  $2.01 \text{ GeV}/c^2$ , the mass of  $D^{*+}$ , while the signals do not. The mass difference  $\Delta m_{D^{*+}}$  between the hypothesis mass  $m_{D^{*+}(D^0 \pi^+)}$  and the mass of  $D^0$  used in the reconstruction is also calculated, If the  $D^{*0}$  candidate is reconstructed from the charged  $D^*$  process,  $\Delta m_{D^{*+}}$  should have peak at  $142 \text{ MeV}$ , the mass of  $\pi^+$ .

The veto is done using  $\Delta m_{D^{*+}}$  instead of the  $m_{D^{*+}}$ , in order to avoid the uncertainty in

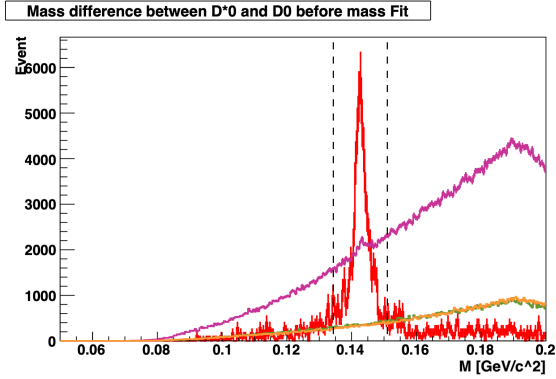


Figure 5.21:  $\Delta m$  distribution of  $D^0 \rightarrow K^- \pi^+ \pi^- \pi^+$  mode. Red line shows scaled signal MC, orange shows  $uds$ , purple shows  $charm$ , and green shows  $B\bar{B}$ . The dashed lines show the cut values.

Table 5.3: The selection criteria on  $D^0$  and  $D^{*0}$  in each mode

Mode	$\sigma_{M_{D^0}}$ [MeV]	$M_{D^0}$ selection [ $\text{GeV}/c^2$ ]	$\sigma_{\Delta M}$ [MeV]	$\Delta M$ selection [MeV]
$D^0 \rightarrow K^- \pi^+$	$5.34 \pm 0.05$	$1.849 < m_{D^0} < 1.881$	$2.7 \pm 0.1$	$134.6 < \Delta m < 150.9$
$D^0 \rightarrow K^- \pi^+ \pi^0$	$11.5 \pm 0.4$	$1.830 < m_{D^0} < 1.898$		
$D^0 \rightarrow K^- \pi^+ \pi^- \pi^+$	$4.6 \pm 0.1$	$1.850 < m_{D^0} < 1.878$		

the reconstructed  $D^0$  mass. The peak structure in  $D^{*+}$  mass is sharper in  $\Delta m_{D^{*+}}$  than that in  $m_{D^{*+}}(D^0 \pi^+)$  as seen from the left and middle plots in Fig. 5.23 - 5.25.

### Optimization of selection criteria

The selection criteria are optimized using FoM as shown in the right plots in Fig. 5.23 - 5.25. The FoM shown in Eq. 5.7 is calculated by excluding the events with lower  $\Delta m_{D^{*+}}$  than the threshold. The highest FoM values are at;  $\Delta m_{D^{*+}} = 150.6 \text{ MeV}/c^2$  for  $D^0 \rightarrow K^- \pi^+$  mode,  $\Delta m_{D^{*+}} = 150.6 \text{ MeV}/c^2$  for  $D^0 \rightarrow K^- \pi^+ \pi^0$  mode and  $\Delta m_{D^{*+}} = 149.9 \text{ MeV}/c^2$  for  $D^0 \rightarrow K^- \pi^+ \pi^- \pi^+$  mode.  $\Delta m_{D^{*+}} > 150.6 \text{ MeV}/c^2$  is used for the selection value for all sub decay modes.

### Check by MC information

Figure 5.26 shows the type of the events excluded by the charged veto  $\Delta m_{D^{*+}} > 150.6 \text{ MeV}/c^2$  traced by the Monte Carlo information. The histograms show whether each event contains decay of  $D^{*+} \rightarrow D^0 \pi^+$  (bin 1),  $D^{*-} \rightarrow D^0 \pi^-$  (bin 2) or no charged  $D^*$  (bin -1). As seen, two-third of the excluded events come from charged  $D^*$ .

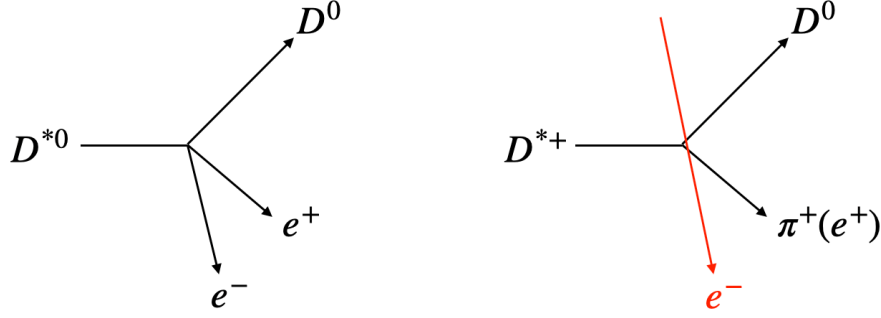


Figure 5.22: Image of charged  $D^*$  background. Left is the signal mode. Right show the background. There is a decay of  $D^{*+} \rightarrow D^0\pi^+$  where the  $\pi^+$  is mis-identified as  $e^+$  and an  $e^-$  track (red one) comes from somewhere accidentally crossing the decay vertex of  $D^{*+}$ .

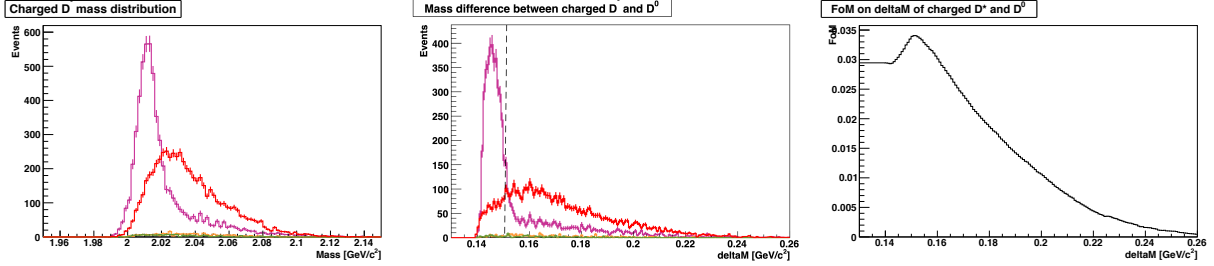


Figure 5.23: The distribution of  $D^{*+}$  hypothesis mass (left) and  $\Delta m_{D^{*+}}$  (center) in  $D^0 \rightarrow K^-\pi^+$  mode in MC. Red shows the signal, orange shows  $uds$ , purple shows  $charm$ , and green shows  $B\bar{B}$ . The dashed lines show the cut values. And FoM transition of  $\Delta m_{D^{*+}}$  distribution (right).

### 5.4.3 Contamination of $D^{*0} \rightarrow D^0 + \pi^0/\gamma$

#### ee vertex selection

$D^{*0} \rightarrow D^0\pi^0(\rightarrow \gamma\gamma)$  and  $D^{*0} \rightarrow D^0\gamma$  become backgrounds if the conversion of a photon to an electron-positron pair occurs by the interaction with a detector material. In such a case, the vertex of  $e^+e^-$  is apart from IP, unlike the signal where  $A'$  decays promptly to  $e^+e^-$ .

The vertex of  $e^+e^-$  is calculated with no mass and IP constraints by a kinematic fitting package called KFitter [74]. Figure 5.27 shows the distributions of the radial distance  $dr$  between the calculated vertex and the interaction point. As shown in the figure, signal events distribute in smaller  $dr$  than the background events. Signal events can be enhanced by excluding events with  $dr$  above a certain threshold.

#### Optimization of Criteria

Figure 5.27 - 5.29 show the distributions of  $dr$  in each mode. We apply the selection values of  $dr$  with highest FoM values;  $dr < 0.44$  cm for  $D^0 \rightarrow K^-\pi^+$  mode,  $dr < 0.66$  cm for  $D^0 \rightarrow K^-\pi^+\pi^0$  mode and  $dr < 0.64$  cm for  $D^0 \rightarrow K^-\pi^+\pi^-\pi^+$  mode.

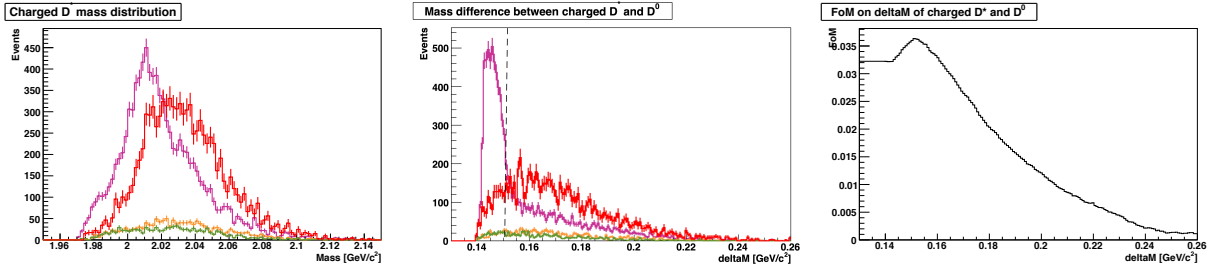


Figure 5.24: The distribution of  $D^{*+}$  hypothesis mass (left) and  $\Delta m_{D^{*+}}$  (center) in  $D^0 \rightarrow K^- \pi^+ \pi^0$  mode in MC. Orange shows  $uds$ , purple shows  $charm$ , and green shows  $B\bar{B}$ . The dashed lines show the cut values. And FoM transition of  $\Delta m_{D^{*+}}$  distribution (right).

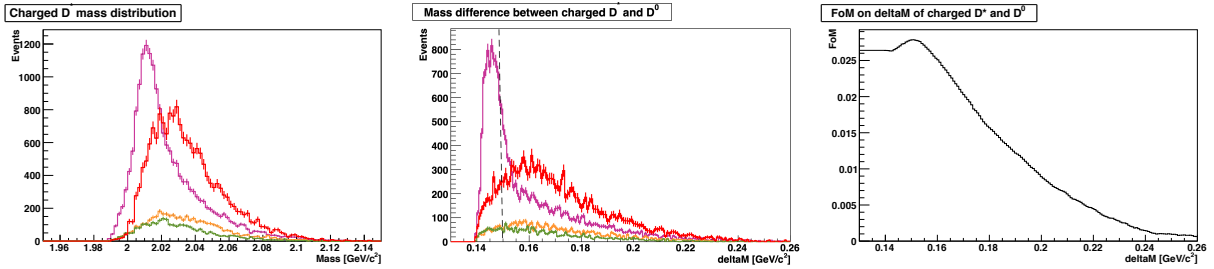


Figure 5.25: The distribution of  $D^{*+}$  hypothesis mass (left) and  $\Delta m_{D^{*+}}$  (center) in  $D^0 \rightarrow K^- \pi^+ \pi^- \pi^+$  mode in MC. Orange shows  $uds$ , purple shows  $charm$ , and green shows  $B\bar{B}$ . The dashed lines show the cut values. And FoM transition of  $\Delta m_{D^{*+}}$  distribution (right).

## Check by MC informations

We check whether the excluded events are  $D^{*0} \rightarrow D^0 \gamma$  events or not by the MC information. Figure 5.30 shows the type of events in  $1 \text{ cm} < dr < 3 \text{ cm}$ , which do not pass the selection for all the  $D^0$  decay modes. The histogram show whether each event includes decay of  $D^{*0} \rightarrow D^0 \gamma$  (bin 1),  $\bar{D}^{*0} \rightarrow \bar{D}^0 \gamma$  (bin 2) or neither of them (bin -1). Two-third of charm background events come from  $D^{*0} \rightarrow D^0 \gamma$ . The  $m_{A'}$  distribution of events excluded by the  $dr$  selection is shown in Fig. 5.31. The excluded events distribute in low mass region and mainly come from charm and  $D^{*0} \rightarrow D^0 e^+ e^-$  as described in Sec. 5.8.

### 5.4.4 Mass constraint vertex fit on $D^{*0}$

The mass constraint fit of vertex is done for the reconstructed  $D^{*0}$  candidates by KFitter [74]. The mass is fixed at the reconstructed particle,  $1.865 \text{ GeV}/c^2$  for  $D^0$  and  $2.007 \text{ GeV}/c^2$  for  $D^{*0}$ , and the vertex position is left free as a fit parameter. Track parameters are modified assuming all tracks come from the vertex calculated by the mass constraint vertex fit on  $D^{*0}$ . This mass constraint vertex fit and track modification is done after all the selections, so there is no effect and distortion in the selections. On the other hand,  $A'$  is reconstructed using the modified  $e^+ e^-$  tracks, and the width of the signal becomes narrower.

The chi-square  $\chi_{D^{*0}}^2$  indicates how well the daughter tracks are fitted.

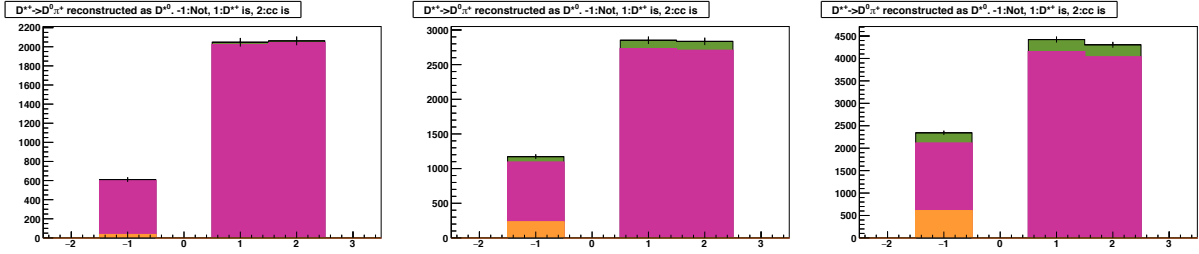


Figure 5.26: The MC information of events excluded by the charged  $D^*$  veto in each mode. Left is  $D^0 \rightarrow K^- \pi^+$ , center is  $D^0 \rightarrow K^- \pi^+ \pi^0$ , and right is  $D^0 \rightarrow K^- \pi^+ \pi^- \pi^+$ . Bin 1 is event including  $D^{*+} \rightarrow D^0 \pi^+$ , bin 2 is  $D^{*-} \rightarrow \bar{D}^0 \pi^-$ , and bin -1 is not including. Orange shows  $uds$ , purple shows  $charm$ , green shows  $B\bar{B}$ , and blue shows  $ee$ .

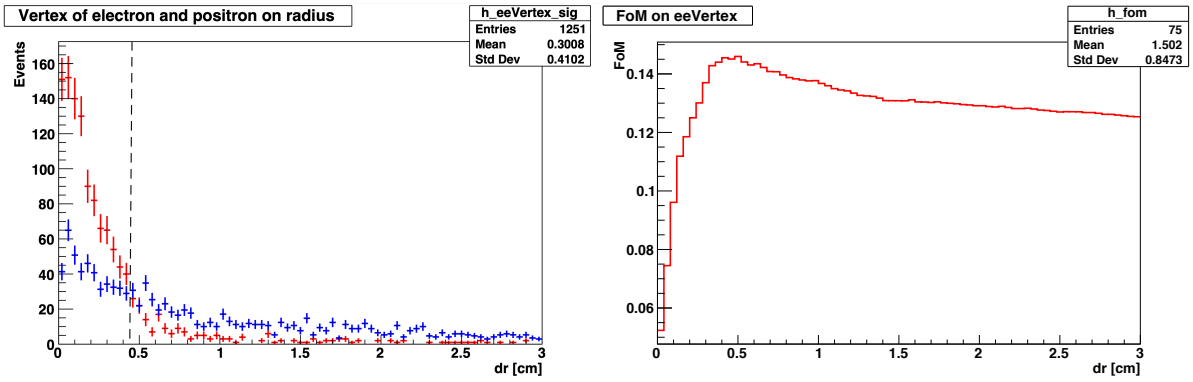


Figure 5.27: Left :  $dr$  of  $ee$  vertex distribution of  $D^0 \rightarrow K^- \pi^+$  mode normalized by the number of entries. Red line shows Signal MC, blue line shows backgrounds. Right : FoM transition of  $ee$  vertex output value distribution.

### Mass constraint vertex fit on $D^0$

For the fit to  $D^{*0}$ ,  $\chi^2$  of its daughter particles must be known. Before the fit to  $D^{*0}$ , the fit to  $D^0$  is performed for the final state particles;  $K, \pi$ .

$\chi^2$  is defined as

$$\chi_{D^0}^2 = \left( \vec{m}(\vec{x}) - \vec{h} \right) V^{-1} \left( \vec{m}(\vec{x}) - \vec{h} \right)^T \quad (5.8)$$

where  $\vec{m}$  is the parameters of  $D^0$  calculated from  $\vec{x}$  which is the measured track parameters of the final state particles,  $\vec{h}$  is a hypothesis of  $D^0$  parameters, and  $V$  is the covariance matrix of the measurement.

The parameters  $\vec{h}$  is determined by minimizing  $\chi_{D^0}^2$ ,

$$\frac{\partial \chi_{D^0}^2}{\partial \vec{x}} = 0. \quad (5.9)$$

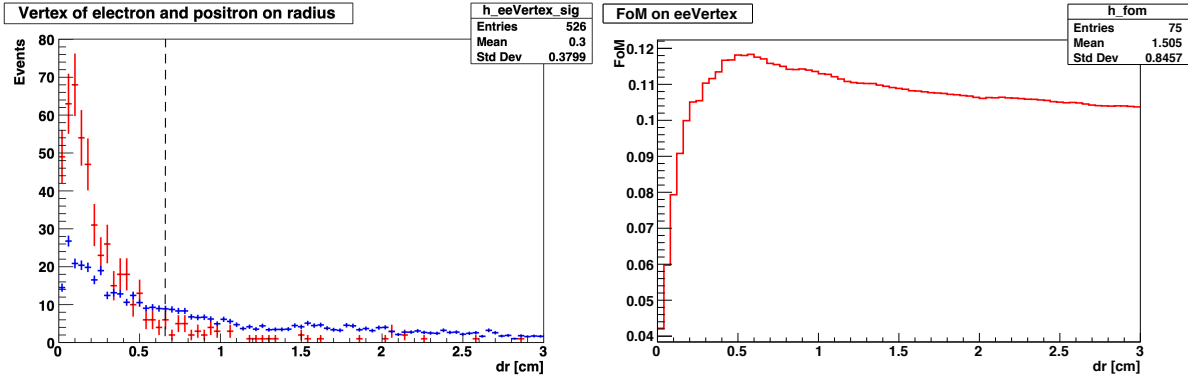


Figure 5.28: Left :  $dr$  of  $ee$  vertex distribution of  $D^0 \rightarrow K^- \pi^+ \pi^0$  mode normalized by the number of entries. Red line shows Signal MC, blue line shows backgrounds. Right : FoM transition of  $ee$  vertex output value distribution.

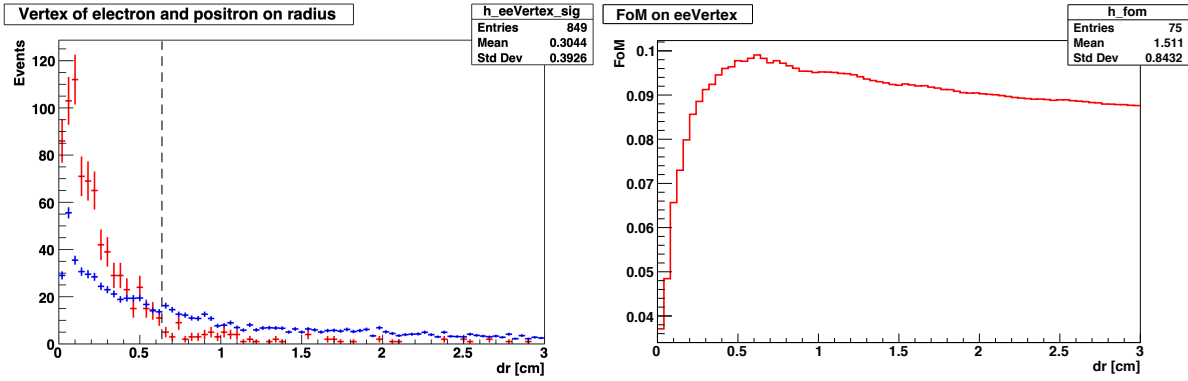


Figure 5.29: Left :  $dr$  of  $ee$  vertex distribution of  $D^0 \rightarrow K^- \pi^+ \pi^- \pi^+$  mode normalized by the number of entries. Red line shows Signal MC, blue line shows backgrounds. Right : FoM transition of  $ee$  vertex output value distribution.

### Mass constraint vertex fit on $D^{*0}$

Mass constraint vertex fit is performed to  $D^{*0}$ . Here, the parameter vector  $\vec{x}$  includes not only the measured track parameters of  $e^+$  and  $e^-$  but also reconstructed  $D^0$  parameters and  $\chi_{D^0}$  calculated above. The distributions of  $\chi^2$  derived by the degrees of freedom,  $\chi_{D^{*0}}^2/ndf$ , are shown in Fig. 5.32 - 5.34.

We require  $\chi_{D^{*0}}^2/ndf > 0.001$  for all modes.

After all, the four momenta of (grand)daughter particles are updated so that the tracks come from the vertex.

## 5.5 Best candidate selection

Finally, the best candidate selection is applied.

There are cases that multiple candidates remain in a single event after all the selections

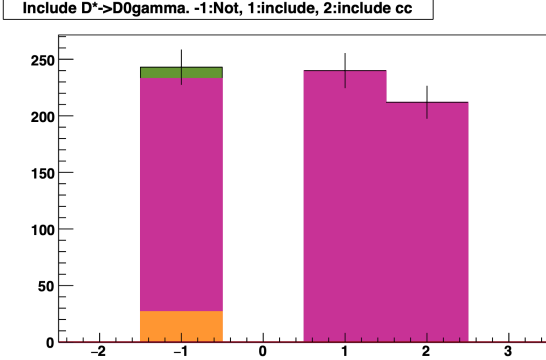


Figure 5.30: The MC truth of  $1 < dr < 3$  cm events. Bin 1 is event including  $D^{*0} \rightarrow D^0 e^+ e^-$ , bin 2 is  $\overline{D}^{*0} \rightarrow \overline{D}^0 e^- e^+$ , and bin -1 is not including. Orange shows *uds*, purple shows *charm*, green shows  $B\overline{B}$ , and blue shows  $D^{*0} \rightarrow D^0 e^+ e^-$ .

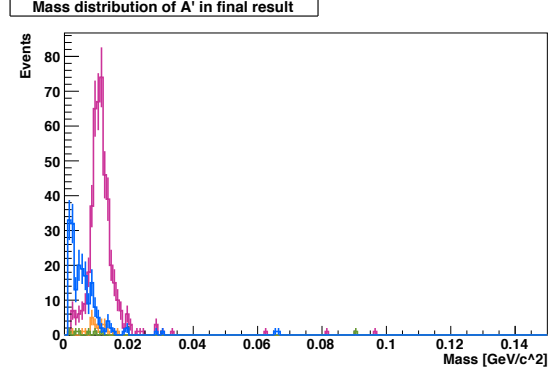


Figure 5.31: The reconstructed  $A'$  mass of  $1 \text{ cm} < dr < 3 \text{ cm}$  events. Orange shows *uds*, purple shows *charm*, green shows  $B\overline{B}$ , and blue shows  $D^{*0} \rightarrow D^0 e^+ e^-$ .

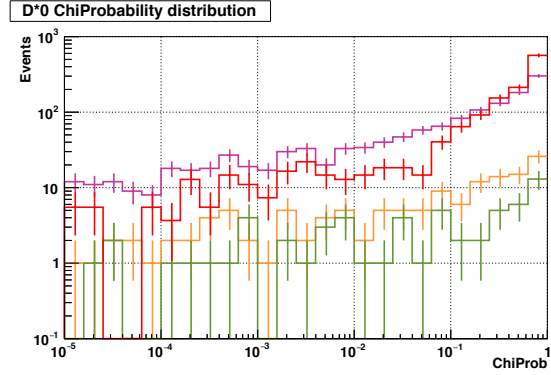
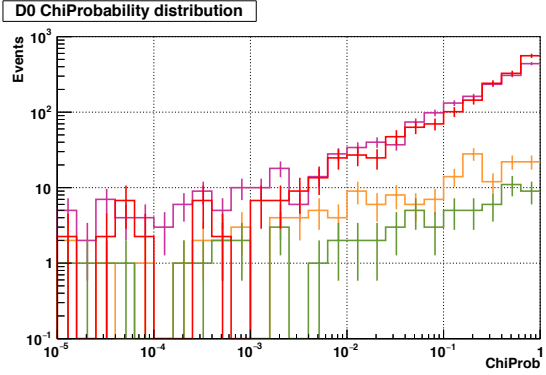


Figure 5.32:  $\chi_{D^0}^2$  (left) and  $\chi_{D^{*0}}^2$  (right) distributions of  $D^0 \rightarrow K^- \pi^+$  mode. Red shows the signal, orange shows *uds*, purple shows *charm*, green shows  $B\overline{B}$ .

are applied. In such a case, the candidate with the highest  $\chi_{D^{*0}}^2/ndf$  is chosen and the other candidates are excluded.

The numbers of candidates per each event in average are summarized in table 5.4.

## 5.6 Selection summary

The selections in each mode are summarized in table 5.5. The efficiencies of signal after each selection is shown in table 5.6. Note that the selections of tracks, the sub decays branching fractions of  $\pi^0$  (Sec. 5.3.1), and  $D^0$  (Sec. 5.3.2) are included in the reconstruction efficiency.

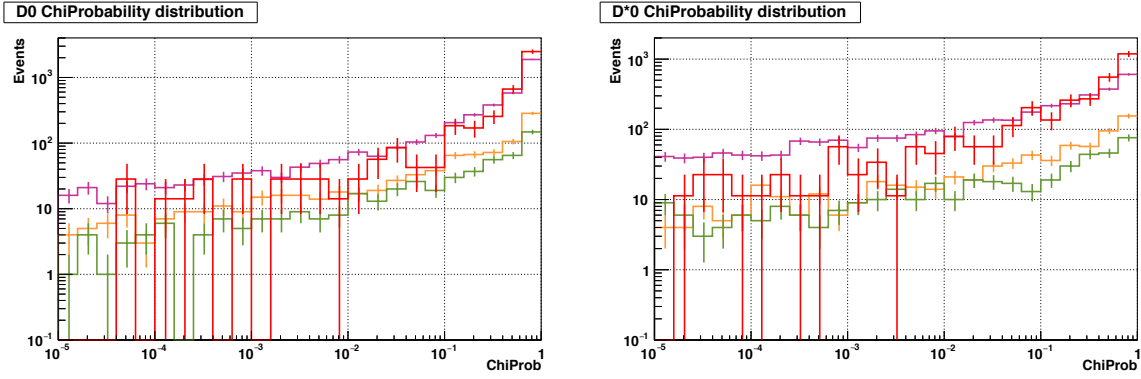


Figure 5.33:  $\chi_{D^0}^2$  (left) and  $\chi_{D^{*0}}^2$  (right) distributions of  $D^0 \rightarrow K^- \pi^+ \pi^0$  mode. Red shows the signal, orange shows  $uds$ , purple shows  $charm$ , green shows  $B\bar{B}$ .

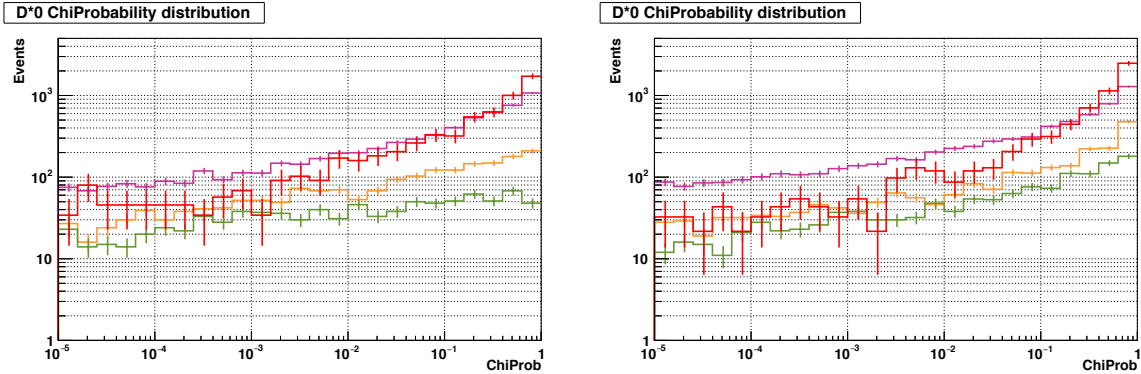


Figure 5.34:  $\chi_{D^0}^2$  (left) and  $\chi_{D^{*0}}^2$  (right) distributions of  $D^0 \rightarrow K^- \pi^+ \pi^- \pi^+$  mode. Red shows the signal, orange shows  $uds$ , purple shows  $charm$ , green shows  $B\bar{B}$ .

## 5.7 The reconstruction of normalization mode $D^{*0} \rightarrow D^0 \gamma$

The reconstruction process of the normalization mode is the same as that for the signal mode except the  $D^{*0}$  reconstruction.

### 5.7.1 $D^0$ reconstruction

$D^0$  reconstruction and  $D^0$  mass selection are the same as those for the signal mode for each  $D^0$  decay (Sec. 5.3.1, 5.3.2). Tracks with  $dr < 1$  cm and  $|dz| < 5$  cm are selected and  $K/\pi$  selection  $R(L_K) > 0.6$  and  $R(L_\pi) > 0.6$  are applied for kaons and pions. The mass and momentum criteria for  $\pi^0$  in  $D^0 \rightarrow K^- \pi^+ \pi^0$  are  $121 \text{ MeV}/c^2 < m_{\pi^0} < 149 \text{ MeV}/c^2$  and  $0.4 \text{ GeV}/c < p_{\pi^0}$ . The criteria for  $D^0$  mass  $m_{D^0}$  are  $1.850 \text{ GeV}/c^2 < m_{D^0} < 1.881 \text{ GeV}/c^2$  for  $D^0 \rightarrow K^- \pi^+$ ,  $1.829 \text{ GeV}/c^2 < m_{D^0} < 1.895 \text{ GeV}/c^2$  for  $D^0 \rightarrow K^- \pi^+ \pi^0$ , and  $1.848 \text{ GeV}/c^2 < m_{D^0} < 1.880 \text{ GeV}/c^2$  for  $D^0 \rightarrow K^- \pi^+ \pi^- \pi^+$ .

Table 5.4: The number of candidates per event in average

Sub decay mode	$K^-\pi^+$	$K^-\pi^+\pi^0$	$K^-\pi^+\pi^-\pi^+$
Signal MC	1.005	1.030	1.004
Background MC	1.008	1.044	1.041

Table 5.5: Selections in each mode

Mode	Selection	Figure of distribution
$D^0 \rightarrow K^-\pi^+$	$1.857 < m_{D^0} < 1.878 \text{ GeV}/c^2$	Fig. 5.7
	$134.6 < \Delta m < 150.9 \text{ MeV}$	Fig. 5.19
	$2.5 < p_{D^{*0}} \text{ GeV}/c$	Fig. 5.14
	$dr_{ee} < 0.44 \text{ cm}$	Fig. 5.27
$D^0 \rightarrow K^-\pi^+\pi^0$	$121 < m_{\pi^0} < 149 \text{ MeV}$	Fig. 5.3
	$1.849 < m_{D^0} < 1.876 \text{ GeV}/c^2$	Fig. 5.9
	$134.6 < \Delta m < 150.9 \text{ MeV}$	Fig. 5.20
	$2.5 < p_{D^{*0}} \text{ GeV}/c$	Fig. 5.16
	$dr_{ee} < 0.66 \text{ cm}$	Fig. 5.28
$D^0 \rightarrow K^-\pi^+\pi^+\pi^-$	$1.859 < m_{D^0} < 1.873 \text{ GeV}/c^2$	Fig. 5.11
	$134.6 < \Delta m < 150.9 \text{ MeV}$	Fig. 5.21
	$2.5 < p_{D^{*0}} \text{ GeV}/c$	Fig. 5.18
	$dr_{ee} < 0.64 \text{ cm}$	Fig. 5.29

### 5.7.2 $D^{*0}$ reconstruction

After the  $D^0$  reconstruction,  $D^{*0}$  meson is reconstructed from  $D^0$  and  $\gamma$ .

The selection  $p_{D^{*0}} > 2.5 \text{ GeV}/c$  is applied in the same way as the signal mode. Other selections used for the signal mode such as the charged veto are not applied to the normalization mode.

## 5.8 The background $D^{*0} \rightarrow D^0 e^+ e^-$ process

### 5.8.1 The decay of $D^{*0} \rightarrow D^0 e^+ e^-$ in the Standard Model

In the SM, the decay  $D^{*0} \rightarrow D^0 e^+ e^-$  is not forbidden. The final state of this decay is the same as the signal. Though the branching fraction is not measured, this process is suppressed by  $\alpha_{EM}$  compared to  $D^{*0} \rightarrow D^0 \gamma$  and the branching fraction is expected to be  $\alpha_{EM} \times BR(D^{*0} \rightarrow D^0 \gamma)$ , which is larger than  $D^{*0} \rightarrow D^0 A'$ . So, this process is not negligible

Table 5.6: Signal efficiencies after reconstruction and each selection

Selection	$D^0 \rightarrow K\pi$	$D^0 \rightarrow K\pi\pi$	$D^0 \rightarrow K\pi\pi\pi$
Reconstruction	9.3 %	5.0 %	18.6 %
$m_{D^0}$	8.6 %	3.7 %	8.3 %
$p_{D^{*0}}$	6.6 %	2.6 %	5.5 %
$\Delta m$	5.3 %	1.7 %	3.7 %
$dr_{ee}$	4.1 %	1.5 %	3.1 %
$D^{*+}$ veto	3.1 %	1.3 %	2.6 %
$\text{prob}(\chi^2_{D^{*0}}, ndf)$	2.8 %	1.1 %	2.2 %
Best candidate selection	2.8 %	1.0 %	2.1 %

<sup>1</sup>. We generate a MC sample of this decay by EvtGen in a similar way as the signal MC, because this decay is not included the Belle generic MC. The pdf is discussed in Appendix. A.2.

### 5.8.2 Differences from the signal mode

Figures 5.35 - 5.38 show the distributions of variables used in background reduction. This process cannot be distinguished from the signal with these variables.

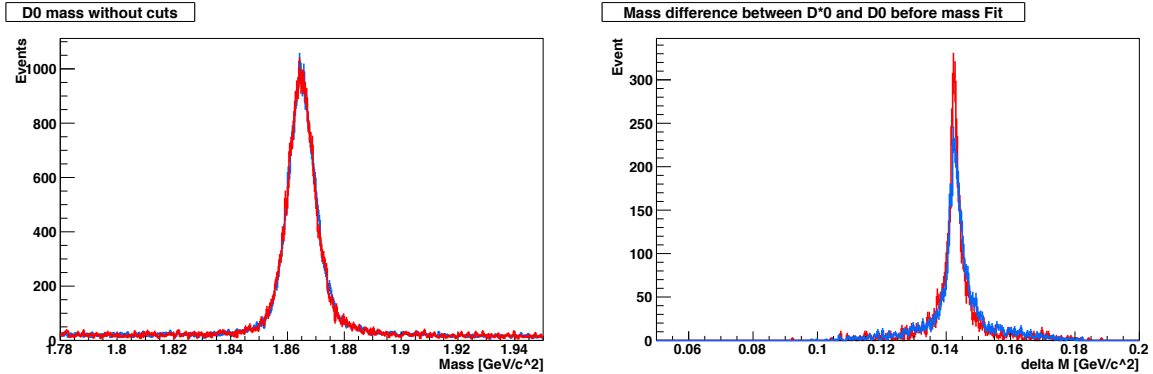


Figure 5.35: The  $D^0$  mass distribution of  $D^{*0} \rightarrow D^0 e^+ e^-$  (blue) and signal (red) in MC. The distributions are normalized by the number of entries.

Figure 5.36: The  $\Delta m$  distribution of  $D^{*0} \rightarrow D^0 e^+ e^-$  (blue) and signal (red) in MC. The distributions are normalized by the number of entries.

<sup>1</sup>This process can occur quantum interference with the signal because of the same final state. But, as mentioned in Sec. 5.1, the decay width of  $A'$  is narrow and the interference is negligible.

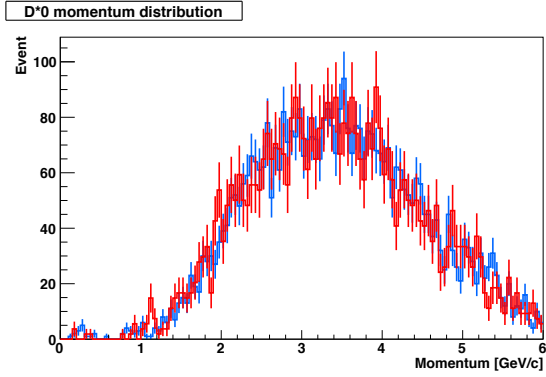


Figure 5.37: The  $D^{*0}$  momentum distribution of  $D^{*0} \rightarrow D^0 e^+ e^-$  (blue) and signal (red) in MC. The distributions are normalized by the number of entries.

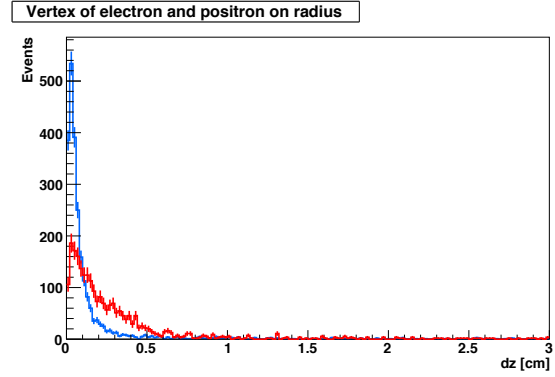


Figure 5.38: The  $dz$  of  $ee$  vertex distribution of  $D^{*0} \rightarrow D^0 e^+ e^-$  (blue) and signal (red) in MC. The distributions are normalized by the number of entries.

# Chapter 6

## Estimation of signal yield by MC simulation

In this chapter the procedure to obtain the signal yield is discussed step by step using the Monte Carlo events.

The distribution of  $m_{A'}$  reconstructed from an  $e^+e^-$  pair is fitted with a sum of the shape functions for the signal and backgrounds obtained by the MC. The yield of  $A'$  is obtained from the fit (Sec. 6.1 - 6.3).

### 6.1 Signal shape and efficiencies

Figures 6.1 - 6.3 are the  $A'$  mass distributions for the signal MC generated with  $m_{A'} = 20$  MeV/ $c^2$ . The distributions show a peak at 20 MeV/ $c^2$ . We model the distribution by

$$f_{\text{sig}}(m_{A'}) = C_{\text{sig}}G(m_{A'}; \mu, \sigma) + (1 - C_{\text{sig}})G_b(m_{A'}; \mu, \sigma_L, \sigma_R) \quad (6.1)$$

where  $G(m_{A'}; \mu, \sigma)$  is a gaussian with a mean  $\mu$  and a standard deviation  $\sigma$ ,  $G_b(m_{A'}; \mu, \sigma_L, \sigma_R)$  is a bifurcated Gaussian with a mean  $\mu$ , a left width  $\sigma_L$  and a right width  $\sigma_R$ , and  $C_{\text{sig}}$  is a fraction of the two Gaussians.

The fit to the distribution is done with RooFit package [75].

The distributions are fitted to  $N_{\text{sig}} \times f_{\text{sig}}(m_{A'})$  where  $N_{\text{sig}}$  is the number of signal, floating  $N_{\text{sig}}$ ,  $\mu$ ,  $\sigma$ ,  $\sigma_L$ ,  $\sigma_R$ , and  $C_{\text{sig}}$ . The fit results are shown in Fig. 6.1 - 6.3. The signal yields and means are  $7,608 \pm 87$  and  $20.01 \pm 0.03$  MeV/ $c^2$  for  $D^0 \rightarrow K^-\pi^+$ ,  $72,688 \pm 52$  and  $20.11 \pm 0.02$  MeV/ $c^2$  for  $D^0 \rightarrow K^-\pi^+\pi^0$ , and  $5,409 \pm 74$  and  $20.09 \pm 0.01$  MeV/ $c^2$  for  $D^0 \rightarrow K^-\pi^+\pi^-\pi^+$ . The other determined parameters are summarized in table 6.1 and 6.2.

The detection efficiency  $e_{\text{sig}}$  for each  $D^0$  decay mode is estimated by taking the ratio of  $N_{\text{sig}}$  to the numbers of generated events  $N_{\text{gen}}$ . The results are summarized in table 6.2.

### 6.2 Background estimation

Following background sources are considered;  $uds$ ,  $B\bar{B}$ , and  $c\bar{c}$ , and  $D^{*0} \rightarrow D^0e^+e^-$ .

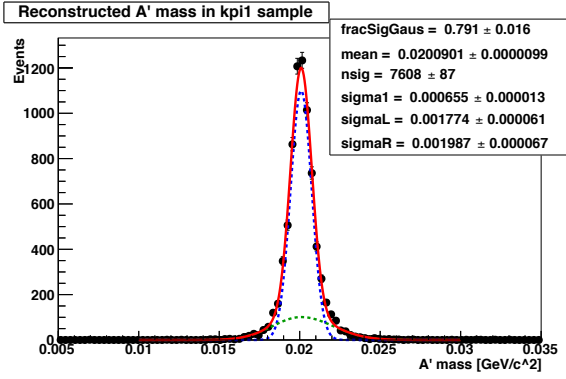


Figure 6.1: Reconstructed  $A'$  mass distribution of signal MC in  $D^0 \rightarrow K^- \pi^+$  mode and the fit result by double Gaussian.

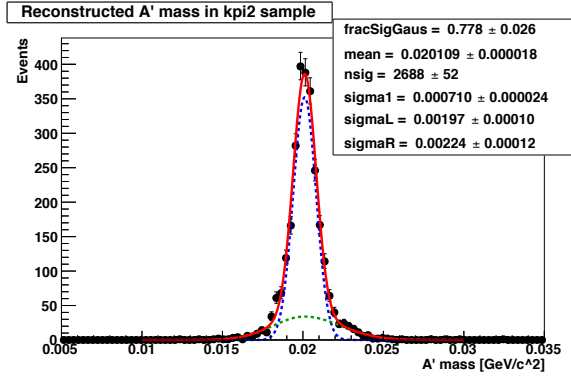


Figure 6.2: Reconstructed  $A'$  mass distribution of signal MC in  $D^0 \rightarrow K^- \pi^+ \pi^0$  mode and the fit result by double Gaussian.

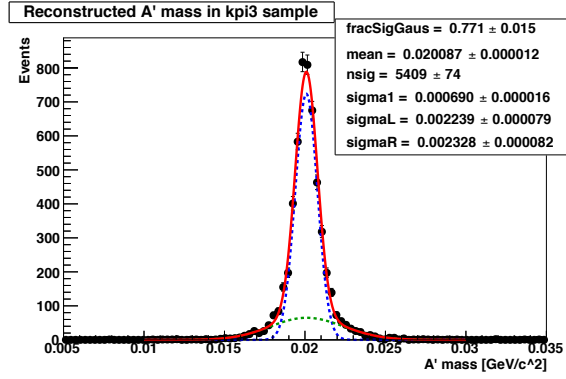


Figure 6.3: Reconstructed  $A'$  mass distribution of signal MC in  $D^0 \rightarrow K^- \pi^+ \pi^- \pi^+$  mode and the fit result by double Gaussian.

Figures 6.4, 6.5, 6.6 show the reconstructed  $A'$  mass for each sub decay modes. The main sources of backgrounds are  $c\bar{c}$  and  $D^{*0} \rightarrow D^0 e^+ e^-$ .

The distributions consist of two components. A structure near  $10 \text{ MeV}/c^2$  is considered to be from  $D^{*0} \rightarrow D^0 \gamma (\rightarrow e^+ e^-)$  process mentioned in Sec. 5.4.3. The  $D^{*0} \rightarrow D^0 e^+ e^-$  background is included in the broad curve and is not treated individually.

The fit range is set from 12 to  $140 \text{ MeV}/c^2$ . The lower limit is determined to avoid contamination from the badly reconstructed tracks in low momentum region. The upper limit is determined by the mass difference between  $D^{*0}$  and  $D^0$ ,  $142 \text{ MeV}/c^2$ . The background is modeled by a sum of a quartic function for the broad structure and an exponential for the structure near  $10 \text{ MeV}/c^2$ .

$$f_{\text{bkg}}(m_{A'}) = C_{\text{bkg}} \left( C_e(a_0) \exp(a_0 m_{A'}) \right) + (1 - C_{\text{bkg}}) \left( C_q(a_i) (1 + a_1 m_{A'} + a_2 m_{A'}^2 + a_3 m_{A'}^3 + a_4 m_{A'}^4) \right), \quad (6.2)$$

where  $C_e(a_0)$  and  $C_q(a_i)$  are normalization factors for the exponential and quartic functions, respectively, and  $C_{\text{bkg}}$  is the fraction of the two functions. Parameters  $a_i$  and  $C_{\text{bkg}}$  are floated in the fit to the data.

Table 6.1: Determined parameters of signal MC for each mode

Mode	$\mu$ [MeV/ $c^2$ ]	$\sigma$ [MeV/ $c^2$ ]	$\sigma_L$ [MeV/ $c^2$ ]	$\sigma_R$ [MeV/ $c^2$ ]	$C_{\text{sig}}$
$D^0 \rightarrow K^- \pi^+$	$20.01 \pm 0.03$	$0.54 \pm 0.04$	$1.30 \pm 0.11$	$1.76 \pm 0.15$	$0.79 \pm 0.02$
$D^0 \rightarrow K^- \pi^+ \pi^0$	$20.11 \pm 0.02$	$0.71 \pm 0.02$	$1.97 \pm 0.10$	$2.24 \pm 0.12$	$0.78 \pm 0.03$
$D^0 \rightarrow K^- \pi^+ \pi^- \pi^+$	$20.09 \pm 0.01$	$0.69 \pm 0.02$	$2.24 \pm 0.08$	$2.24 \pm 0.08$	$0.77 \pm 0.02$

Table 6.2: The signal efficiencies in each mode

Mode	Fitted yield	Generated events	Signal efficiency
$D^0 \rightarrow K^- \pi^+$	$7,608 \pm 87$	244,036	$3.12 \pm 0.04\%$
$D^0 \rightarrow K^- \pi^+ \pi^0$	$2,688 \pm 52$	259,417	$1.04 \pm 0.02\%$
$D^0 \rightarrow K^- \pi^+ \pi^- \pi^+$	$5,409 \pm 74$	262,707	$2.06 \pm 0.03\%$

Figures 6.7 - 6.9 show the result of fit to  $m_{A'}$  distribution for each  $D^0$  decay mode. The functions are appropriate to model the backgrounds.

## 6.3 Extraction of signal yield

Once we obtain the  $m_{A'}$  distributions, the signal is extracted by fitting the distribution to the fitting function  $f(m_{A'})$ ,

$$f(m_{A'}) = N_{\text{sig}} f_{\text{sig}}(m_{A'}) + N_{\text{bkg}} f_{\text{bkg}}(m_{A'}) \quad (6.3)$$

where  $N_{\text{sig}}$  and  $N_{\text{bkg}}$  are the numbers of signal and background events. The parameters in  $f_{\text{sig}}$  are fixed to the values obtained from the signal MC shown in table 6.1, while the parameters in  $f_{\text{bkg}}$  (shown in Eq. 6.2) are floated.

To validate the fit procedure, we fit the background MC distribution with Eq. 6.3 and estimate the signal yield. If the fit does not have a bias, the yield should be consistent with null.

Figures 6.10 - 6.12 show the results of the fit to background MC corresponding to 711  $\text{fb}^{-1}$  assuming  $m_{A'} = 20 \text{ MeV}/c^2$ . We obtain signal yields  $N_{\text{sig}} = 9.5 \pm 7.9$  in  $D^0 \rightarrow K^- \pi^+$ ,  $N_{\text{sig}} = -18.1 \pm 11$  in  $D^0 \rightarrow K^- \pi^+$ , and  $N_{\text{sig}} = -27.6 \pm 15$  in  $D^0 \rightarrow K^- \pi^+ \pi^- \pi^+$  mode.

## 6.4 Fit stability

### 6.4.1 Toy MC

The stability of the yield estimation for different datasets is checked by the Toy Monte Carlo (Toy MC) method. Toy MC is a process to generate multiple datasets, called Toy MC sample, which consist of randomly generated events based on signal and background pdfs. Since the

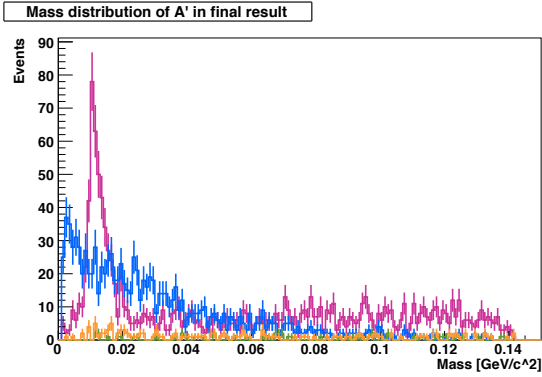


Figure 6.4: Reconstructed  $A'$  mass distribution of background MC in  $D^0 \rightarrow K^- \pi^+$  mode. Orange shows  $uds$ , purple shows  $charm$ , green shows  $B\bar{B}$ , and blue shows the  $D^0 e^+ e^-$  background.

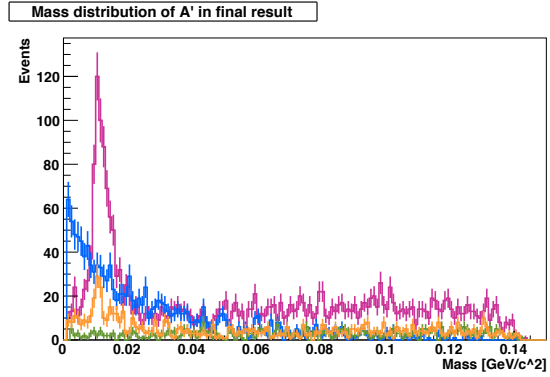


Figure 6.5: Reconstructed  $A'$  mass distribution of background MC in  $D^0 \rightarrow K^- \pi^+ \pi^0$  mode. Orange shows  $uds$ , purple shows  $charm$ , green shows  $B\bar{B}$ , and blue shows the  $D^0 e^+ e^-$  background.

events are generated without the detailed and time-consuming detector simulation, a large number of datasets can be prepared. The fit is performed on many datasets and the variation in the results is checked to study possible bias or instability of the fit.

Toy MC samples are generated using the Monte Carlo method according to the signal and background pdfs shown in Sec. 6.1 and Sec. 6.2. The parameters in pdfs are fixed to the values obtained from the fit to the MC data as described in previous sections. The fit results are shown in Fig. 6.7 - 6.9 and the parameter values are summarized in Table 6.1. The size of each Toy MC sample corresponds to  $711 \text{ fb}^{-1}$  which is the same size of the real data.

### 6.4.2 Validation with Toy MC method

We first generate 3000 Toy MC samples only from the background pdf and fit them to estimate  $N_{\text{sig}}$  for each sample. The resulting distributions of  $N_{\text{sig}}$  and its error for each  $D^0$  decay mode are shown in Fig. 6.13 - 6.18. The distributions of  $N_{\text{sig}}$  and errors are fitted to a Gaussian function. The means of  $N_{\text{sig}}$  are found to be  $-0.4 \pm 7.5$  in  $D^0 \rightarrow K^- \pi^+$ ,  $-0.8 \pm 11.5$  in  $D^0 \rightarrow K^- \pi^+$ , and  $0.1 \pm 15.4$  in  $D^0 \rightarrow K^- \pi^+ \pi^- \pi^+$  mode. They are zero-consistent and the fit procedure is confirmed to work correctly by Toy MC.

### 6.4.3 Check of fit stability

The check with the signal component is performed as the next step. The Toy MC samples are generated with both signal and background pdf included. The number of signal events in the sample is varied and compared with the values of  $N_{\text{sig}}$  obtained by the fit. The number of signal events are set to 0, 5, 10, 15, 20, 25, and 30 in each of Toy MC study, and compared with  $N_{\text{sig}}$  obtained by the fit.

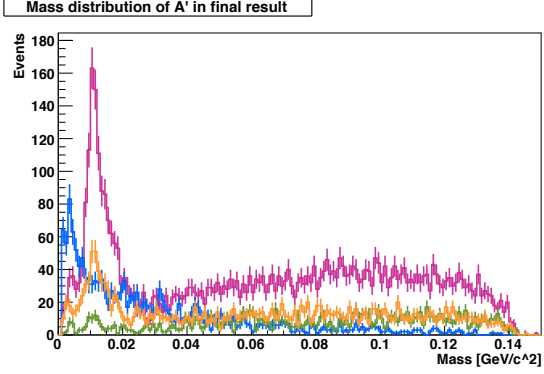


Figure 6.6: Reconstructed  $A'$  mass distribution of background MC in  $D^0 \rightarrow K^- \pi^+ \pi^- \pi^+$  mode. Orange shows  $uds$ , purple shows  $charm$ , green shows  $B\bar{B}$ , and blue shows the  $D^0 e^+ e^-$  background.

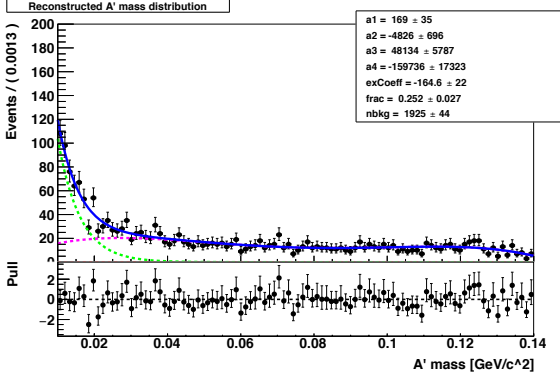


Figure 6.7: Fit result on the background MC in  $D^0 \rightarrow K^- \pi^+$  mode. The green dotted line shows exponential component in Eq. 6.3 and the magenta line shows the polynomial component.

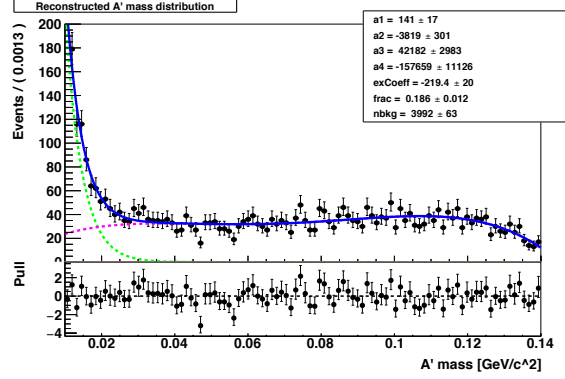


Figure 6.8: Fit result on the background MC in  $D^0 \rightarrow K^- \pi^+ \pi^0$  mode. The green dotted line shows exponential component in Eq. 6.3 and the magenta line shows the polynomial component.

The results are shown in Fig.6.19 - 6.21. As seen, the linearity between the input and output  $N_{\text{sig}}$  is well kept and the fit is confirmed to be stable without any bias.

## 6.5 Yield estimation of $D^{*0} \rightarrow D^0 \gamma$

For the normalization mode, the yield of  $D^{*0} \rightarrow D^0 \gamma$  ( $N_{D^* \gamma}$ ) is obtained from the fit to  $\Delta m = m_{D^{*0}} - m_{D^0}$  distribution. The signal component is modeled by

$$f_{\text{sig}\gamma}(\Delta m) = CB(\Delta m; \mu_\gamma, \sigma_\gamma, \alpha, n), \quad (6.4)$$

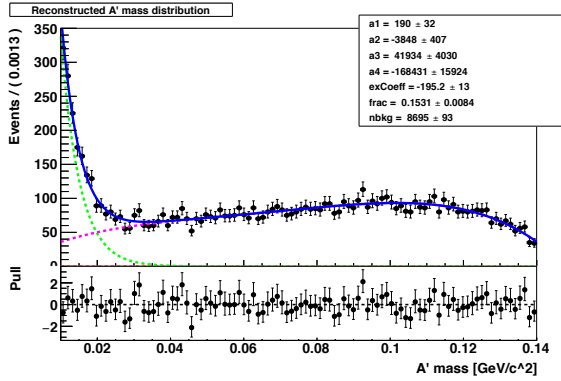


Figure 6.9: Fit result on the background MC in  $D^0 \rightarrow K^- \pi^+ \pi^- \pi^+$  mode. The green dotted line shows exponential component in Eq. 6.3 and the magenta line shows the polynomial component.

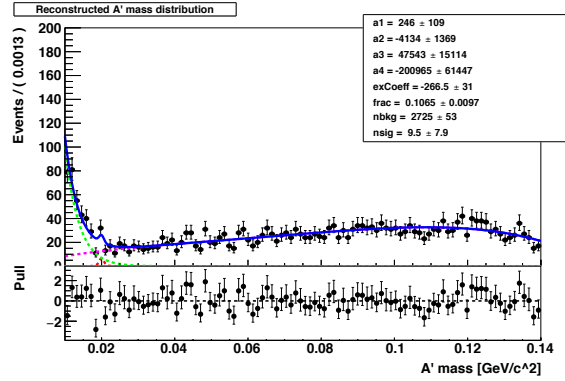


Figure 6.10: Fit result on the background MC to signal and background function in  $D^0 \rightarrow K^- \pi^+$  mode. The red dotted curve shows the signal component, green dotted curve shows exponential component in Eq. 6.3 and the magenta line shows the polynomial component.

where  $CB$  is a Crystal Ball function with mean  $\mu_\gamma$ , width  $\sigma_\gamma$ , and tail factors  $\alpha$  and  $n$  defined by

$$CB(x; \mu_\gamma, \sigma_\gamma, \alpha, n) = N \cdot \begin{cases} \exp\left(-\frac{(x-\mu_\gamma)^2}{2\sigma_\gamma^2}\right) & \text{for } \frac{x-\mu_\gamma}{\sigma_\gamma} > -\alpha \\ A \cdot \left(B - \frac{x-\mu_\gamma}{\sigma_\gamma}\right)^{-n} & \text{for } \frac{x-\mu_\gamma}{\sigma_\gamma} \leq -\alpha \end{cases} \quad (6.5)$$

with

$$A = \left(\frac{n}{|\alpha|}\right)^n \cdot \exp\left(-\frac{|\alpha|^2}{2}\right), \quad (6.6)$$

$$B = \frac{n}{|\alpha|} - |\alpha|. \quad (6.7)$$

where  $N$  is the normalization factor. The background is modeled by a quadratic function as

$$f_{\text{bkg}\gamma}(\Delta m) = C_q(a_i)(1 + a_1 \Delta m + a_2 \Delta m^2), \quad (6.8)$$

where  $a_1$  and  $a_2$  are the parameters of the quadratic function and  $C_q(a_i)$  is the normalization. The fit function is

$$f_{D^*\gamma}(\Delta m) = N_{\text{sig}\gamma} f_{\text{sig}\gamma}(\Delta m) + N_{\text{bkg}\gamma} f_{\text{bkg}\gamma}(\Delta m), \quad (6.9)$$

where  $N_{\text{sig}\gamma}$  and  $N_{\text{bkg}\gamma}$  are the number of  $D^{*0} \rightarrow D^0 \gamma$  and background events. All the parameters in  $f_{\text{sig}\gamma}$  and  $f_{\text{bkg}\gamma}$  are floated in the fit.

The efficiency of  $D^{*0} \rightarrow D^0 \gamma$  is evaluated by the MC simulation as the ratio of  $N_{\text{sig}\gamma}$  and the number of generated  $D^{*0} \rightarrow D^0 \gamma$  events  $N_{\text{gen}}$ ;

$$e_{D^*\gamma} = \frac{N_{\text{sig}\gamma}}{N_{\text{gen}}}. \quad (6.10)$$

A typical fit to  $D^0 \rightarrow K^- \pi^+$  mode is shown in Fig. 6.22. The estimated detection efficiencies are summarized in table 6.3.

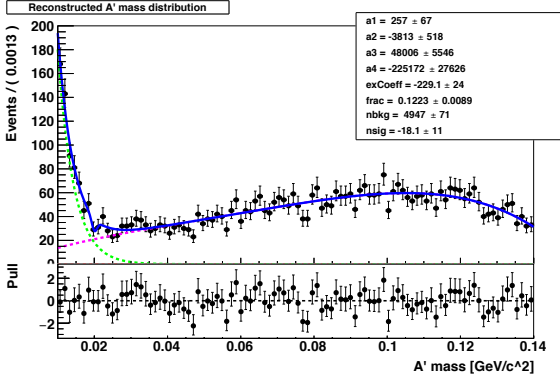


Figure 6.11: Fit result on the background MC to signal and background function in  $D^0 \rightarrow K^-\pi^+\pi^0$  mode. The red dotted curve shows the signal component, green dotted curve shows exponential component in Eq. 6.3 and the magenta line shows the polynomial component.

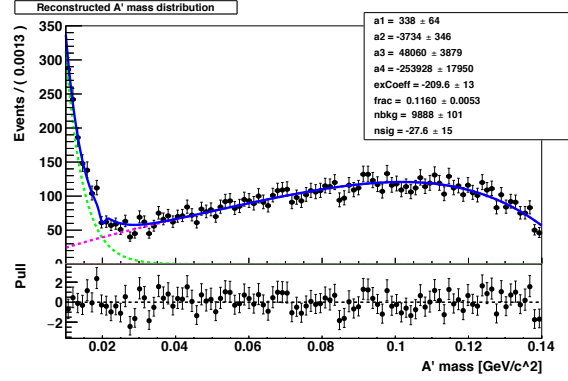


Figure 6.12: Fit result on the background MC to signal and background function in  $D^0 \rightarrow K^-\pi^+\pi^-\pi^+$  mode. The red dotted curve shows the signal component, green dotted curve shows exponential component in Eq. 6.3 and the magenta line shows the polynomial component.

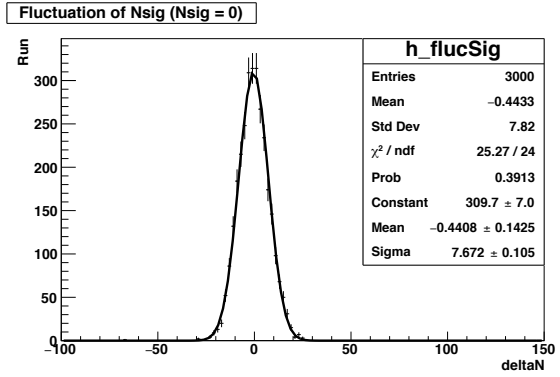


Figure 6.13:  $N_{\text{sig}}$  distribution of  $D^0 \rightarrow K^-\pi^+$  mode in toy MCs.

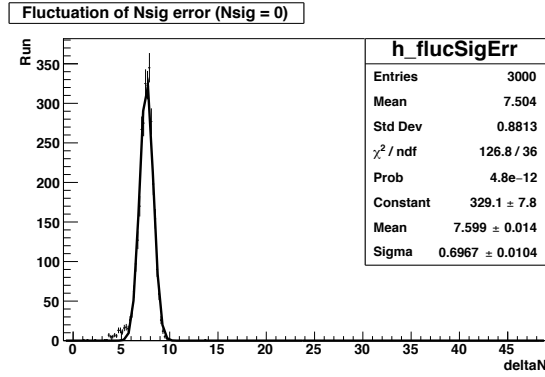


Figure 6.14:  $N_{\text{sig}}$  error distribution of  $D^0 \rightarrow K^-\pi^+$  mode in toy MCs.

## 6.6 Branching fraction calculation by the simultaneous fit in MC

To combine the three  $D^0$  decay modes, we perform a simultaneous fit to the  $m_{A'}$  distributions of the three modes using the ratio of branching fractions  $R = B(D^{*0} \rightarrow D^0 A') / B(D^{*0} \rightarrow D^0 \gamma)$  as a single common parameter. As shown in Eq. 5.4, the signal yield in each  $D^0$  decay mode is written as

$$N_{\text{sig}} = N_{D^{*0}\gamma} \frac{e_{\text{sig}}}{e_{D^{*0}\gamma}} R \quad (6.11)$$

where  $N_{D^{*0}\gamma}$  and  $e_{D^{*0}\gamma}$  are the number of events and efficiency of the normalization mode  $D^{*0} \rightarrow D^0 \gamma$  and  $e_{\text{sig}}$  is the signal efficiency in each mode.  $e_{\text{sig}}$  and  $e_{D^{*0}\gamma}$  are obtained by MC studies in Sec. 6.1 and Sec. 6.5.

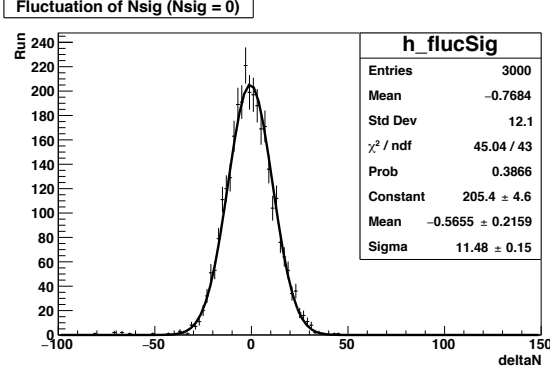


Figure 6.15:  $N_{\text{sig}}$  distribution of  $D^0 \rightarrow K^- \pi^+ \pi^0$  mode in toy MCs.

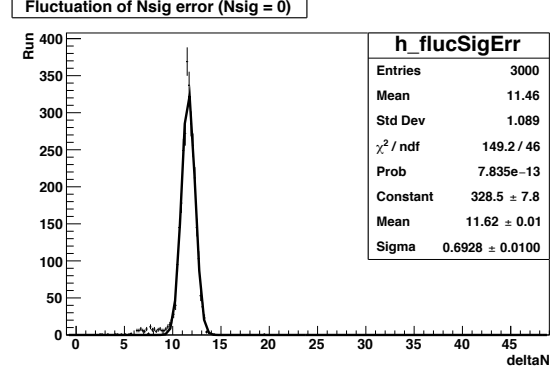


Figure 6.16:  $N_{\text{sig}}$  error distribution of  $D^0 \rightarrow K^- \pi^+ \pi^0$  mode in toy MCs.

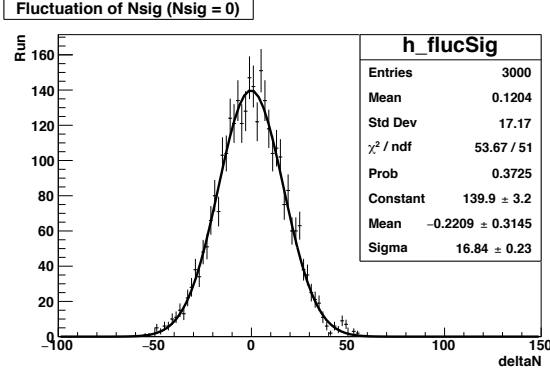


Figure 6.17:  $N_{\text{sig}}$  distribution of  $D^0 \rightarrow K^- \pi^+ \pi^- \pi^+$  mode in toy MCs.

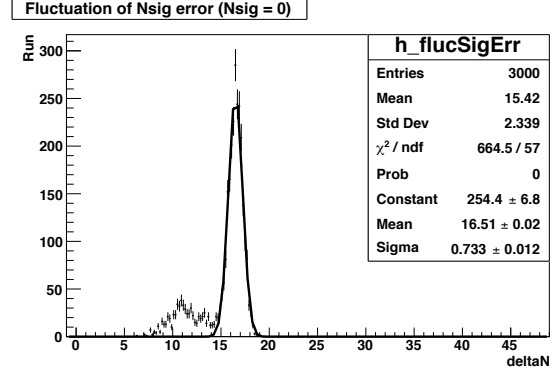


Figure 6.18:  $N_{\text{sig}}$  error distribution of  $D^0 \rightarrow K^- \pi^+ \pi^- \pi^-$  mode in toy MCs.

The likelihood for the simultaneous fit is defined as

$$\begin{aligned}
 \mathcal{L}(R; \{m_{A'}\}, \boldsymbol{\theta}) &= \prod_j \frac{\exp(-(N_{\text{sig}}^j + N_{\text{bkg}}^j))}{n^j!} \prod_i^{n^j} \left( N_{\text{sig}}^j f_{\text{sig}}^j(m_{A'i}) + N_{\text{bkg}}^j f_{\text{bkg}}^j(m_{A'i}, \boldsymbol{\theta}_{\text{bkg}}^j) \right) \\
 &= \prod_j \frac{\exp\left(-\left(N_{D^* \gamma}^j \frac{e_{\text{sig}}^j}{e_{D^* \gamma}^j} R + N_{\text{bkg}}^j\right)\right)}{n^j!} \prod_i^{n^j} \left( N_{D^* \gamma}^j \frac{e_{\text{sig}}^j}{e_{D^* \gamma}^j} R f_{\text{sig}}^j(m_{A'i}) + N_{\text{bkg}}^j f_{\text{bkg}}^j(m_{A'i}, \boldsymbol{\theta}_{\text{bkg}}^j) \right).
 \end{aligned} \tag{6.12}$$

In the left term,  $\{m_{A'}\}$  represents the results of  $m_{A'}$  in all reconstructed events,  $\boldsymbol{\theta}$  represents all the parameters of fit function for three  $D^0$  decay modes. In the right term,  $j$  denotes each sub decay mode of  $D^0$ ,  $m_{A'i}$  is the mass of  $A'$  derived from the  $i$ -th event out of a total of  $n^j$  events in each mode, and  $\boldsymbol{\theta}_{\text{bkg}}$  are floating parameters of  $f_{\text{bkg}}^j$  shown in Eq. 6.2.

As an example, we perform a simultaneous fit to background MC sample assuming  $m_{A'} = 20 \text{ MeV}/c^2$ . The result is shown in Fig. 6.23 - 6.25 and we obtain

$$R = (-1.1 \pm 4.7) \times 10^{-5}. \tag{6.13}$$

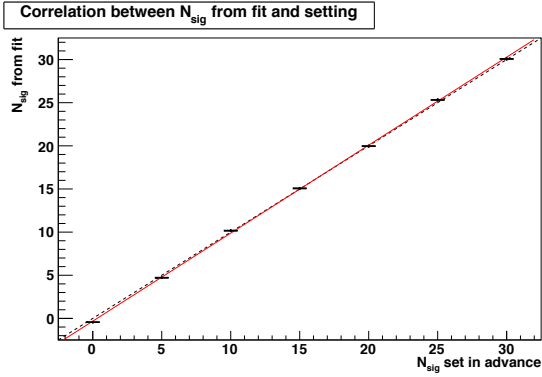


Figure 6.19:  $N_{\text{sig}}$  correlation in  $D^0 \rightarrow K^- \pi^+$  mode. Red line shows fit result by linear function and black dashed line is  $x = y$  reference.

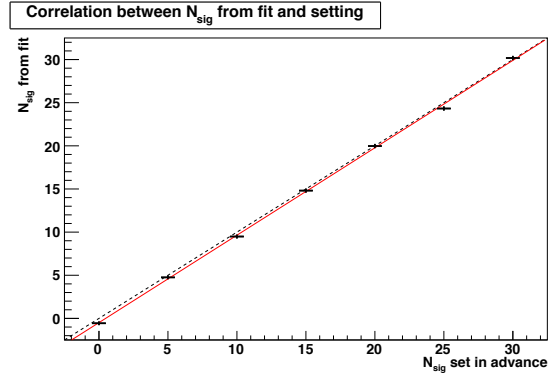


Figure 6.20:  $N_{\text{sig}}$  correlation in  $D^0 \rightarrow K^- \pi^+ \pi^0$  mode. Red line shows fit result by linear function and black dashed line is  $x = y$  reference.

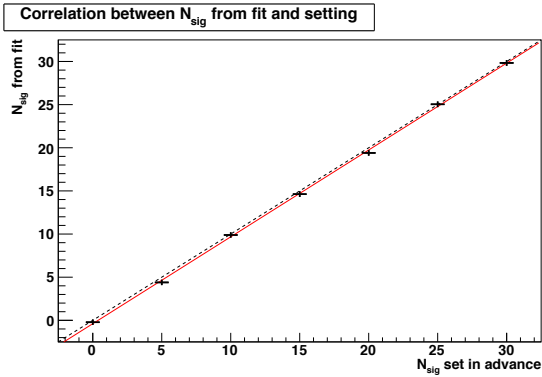


Figure 6.21:  $N_{\text{sig}}$  correlation in  $D^0 \rightarrow K^- \pi^+ \pi^- \pi^+$  mode. Red line shows fit result by linear function and black dashed line is  $x = y$  reference.

We also perform a Toy MC study of the signal fit with null signal. 3000 toy experiment sets are prepared and are fitted.

The distribution of the ratio of branching fractions and its error are shown in Fig. 6.26 and Fig. 6.27. From the mean and width of the distribution, we obtain

$$R = (-0.1 \pm 2.9) \times 10^{-5}. \quad (6.14)$$

The result is consistent with null.

## 6.7 $A'$ mass dependence of parameters

The mass of the dark photon is unknown, and we need to repeat the same procedure for different  $A'$  masses and scan over  $m_{A'}$ . For this purpose, additional signal MCs are prepared with different  $A'$  mass from 30 to 120 MeV/ $c^2$  in every 10 MeV/ $c^2$  step. The  $m_{A'}$  dependence

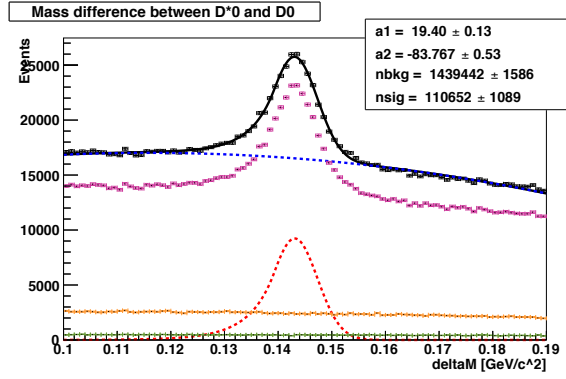


Figure 6.22:  $\Delta m$  distribution of  $D^{*0} \rightarrow D^0(\rightarrow K\pi)\gamma$  in a part of MC simulation ( $60 \text{ fb}^{-1}$ ). Orange shows  $uds$ , purple shows  $charm$ , green shows  $B\bar{B}$ . The fit results are shown by the lines. Red dotted line shows CB component, blue dotted line shows the background component, and black solid line shows the sum of them.

Table 6.3: The summary of efficiencies of  $D^{*0} \rightarrow D^0\gamma$  in whole MC ( $711 \text{ fb}^{-1}$ )

$D^0$ decay mode	$D^0 \rightarrow K^-\pi^+$	$D^0 \rightarrow K^-\pi^+\pi^0$	$D^0 \rightarrow K^-\pi^+\pi^-\pi^+$
$N_{\text{gen}}$	$6.7 \times 10^6$	$22.9 \times 10^6$	$12.6 \times 10^6$
$N_{\text{det}}$	$1.33 \times 10^6$	$1.71 \times 10^6$	$1.73 \times 10^6$
Efficiency [%]	$20.01 \pm 0.02$	$7.51 \pm 0.01$	$13.7 \pm 0.01$

of the signal efficiencies and the parameters in the signal PDFs are checked. Figures 6.28 - 6.32 show the obtained parameters in each decay mode. Table 6.4 shows the obtained dependences on  $m_{A'}$ . The fit results are shown in Fig. 6.28 - 6.32.

We model the dependence with a linear function. From the fit, we obtain the dependences on  $m_{A'}$  as shown in table 6.4.

Table 6.4: The dependence of signal function parameters on  $m_{A'}$

Mode	Efficiency	$\sigma$ [ $\text{MeV}/c^2$ ]	$\sigma_L$ [ $\text{MeV}/c^2$ ]	$\sigma_R$ [ $\text{MeV}/c^2$ ]	$C_{\text{sig}}$
$D^0 \rightarrow K^-\pi^+$	$0.032 + 0.035m_{A'}$	$(0.71 + 0.89m_{A'}) \times 10^{-3}$	$(2.00 + 4.05m_{A'}) \times 10^{-3}$	$(2.22 + 7.76m_{A'}) \times 10^{-3}$	$0.83 - 1.20m_{A'}$
$D^0 \rightarrow K^-\pi^+\pi^0$	$0.011 + 0.006m_{A'}$	$(0.70 + 2.05m_{A'}) \times 10^{-3}$	$(2.06 + 8.10m_{A'}) \times 10^{-3}$	$(2.23 + 12.00m_{A'}) \times 10^{-3}$	$0.75 - 0.23m_{A'}$
$D^0 \rightarrow K^-\pi^+\pi^-\pi^+$	$0.021 + 0.024m_{A'}$	$(0.72 + 1.32m_{A'}) \times 10^{-3}$	$(2.37 + 5.01m_{A'}) \times 10^{-3}$	$(2.26 + 12.89m_{A'}) \times 10^{-3}$	$0.78 - 0.75m_{A'}$

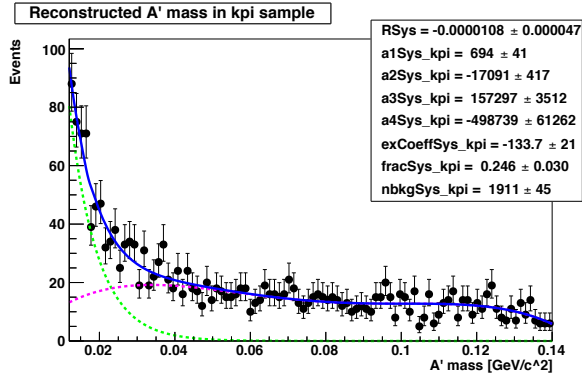


Figure 6.23: The result of simultaneous fit in  $D^0 \rightarrow K^- \pi^+$  mode. The Red dotted shows the signal yield. And the green dotted line shows exp component in Eq. 6.3 and the magenta line shows the  $pol4$ .

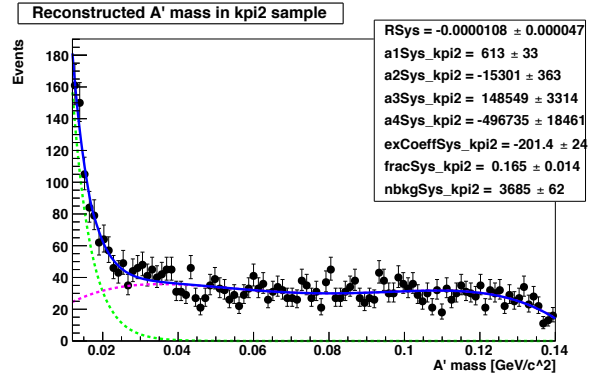


Figure 6.24: The result of simultaneous fit in  $D^0 \rightarrow K^- \pi^+ \pi^0$  mode. The Red dotted shows the signal yield. And the green dotted line shows exp component in Eq. 6.3 and the magenta line shows the  $pol4$ .

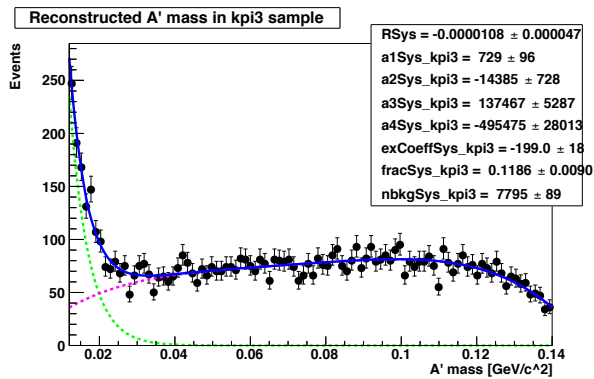


Figure 6.25: The result of simultaneous fit in  $D^0 \rightarrow K^- \pi^+ \pi^- \pi^+$  mode. The Red dotted shows the signal yield. And the green dotted line shows exp component in Eq. 6.3 and the magenta line shows the  $pol4$ .

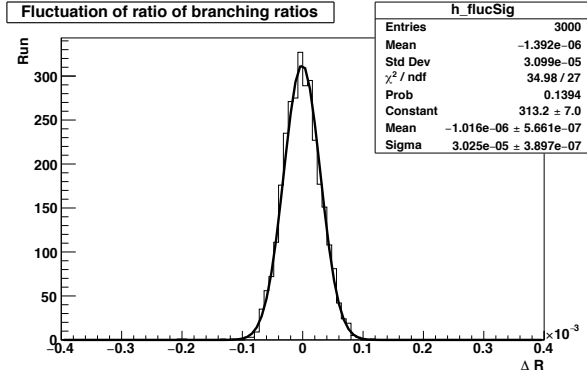


Figure 6.26: The distribution of the ratio of branching fractions in 3000 toy experiments.

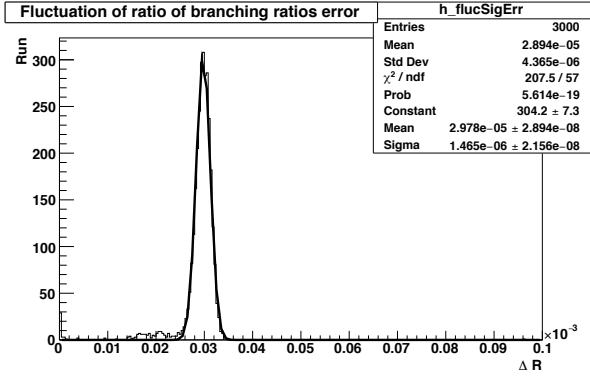


Figure 6.27: The distribution of the ratio of branching fractions error in 3000 toy experiments.

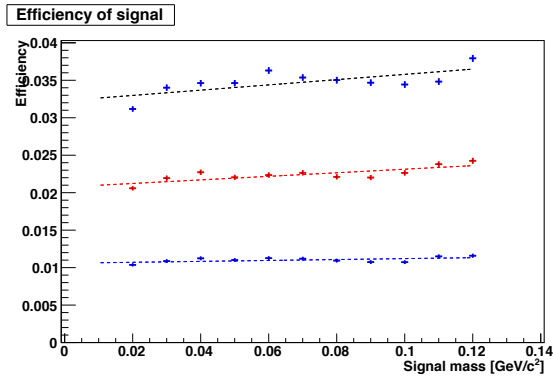


Figure 6.28: The efficiency versus  $A'$  mass. Black shows  $D^0 \rightarrow K^- \pi^+$  mode, blue shows  $D^0 \rightarrow K^- \pi^+ \pi^0$  mode, and red shows  $D^0 \rightarrow K^- \pi^+ \pi^- \pi^+$  mode. The each dotted line shows the fit result of linear function.

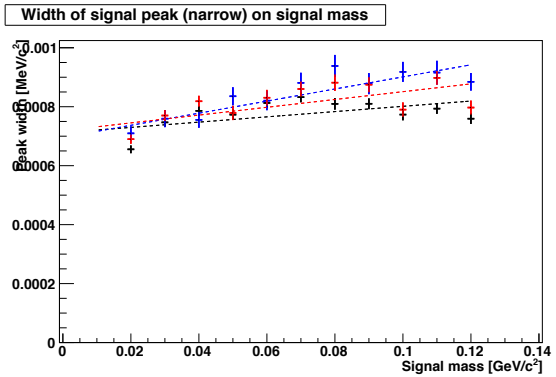


Figure 6.29: The width ( $\sigma$ ) versus  $A'$  mass. Black shows  $D^0 \rightarrow K^- \pi^+$  mode, blue shows  $D^0 \rightarrow K^- \pi^+ \pi^0$  mode, and red shows  $D^0 \rightarrow K^- \pi^+ \pi^- \pi^+$  mode. The each dotted line shows the fit result of linear function.

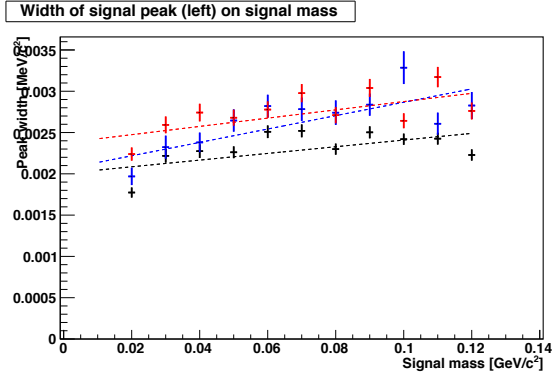


Figure 6.30: The left width ( $\sigma_L$ ) versus  $A'$  mass. Black shows  $D^0 \rightarrow K^-\pi^+$  mode, blue shows  $D^0 \rightarrow K^-\pi^+\pi^0$  mode, and red shows  $D^0 \rightarrow K^-\pi^+\pi^-\pi^+$  mode. The each dotted line shows the fit result of linear function.

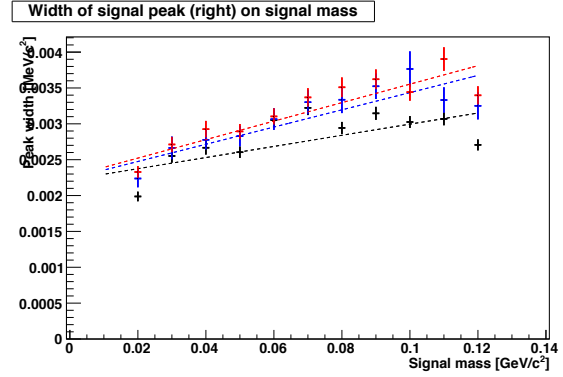


Figure 6.31: The right width ( $\sigma_R$ ) versus  $A'$  mass. Black shows  $D^0 \rightarrow K^-\pi^+$  mode, blue shows  $D^0 \rightarrow K^-\pi^+\pi^0$  mode, and red shows  $D^0 \rightarrow K^-\pi^+\pi^-\pi^+$  mode. The each dotted line shows the fit result of linear function.

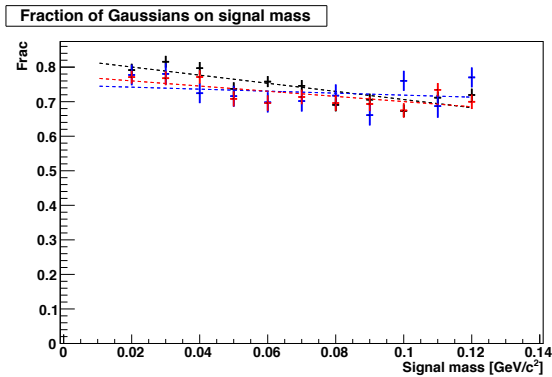


Figure 6.32: The fraction of Gaussians versus  $A'$  mass. Black shows  $D^0 \rightarrow K^-\pi^+$  mode, blue shows  $D^0 \rightarrow K^-\pi^+\pi^0$  mode, and red shows  $D^0 \rightarrow K^-\pi^+\pi^-\pi^+$  mode. The each dotted line shows the fit result of linear function.

# Chapter 7

## Systematic Uncertainty

There are two kinds of systematic uncertainties. One is related to the detection efficiency, and is discussed in this chapter. The other systematic uncertainty comes from the fit and is discussed in Chap. 8.

### 7.1 Breakdown of the systematics

As already discussed, the  $R$  ratio depends on the detection efficiencies for the signal and normalization modes as shown in Eq. 7.1.

$$R = \frac{B(D^{*0} \rightarrow D^0 A')}{B(D^{*0} \rightarrow D^0 \gamma)} = \frac{N_{\text{sig}} e_{D^{*}\gamma}}{N_{D^{*}\gamma} e_{\text{sig}}}. \quad (7.1)$$

The efficiencies obtained by MC need additional calibration using data:

$$e_{\text{sig}} = e_{\text{sig}}^{\text{MC}} \eta_{D^0} \eta_{e^\pm} \eta_{\text{vtx}} \eta_{\chi^2} \quad (7.2)$$

$$e_{D^{*}\gamma} = e_{D^{*}\gamma}^{\text{MC}} \eta_{D^0} \eta_{\gamma} \quad (7.3)$$

where  $e_{\text{sig}}^{\text{MC}}$  and  $e_{D^{*}\gamma}^{\text{MC}}$  are the efficiencies of signal and normalization modes obtained by MC and  $\eta_{D^0}$ ,  $\eta_{e^\pm}$ ,  $\eta_{\gamma}$ ,  $\eta_{\text{vtx}}$ , and  $\eta_{\chi^2}$  are the correction factors obtained by data for the reconstruction of  $D^0$ , efficiencies of  $e^\pm$  and  $\gamma$ , and  $e^+e^-$  vertex and  $\chi^2$  selections, respectively.

With the correction factors,  $R$  can be expressed as

$$R = \frac{N_{\text{sig}}}{N_{D^{*}\gamma}} \frac{e_{D^{*}\gamma}^{\text{MC}}}{e_{\text{sig}}^{\text{MC}}} \frac{\eta_{\gamma}}{\eta_{e^\pm} \eta_{\text{vtx}} \eta_{\chi^2}}. \quad (7.4)$$

The uncertainty in the  $D^0$  reconstruction is cancelled. Remaining systematic uncertainties are estimated in following sections.

## 7.2 The efficiencies of $e^+e^-$

The systematic uncertainty in electron reconstruction comes from that in the tracking and lepton ID. The Belle standard values are used for them.

The uncertainty in tracking is estimated by the study using  $B^0 \rightarrow D^{*-}\pi^+$  [76]. The uncertainty is obtained in each region of different momentum and polar angle range. The uncertainty for signal mode is calculated by taking a weighted average over momentum and polar angle. The uncertainty is 2.3% [76] per track.

The uncertainty in lepton ID is also measured using the two photon process  $\gamma\gamma \rightarrow e^+e^-$  [77]. The lepton ID uncertainty also depends on the momentum and polar angle of track. It is estimated by taking a weighted average over the momentum and polar angle. The systematic uncertainty in lepton ID is 2.3% [77] per track.

## 7.3 $\gamma$ finding efficiency

For the uncertainty in efficiency of  $\gamma$  finding ( $\eta_\gamma$ ), the Belle standard value is used. The systematics is estimated using radiative Bhabha sample [78]. The uncertainty is 2% per single photon.

## 7.4 $e^+e^-$ vertex selection efficiency

The systematic uncertainty in the  $e^+e^-$  vertex selection is estimated using the control sample  $\psi(2S) \rightarrow J/\psi(\rightarrow \mu^+\mu^-/e^+e^-)\pi^+\pi^-$ . Data and MC samples corresponding to  $86 \text{ fb}^{-1}$  are used for this study.

In the reconstruction of  $\psi(2S) \rightarrow J/\psi\pi^+\pi^-$ ,  $dr < 1 \text{ cm}$ ,  $|dz| < 5 \text{ cm}$ , and PID selections  $R(L_i) > 0.6$  ( $i = \mu, e, \pi$ ) are applied. Figure 7.1 shows the reconstructed  $J/\psi$  mass. We require  $J/\psi$  mass to be in the range of  $3.085 < m_{J/\psi} < 3.115 \text{ GeV}/c^2$ .

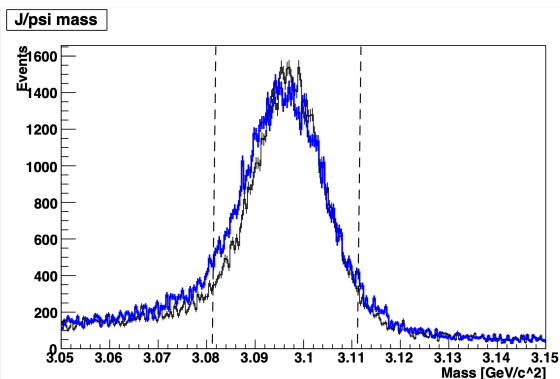


Figure 7.1: Reconstructed  $J/\psi$  mass distribution of data (blue line) and MC (black line).

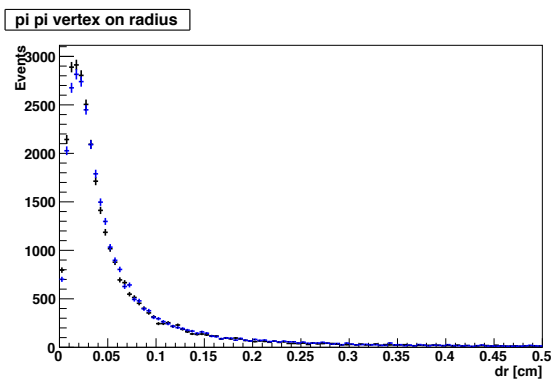


Figure 7.2: The distribution of  $\pi^+\pi^-$  vertex on  $dr$ . The blue line shows the data and the black line shows the MC.

Figure 7.2 shows the vertex of  $\pi^+\pi^-$  of the control mode calculated in the same way as  $e^+e^-$  vertex of the signal mode. The distribution of  $\pi^+\pi^-$  vertex of the control mode, similarly to the signal, has a finite value peak close to 0 and an exponentially decreasing tail.

Figure 7.3 shows the distribution of  $\Delta m = m_{\psi(2S)} - m_{J/\psi}$ . We estimate the number of  $\psi(2S) \rightarrow J/\psi\pi^+\pi^-$  events by a fit to the  $\Delta m$  distribution. The fit is performed to a function

$$f_{\psi}(\Delta m) = N_{\psi}G(\Delta m) + N_{\text{bkg}}C(1 + a\Delta m) \quad (7.5)$$

where  $N_{\psi}$  is the number of  $\psi(2S)$  events,  $G$  is a Gaussian function,  $N_{\text{bkg}}$  is the number of background events,  $a$  is a coefficient for linear function, and  $C$  is the normalization. The fit is done for each  $\Delta m$  distribution with (the red line in Fig. 7.3) and without (the black line in Fig. 7.3) the vertex selection. The efficiency of the vertex selection for the control mode is estimated by the ratio of yields with and without the vertex selection.

For the signal mode, the criteria of the  $e^+e^-$  vertex selection and their efficiencies estimated by MC are  $dr < 0.44$  cm ( $88.03 \pm 0.99\%$ ) for  $D^0 \rightarrow K^-\pi^+$ ,  $dr < 0.66$  cm ( $93.27 \pm 1.25\%$ ) for  $D^0 \rightarrow K^-\pi^+\pi^0$ , and  $dr < 0.64$  cm ( $92.35 \pm 1.02\%$ ) for  $D^0 \rightarrow K^-\pi^+\pi^-\pi^+$ . For the control mode, the criteria are set to be  $dr < 0.092$  cm,  $dr < 0.139$  cm, and  $dr < 0.124$  cm, so that the efficiency of the vertex selection for the control mode is close to that for the signal mode as shown in the fifth column of table 7.1.

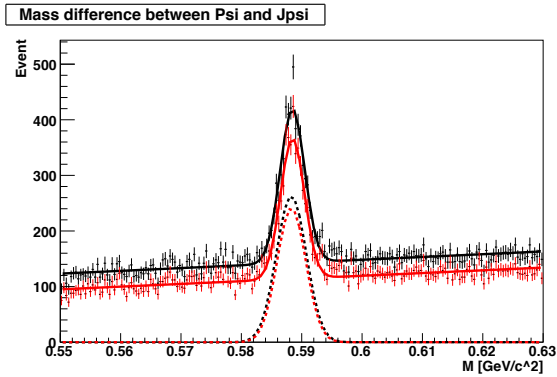


Figure 7.3: An example of  $\Delta m$  distribution before (the black line) and after (the red line) the  $\pi\pi$  vertex selection at  $dr < 0.1$  in MC. Each dotted line shows the peak component.

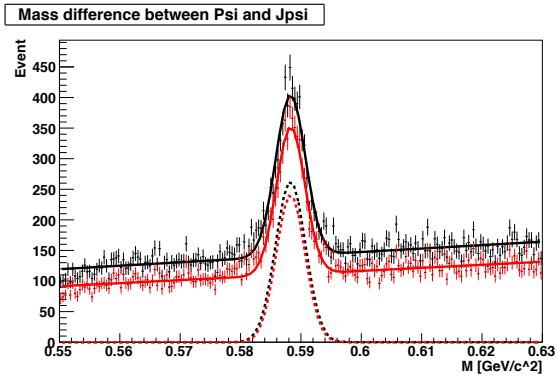


Figure 7.4: An example of  $\Delta m$  distribution before (the black line) and after (the red line) the  $\pi\pi$  vertex selection at  $dr < 0.1$  in data. Each dotted line shows the peak component.

The  $\Delta m$  distributions for the data with and without the selection are shown in Fig. 7.4. Table 7.1 shows the efficiencies of the vertex selection for data and MC. We take the largest difference of the efficiencies in data and MC, 2.6 % as a systematic error for  $\eta_{\text{vtx}}$ .

## 7.5 $\chi^2$ probability selection efficiency

The systematic uncertainty in the selection of  $\chi^2$  probability of the  $D^{*0}$  vertex fit is evaluated using the control mode  $D^{*+} \rightarrow D^0\pi^+$ . The study is done using  $86 \text{ fb}^{-1}$  of data and MC.

Table 7.1: Summary of efficiencies in vertex selections,  $\Delta e$  is the difference of efficiencies.

Mode	Cut value for signal mode [cm]	Efficiency of signal mode $e^+e^-$ vertex in MC [%]	Cut value for control mode [cm]	Efficiency of control mode $\pi^+\pi^-$ vertex in MC [%]	Efficiency of control mode $\pi^+\pi^-$ vertex in data [%]	$\Delta e$ [%]
$K^-\pi^+$	0.44	$88.03 \pm 0.99$	0.092	$88.15 \pm 0.54$	$86.32 \pm 0.54$	$-1.83 \pm 0.76$
$K^-\pi^+\pi^0$	0.64	$93.27 \pm 1.25$	0.139	$93.30 \pm 0.42$	$93.05 \pm 0.43$	$-0.25 \pm 0.60$
$K^-\pi^+\pi^-\pi^+$	0.66	$92.35 \pm 1.02$	0.124	$92.39 \pm 0.44$	$90.97 \pm 0.45$	$-1.42 \pm 0.63$

The final state of the control mode  $D^{*+} \rightarrow D^0\pi^+$  is similar to that of the signal mode except that it has one less charged tracks. The vertex fit is performed in two steps; the vertex fit of  $D^0$  is performed first, then the fit of  $D^{*+}$  is performed using the parameters obtained by the  $D^0$  vertex fit and the other daughter particle(s). The first step is the same both in the signal and the control modes. The second step is also similar though the number of daughter particles is different.

For the control mode, the track selections and  $D^0$  reconstruction are the same as the signal mode (Sec. 5.3.1 and Sec. 5.3.2). Figures 7.5 - 7.7 show the reconstructed mass distributions of  $D^0$  with the same mass selection criteria used for the signal mode in Sec. 5.3.2. The slow pion from the  $D^{*0}$  decay is selected using the same criteria as that for the pion in the  $D^0$  decay.

$D^{*0}$  is reconstructed from the  $D^0$  and  $\pi^+$  tracks with the momentum  $p_{D^{*0}} > 2.5$  GeV. After the  $D^{*0}$  reconstruction,  $\chi_{D^{*+}}^2$  is calculated as described in Sec. 5.4.4.

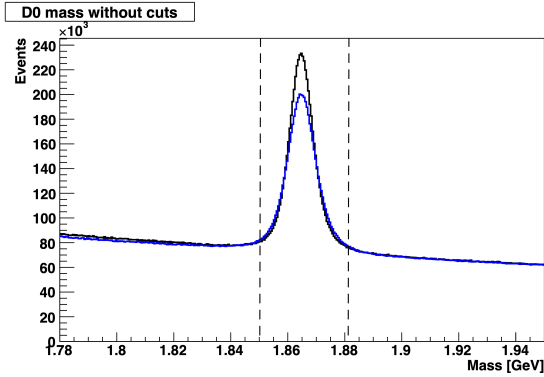


Figure 7.5: The distribution of  $D^0$  mass in  $D^{*+} \rightarrow D^0(\rightarrow K^-\pi^+)\pi^+$  mode. The blue line shows the data and the black line shows the background generated by MC.

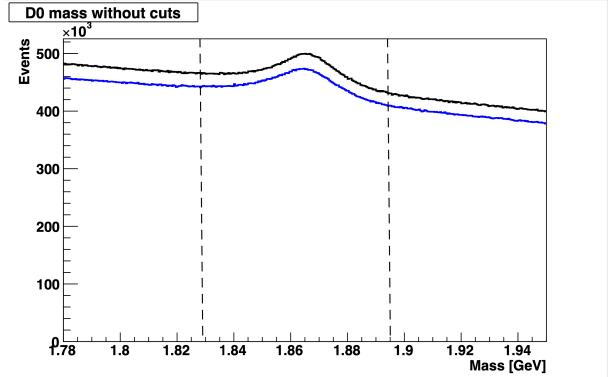


Figure 7.6: The distribution of  $D^0$  mass in  $D^{*+} \rightarrow D^0(\rightarrow K^-\pi^+\pi^0)\pi^+$  mode. The blue line shows the data and the black line shows the background generated by MC.

Figure 7.8 shows the  $\Delta m = m_{D^{*+}} - m_{D^0}$  distribution of  $D^0 \rightarrow K^-\pi^+$  mode as an example. We estimate the signal yields from the fit to the  $\Delta m$  distributions with and without  $\chi_{D^{*+}}^2$  selection. The  $\Delta m$  distribution is modeled by a sum of two Gaussians and a linear function;

$$f_\chi = N_\chi(C_\chi G_1(\Delta m) + (1 - C_\chi)G_2(\Delta m)) + N_{\text{bkg}}C(1 + a\Delta m) \quad (7.6)$$

where  $N_\chi$  is the number of  $D^{*+} \rightarrow D^0\pi^+$  and  $G_1$  and  $G_2$  are normalized Gaussian functions,

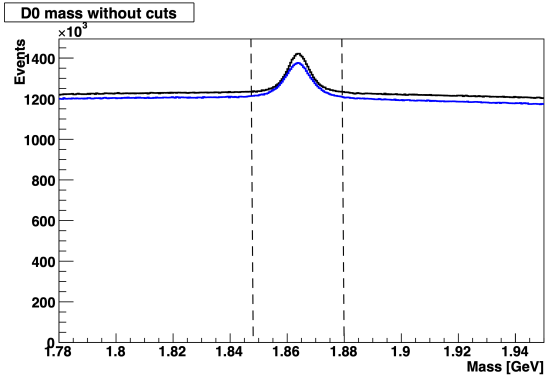


Figure 7.7: The distribution of  $D^0$  mass in  $D^{*+} \rightarrow D^0(\rightarrow K^-\pi^+\pi^-\pi^+)\pi^+$  mode. The blue line shows the data and the black line shows the background generated by MC.

$C_\chi$  is the fraction of the two Gaussian functions,  $N_{\text{bkg}}$  is the number of the background events,  $a$  is a coefficient of linear function and  $C$  is the normalization. The fit is done for each  $\Delta m$  distribution with (the red line in Fig. 7.8) and without (the black line in Fig. 7.8) the  $\chi^2_{D^{*+}}$  selection. The efficiency of the control mode is estimated by the ratio of yields with and without the  $\chi^2_{D^{*+}}$  selection. The  $\chi^2$  criteria of the vertex fit in the control mode is set so that the efficiency becomes the same as that of the signal mode in MC. For the signal mode,  $\chi^2_{D^{*+}}$  is required to be larger than 0.001 for all  $D^0$  decay modes. For the control mode,  $\chi^2_{D^{*+}}$  is required to be  $> 0.0178$  for  $D^0 \rightarrow K^-\pi^+$ ,  $> 0.0182$  for  $D^0 \rightarrow K^-\pi^+\pi^0$ , and  $> 0.0196$  for  $D^0 \rightarrow K^-\pi^+\pi^-\pi^+$ .

Figure 7.8 shows  $\Delta m$  distribution of  $D^{*0} \rightarrow D^0\pi^+$  for data with and without the  $\chi^2_{D^{*+}}$  selection. We take the largest difference of the efficiencies in data and MC, 4.6 % as a systematic error for  $\eta_{\chi^2}$ .

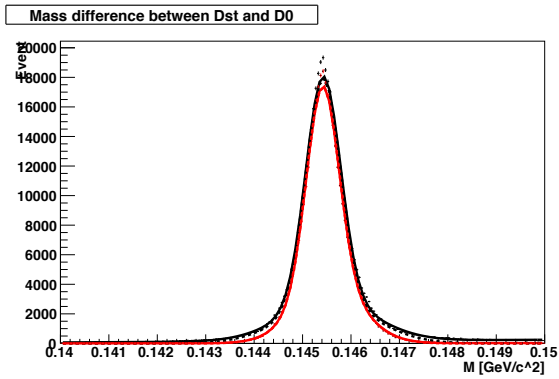


Figure 7.8:  $\Delta m$  distribution of  $D^0 \rightarrow K^-\pi^+$  before (the black line) and after (the red line) the chi probability selection at  $\chi^2 > 0.01$  in MC. Each dotted line shows the peak component.

Table 7.2: Summary of efficiencies in  $\chi^2$  selections,  $\Delta e$  is the difference of efficiencies.

Mode	Efficiency in the signal mode $D^{*0} \rightarrow D^0 A'$ MC [%]	The threshold for the control mode $D^{*+} \rightarrow D^0 \pi^+$	Efficiency in the control mode $D^{*+} \rightarrow D^0 \pi^+$ MC [%]	Efficiency in the control mode $D^{*+} \rightarrow D^0 \pi^+$ data [%]	$\Delta e$ [%]
$K^- \pi^+$	$88 \pm 1$	0.0178	$88.0 \pm 0.1$	$85.1 \pm 0.1$	$-2.8 \pm 0.1$
$K^- \pi^+ \pi^0$	$85 \pm 2$	0.0182	$85.0 \pm 0.1$	$80.9 \pm 0.1$	$-4.1 \pm 0.1$
$K^- \pi^+ \pi^- \pi^+$	$83 \pm 1$	0.0196	$83.0 \pm 0.1$	$78.5 \pm 0.1$	$-4.5 \pm 0.1$

## 7.6 Summary of proportional systematics

Table 7.3 shows the summary of the systematic uncertainties. All systematic uncertainties except for  $\gamma$  finding are the uncertainty in the signal efficiency. The uncertainty in the  $\gamma$  finding comes from the normalization mode. The total systematics uncertainty related to the efficiency is 7.3%.

Table 7.3: Summary of systematic uncertainties

Source	$K\pi$ mode	$K\pi\pi$ mode	$K\pi\pi\pi$ mode	Maximum
Electron ID	3.3%	3.2%	3.3%	3.3%
Tracking	3.3%	3.3%	3.3%	3.3%
$\gamma$ finding	2.0%	2.0%	2.0%	2.0 %
$e^+e^-$ vertex selection	2.6%	0.9%	2.0%	2.6%
$\chi^2$ selection	2.9%	4.2%	4.6%	4.6%
Total for each mode	6.3%	6.7%	6.8%	7.3%

# Chapter 8

## Data Analysis

In this chapter, the experimental data accumulated by Belle spectrometer are analyzed.

The reconstruction of  $D^0$  that is common among the signal and normalization modes is shown in Sec. 8.1. The result of the normalization mode is shown in Sec. 8.2. The measurement of the ratio  $R$  in the signal is given in Sec.8.3. The upper limit of  $R$  is obtained in Sec. 8.4.

### 8.1 Reconstruction of $D^0$ in data

The whole Belle data of  $711 \text{ fb}^{-1}$  are analyzed in the same procedure as that described in Chap. 5.

Figure 8.1 shows the distribution of reconstructed  $m_{\pi^0}$  in  $D^0 \rightarrow K^- \pi^+ \pi^0$  mode. It shows a clear peak at 135 MeV. Figures 8.2 - 8.4 are the distributions of  $m_{D^0}$  for each  $D^0$  sub decay

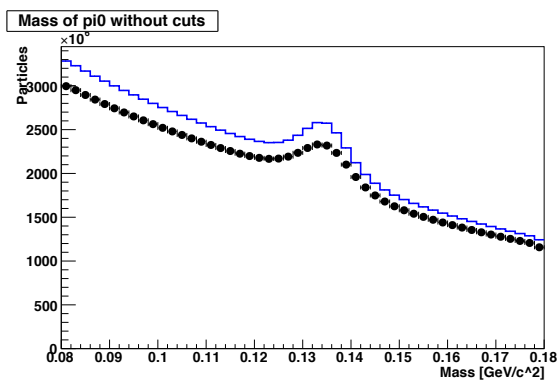


Figure 8.1: The  $m_{\pi^0}$  distribution of experimental data and MC in  $D^0 \rightarrow K^- \pi^+ \pi^0$  mode. Black dots show the data and blue histogram shows the MC.

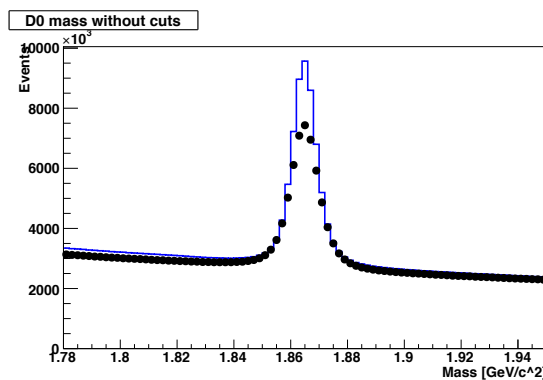


Figure 8.2: The  $m_{D^0}$  distribution of experimental data and MC in  $D^0 \rightarrow K^- \pi^+$  mode. Black dots show the data and blue histogram shows the MC.

mode. They also show clear peaks at  $1.86 \text{ GeV}/c^2$ . There is a discrepancy between the data and MC in the height of the peak. Similar discrepancy is observed in other Belle analyses

[79]–[81], and it is considered to be due to the limitation in the Belle MC simulation. Since the effect is common both in the signal and normalization mode, it does not affect on the ratio  $R$ .

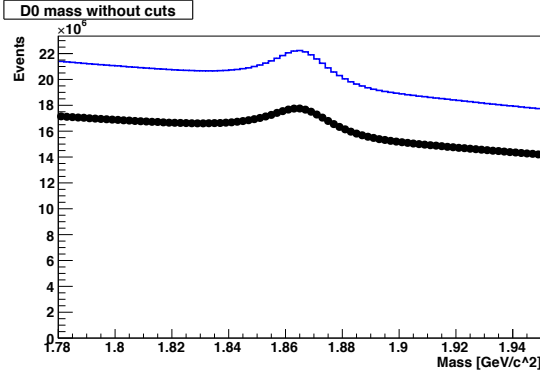


Figure 8.3: The  $m_{D^0}$  distribution of experimental data and MC in  $D^0 \rightarrow K^- \pi^+ \pi^0$  mode. Black dots show the data and blue histogram shows the MC.

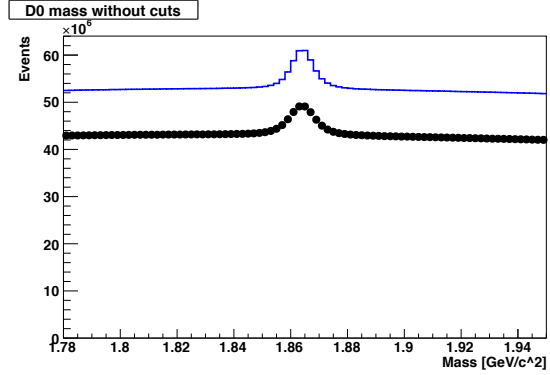


Figure 8.4: The  $m_{D^0}$  distribution of experimental data and MC in  $D^0 \rightarrow K^- \pi^+ \pi^- \pi^+$  mode. Black dots show the data and blue histogram shows the MC.

## 8.2 The yield of the normalization mode in data

Figure 8.5 shows the  $\Delta m$  distributions for the normalization mode. The distributions are fitted to the functions defined in Eq. 6.9, where all parameters are left floated. From the fits, the yields are obtained to be  $(11.5 \pm 0.2) \times 10^5$  in the  $K^+ \pi^-$  mode,  $(16.7 \pm 0.3) \times 10^5$  in the  $K^- \pi^+ \pi^0$  mode, and  $(16.2 \pm 0.6) \times 10^5$  in the  $K^- \pi^+ \pi^- \pi^+$  mode, respectively.

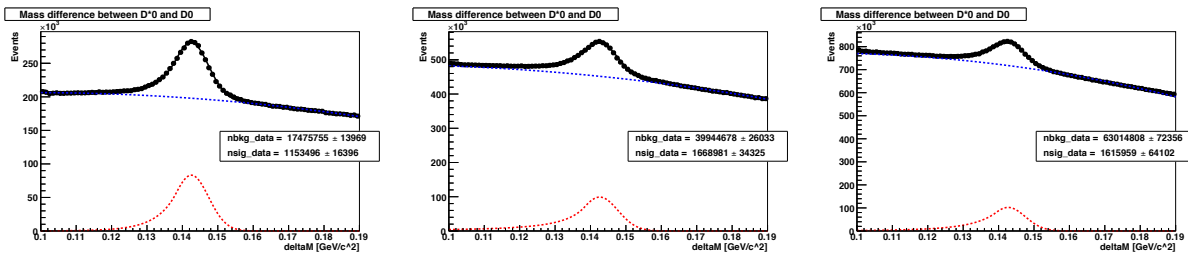


Figure 8.5: The distribution of  $\Delta m$  and fit result of  $D^{*0} \rightarrow D^0 \gamma$  in each mode. Left is  $D^0 \rightarrow K^- \pi^+$ , center is  $D^0 \rightarrow K^- \pi^+ \pi^0$ , and right is  $D^0 \rightarrow K^- \pi^+ \pi^- \pi^+$  mode. Black dots show the data, red line shows the peak component, blue line shows the background, and black line shows the sum of red and blue.

## 8.3 Results for data

### 8.3.1 Reconstruction of $D^{*0}$ and $A'$

Figure 8.6 - 8.8 are the distributions of  $\Delta m$  for data after the  $m_{D^0}$  and  $p_{D^{*0}}$  selections are applied. They also show peaks at  $0.142 \text{ GeV}/c^2$ .

After the  $\Delta m$  selection and other background suppressions described in Sec. 5.4, the invariant mass of the electron and positron candidates are calculated as the mass of  $A'$ ,  $m_{A'}$ . Figure 8.9 - 8.11 show the distributions of  $m_{A'}$  for each decay mode of  $D^0$  for data, together with the MC. The discrepancy between data and MC is due to the limitation in the Belle simulation as mentioned before.

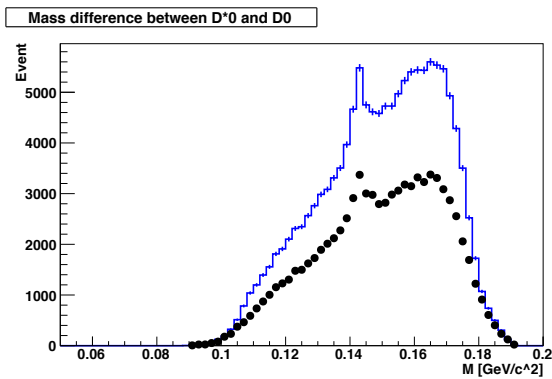


Figure 8.6: The  $\Delta m$  distribution of experimental data and MC in  $D^0 \rightarrow K^- \pi^+ \pi^0$  mode. Black dots show the data and blue histogram shows the MC.

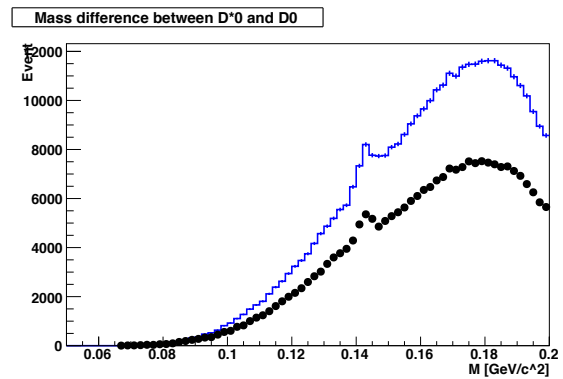


Figure 8.7: The  $\Delta m$  distribution of experimental data and MC in  $D^0 \rightarrow K^- \pi^+ \pi^- \pi^+$  mode. Black dots show the data and blue histogram shows the MC.

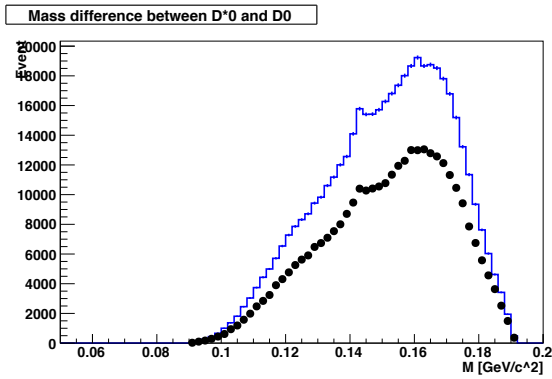


Figure 8.8: The  $\Delta m$  distribution of experimental data and MC in  $D^0 \rightarrow K^- \pi^+ \pi^0$  mode. Black dots show the data and blue histogram shows the MC.

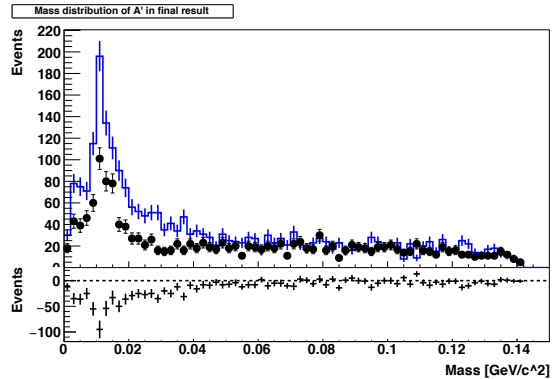


Figure 8.9: The distribution of reconstructed  $m_{A'}$  in  $D^0 \rightarrow K^- \pi^+$  mode. Black dots show the data, blue line shows the MC.

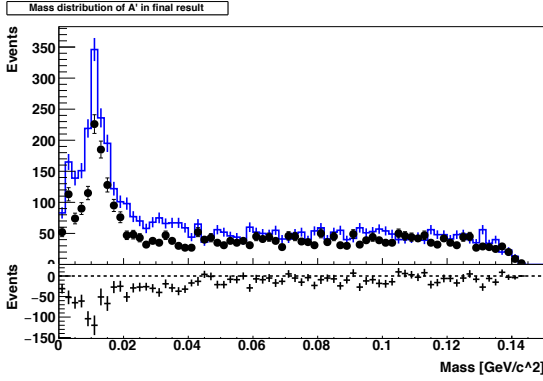


Figure 8.10: The distribution of reconstructed  $m_{A'}$  in  $D^0 \rightarrow K^- \pi^+ \pi^0$  mode. Black dots show the data, blue line shows the MC.

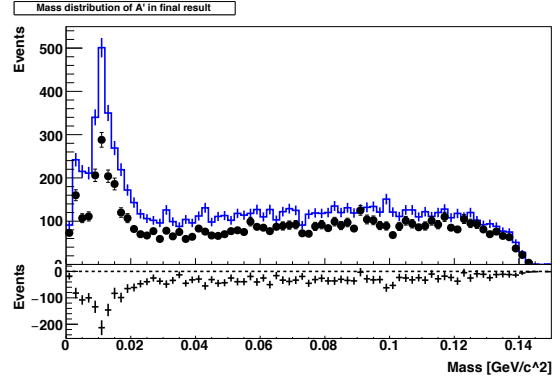


Figure 8.11: The distribution of reconstructed  $m_{A'}$  in  $D^0 \rightarrow K^- \pi^+ \pi^- \pi^+$  mode. Black dots show the data, blue line shows the MC.

### 8.3.2 Result of simultaneous fit to the data

In order to measure the value of  $R$ , a simultaneous fit is performed for three decay modes of  $D^0$ , as discussed in Sec. 6.6. The fit is performed assuming the mass of  $A'$  to be  $17.0 \text{ MeV}/c^2$ . The fixed parameters of the signal functions are listed in table 8.1, which are calculated for  $m_{A'} = 17 \text{ MeV}/c^2$  from table 6.4. The fixed parameters from the normalization mode are summarized in table 8.2. The fit results are shown in Fig. 8.12 - 8.14, and are summarized in Table 8.3.

Table 8.1: The parameters of signal function for  $m_{A'} = 17 \text{ MeV}/c^2$

Mode	Efficiency [%]	$\sigma$ [MeV/ $c^2$ ]	$\sigma_L$ [MeV/ $c^2$ ]	$\sigma_R$ [MeV/ $c^2$ ]	$C_{\text{sig}}$
$D^0 \rightarrow K^- \pi^+$	3.26	0.725	2.07	2.35	0.810
$D^0 \rightarrow K^- \pi^+ \pi^0$	1.11	0.735	2.20	2.43	0.746
$D^0 \rightarrow K^- \pi^+ \pi^- \pi^+$	2.14	0.742	2.46	2.48	0.767

Table 8.2: The summary of constants from the normalization mode

$D^0$ decay mode	$D^0 \rightarrow K^- \pi^+$	$D^0 \rightarrow K^- \pi^+ \pi^0$	$D^0 \rightarrow K^- \pi^+ \pi^- \pi^+$
$N_{D^* \gamma}$	$(11.5 \pm 0.2) \times 10^5$	$(16.7 \pm 0.03) \times 10^5$	$(16.2 \pm 0.6) \times 10^5$
$e_{D^* \gamma}$ [%]	$20.01 \pm 0.02$	$7.51 \pm 0.01$	$13.7 \pm 0.01$
$N_\gamma/e_\gamma$ in total	$(5.76 \pm 0.08) \times 10^6$	$(22.2 \pm 0.5) \times 10^6$	$(11.8 \pm 0.5) \times 10^6$

From the fit, we obtain the ratio  $R$  to be

$$R = (0.7 \pm 3.7) \times 10^{-5}. \quad (8.1)$$

Table 8.3: The summary of fit results. The notations of variables are same as Eq. 6.2.

$D^0$ decay mode	$D^0 \rightarrow K^- \pi^+$	$D^0 \rightarrow K^- \pi^+ \pi^0$	$D^0 \rightarrow K^- \pi^+ \pi^- \pi^+$
$R$	$(0.7 \pm 3.7) \times 10^{-5}$		
$a_0$	$-189.0 \pm 28$	$-235.8 \pm 26$	$-201.6 \pm 24$
$a_1$	$746 \pm 239$	$451 \pm 67$	$622 \pm 107$
$a_2$	$-12204 \pm 2269$	$-10037 \pm 942$	$-12506 \pm 1353$
$a_3$	$89322 \pm 18283$	$97960 \pm 8742$	$127916 \pm 12954$
$a_4$	$-268634 \pm 75564$	$-342446 \pm 32819$	$-481688 \pm 48657$
$C_{\text{bkg}}$	$0.189 \pm 0.021$	$0.159 \pm 0.014$	$0.0953 \pm 0.0094$
$N_{\text{bkg}}$	$1286 \pm 36$	$2744 \pm 53$	$5578 \pm 75$

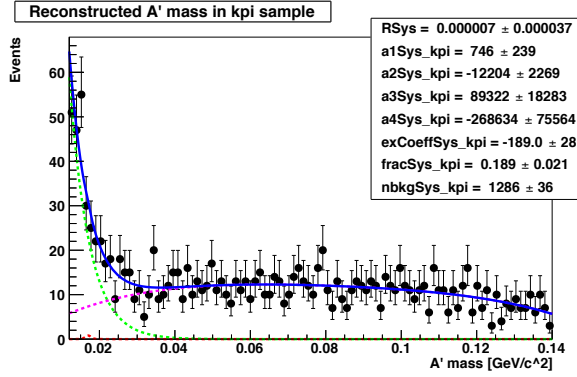


Figure 8.12: The distribution of reconstructed  $m_{A'}$  in  $D^0 \rightarrow K^- \pi^+$  mode. The Red dotted shows the signal yield assuming  $m_{A'} = 17$  MeV. And the green dotted line shows exp component in Eq. 6.3 and the magenta line shows the  $pol4$ .

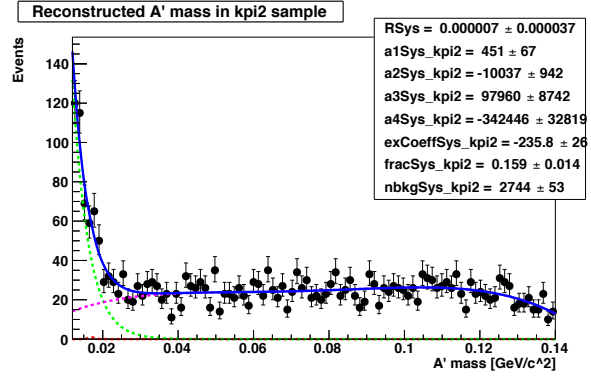


Figure 8.13: The distribution of reconstructed  $m_{A'}$  in  $D^0 \rightarrow K^- \pi^+ \pi^0$  mode. The Red dotted shows the signal yield assuming  $m_{A'} = 17$  MeV. And the green dotted line shows exp component in Eq. 6.3 and the magenta line shows the  $pol4$ .

Since the obtained  $R$  value is consistent with zero, we calculate the upper limit at 90% C.L. Figure 8.15 shows the likelihood distribution  $\mathcal{L}(R)$  from the fit. The upper limit  $R_{ul}$  is defined by

$$\frac{\int_0^{R_{ul}} \mathcal{L}(R) dR}{\int_0^{\infty} \mathcal{L}(R) dR} = 0.9. \quad (8.2)$$

The blue area in Fig. 8.15 shows the numerator and  $R_{ul}$  is the right edge of the area. The upper limit, with statistical error only, is obtained as

$$R < 8.1 \times 10^{-4}. \quad (8.3)$$

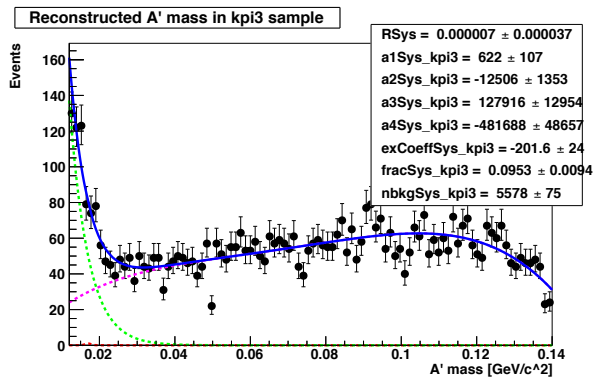


Figure 8.14: The distribution of reconstructed  $m_{A'}$  in  $D^0 \rightarrow K^- \pi^+ \pi^- \pi^+$  mode. The Red dotted shows the signal yield assuming  $m_{A'} = 17$  MeV. And the green dotted line shows exp component in Eq. 6.3 and the magenta line shows the  $pol4$ .

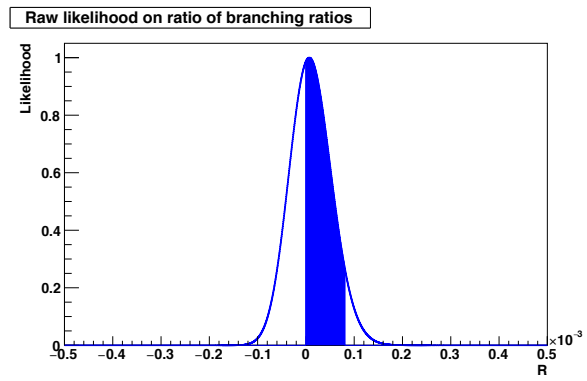


Figure 8.15: The fit likelihood transition as a function of the ratio of branching fractions in the case of  $m_{A'} = 17$  MeV. The blue area shows the 90% of integration from 0 to  $\infty$ .

## 8.4 Upper limit with systematic uncertainties

The systematic uncertainties related to the efficiencies are estimated to be 7.3 % as mentioned in Sec. 7.6

We also have to take into account the uncertainties from the parameters of the fixed signal functions  $f_{\text{sig}}$ . The relevant parameters are  $\sigma, \sigma_L, \sigma_R$ , and  $C_{\text{sig}}$  for each mode shown in table 6.1. We vary each parameter by  $1\sigma$ , perform a fit and obtain the signal yield. The uncertainty of the fit is estimated by the deviation of  $R$  when each parameter is varied.

For example,  $\sigma_L$  for  $K\pi$  mode is fixed to 1.77 MeV in the nominal fit. Fits are repeated varying  $\sigma_L$  by  $\pm 1\sigma$ , i.e. fixing it to 1.83 MeV or 1.71 MeV. In this case, we obtain  $2.8 \times 10^{-5}$  for  $\sigma_L = 1.83$  MeV and  $1.5 \times 10^{-5}$  for  $\sigma_L = 1.71$  MeV, so the deviation of  $R$  from the nominal fit is  $2.8 \times 10^{-5}$  and  $-1.5 \times 10^{-5}$ . We take the largest deviation of  $2.8 \times 10^{-5}$  as the systematic uncertainty for  $\sigma_L$ .

In this way, the systematic uncertainties for all the parameters are evaluated. We take their quadratic sum and regard it as the total systematic uncertainty in the fitting. The summary of the fit systematics for  $m_{A'} = 17$  MeV/ $c^2$  is shown in table 8.4. The systematics uncertainty in the fit is estimated to be  $7.0 \times 10^{-5}$  in total.

Table 8.4: Maximum deviation of  $R$  for  $m_{A'} = 17$  MeV when each parameter is shifted by  $1\sigma$  of its error.

Mode	$\sigma$	$\sigma_L$	$\sigma_R$	$C_{\text{sig}}$	Total
$D^0 \rightarrow K^- \pi^+$	0.0	$3.1 \times 10^{-5}$	$2.2 \times 10^{-6}$	$3.1 \times 10^{-5}$	$4.4 \times 10^{-5}$
$D^0 \rightarrow K^- \pi^+ \pi^0$	0.0	$2.2 \times 10^{-6}$	$3.1 \times 10^{-5}$	$3.2 \times 10^{-6}$	$4.4 \times 10^{-5}$
$D^0 \rightarrow K^- \pi^+ \pi^- \pi^+$	0.0	$2.2 \times 10^{-6}$	$3.1 \times 10^{-6}$	$2.1 \times 10^{-6}$	$3.1 \times 10^{-5}$
Total	0.0	$3.1 \times 10^{-5}$	$4.4 \times 10^{-5}$	$4.5 \times 10^{-6}$	$7.0 \times 10^{-5}$

Finally, taking the quadratic sum of the uncertainty related to the efficiencies and that for the fit, the result of  $R$  for  $m_{A'} = 17$  MeV/ $c^2$  is

$$R = (0.7 \pm 3.7 \pm 7.0) \times 10^{-5}. \quad (8.4)$$

To obtain the upper limit at 90 % C.L., the systematic uncertainties are taken into account by smearing the likelihood distribution by a Gaussian function with  $\mu = R$  and  $\sigma = R \times 7.3\% + \sigma_{\text{fit}}$ , where  $\sigma_{\text{fit}}$  is the systematic uncertainty in the fit. The likelihood distributions for  $m_{A'} = 17$  MeV/ $c^2$  before and after the smearing are shown in Fig. 8.16 and 8.17.

The upper limit with systematic uncertainty is obtained in the same way as shown in Sec. 8.3.2 using the likelihood after the smearing. The final result of  $R$  upper limit for  $m_{A'} = 17$  MeV is

$$R < 1.65 \times 10^{-4}. \quad (8.5)$$

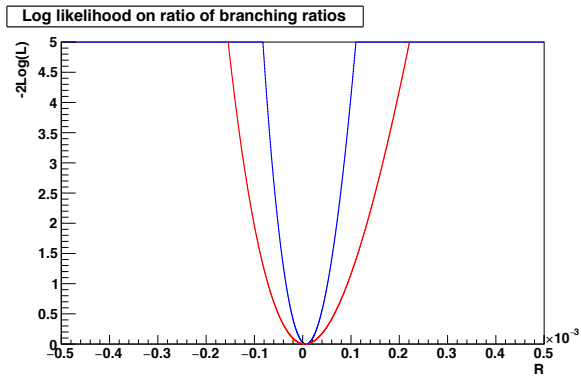


Figure 8.16: The distribution of  $-2\log(L)$  before (blue) and after (red) the smearing.

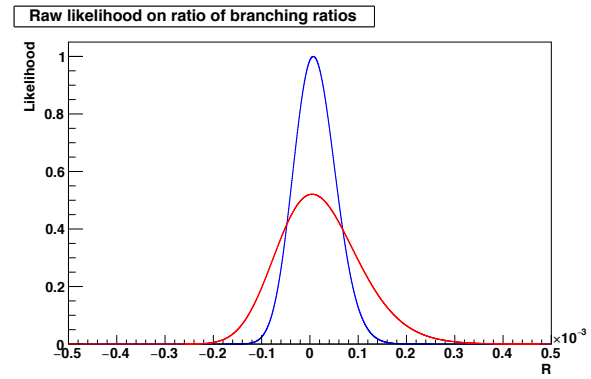


Figure 8.17: The distribution of raw likelihood before (blue) and after (red) the smearing.

# Chapter 9

## Result and discussion

The scan over  $m_{A'}$  is performed from 12 MeV to 120 MeV in Sec. 9.1. Based on the scan result, the mixing between  $D^{*0} \rightarrow D^0 A'$  and  $D^{*0} \rightarrow D^0 \gamma$  is discussed from theoretical aspects via a mixing parameter  $\epsilon$  in Sec. 9.2.

### 9.1 Mass scan for data

The upper limit of the branching ratio for  $m_{A'} = 17$  MeV is derived in the previous chapter. Since the mass of the dark photon is unknown, we need to repeat the same procedure for different  $A'$  masses and scan over  $m_{A'}$ .

We use the same fit function for different  $m_{A'}$  assumption, but the parameters in the fit are varied according to table 6.4. We perform the scan over  $m_{A'}$  in the range between 12 MeV to 120 MeV by 0.5 MeV step. Figure 9.1 shows  $R$  obtained from a fit for different  $m_{A'}$  assumption. Here, the errors are statistical only.

We do not find any significant signal in all the  $m_{A'}$  mass region, so we set upper limits for each  $m_{A'}$ . In this procedure, the systematic uncertainties are also calculated for each  $m_{A'}$  in the same way as Chap. 7 and Sec. 8.4. Figure 9.2 shows the fit systematics are evaluated for the scan region  $12 < m_{A'} < 120$  MeV. Figure 9.3 shows the upper limit of  $R$  without and with the systematic uncertainty for each  $m_{A'}$ .

The final result of  $R$  is in Fig. 9.4.

### 9.2 Discussion

Assuming kinetic mixing, the relation between  $R$  and the mixing parameter  $\epsilon$  can be written as

$$R = \epsilon^2 \left( 1 - \frac{m_{A'}^2}{\Delta m^2} \right) \quad (9.1)$$

where  $\Delta m$  is the mass difference between  $D^{*0}$  and  $D^0$ , 142 MeV. From this relation, we obtain the upper limit on  $\epsilon$  as shown in Fig. 9.5.

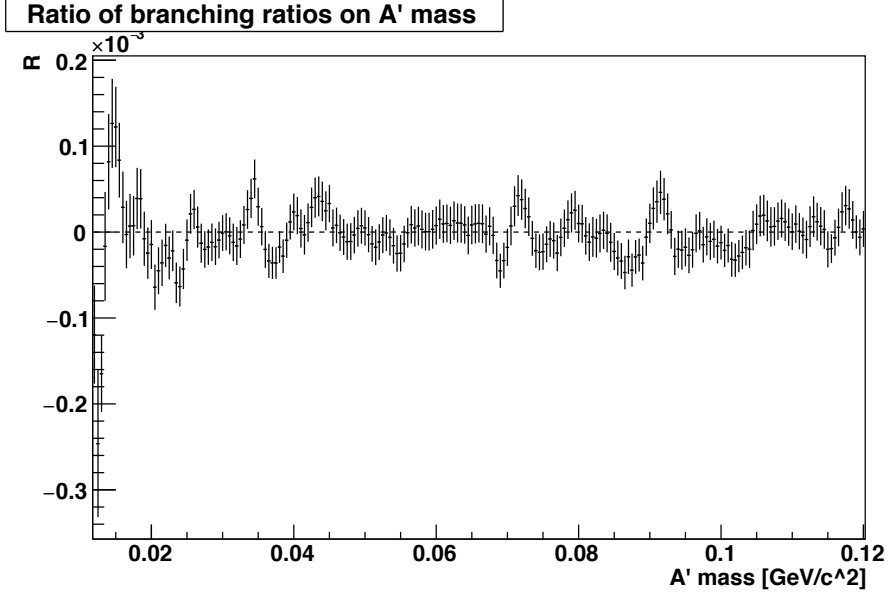


Figure 9.1: The ratio of branching ratios vs  $m_{A'}$  obtained from the simultaneous fit.

The previous search results shown in Fig. 2.5 are also obtained with the kinetic mixing assumption. Assuming the kinetic mixing, our limit on  $\epsilon$  is above the current limit and consistent with the previous results. For  $X(17)$  with  $R = 5.8 \times 10^{-6}$  mentioned in Sec. 2.4, the upper limit obtained in Eq. 8.5 is above the previous result.

However, our result is obtained for the coupling only to charm flavour, and if the coupling of Dark Photon is different among flavors, it gives a strong limit to the model. For example, J.L. Feng et al. discussed different  $\epsilon$  for each quark flavour [82]. Considering the mixing of  $A'$  with SM photon, Dark Photon is a particle with  $J^P = 1^-$  vector. The new vector couples to a current  $J_{A'}^\mu$ , which is a linear combination of the SM fermion currents,

$$\mathcal{L} \supset iA'^\mu J_{A'}^\mu = iA'_\mu \sum_{i=\text{fermions}} \epsilon_i e J_i^\mu, \quad (9.2)$$

$$J_i^\mu = \bar{f}_i \gamma^\mu f_i. \quad (9.3)$$

In this hypothesis,  $\epsilon_i$  can be different for couplings to each fermion and Eq. 9.1 becomes

$$R = \epsilon_c^2 \left(1 - \frac{m_{A'}^2}{\Delta m^2}\right) \quad (9.4)$$

and, using our limit on  $R$  in Sec. 8.4, the  $\epsilon_c$  for  $m_{A'} = 17 \text{ MeV}/c^2$  is obtained to be

$$\epsilon_c < 9.2 \times 10^{-3} \quad (9.5)$$

The most stringent upper limit on  $\epsilon$  at  $m_{A'} = 17 \text{ MeV}/c^2$  is given by NA48/2. Since this result is obtained using the decay of  $\pi \rightarrow \gamma(A' \rightarrow e^+e^-)$  which couples only with  $u$  and  $d$

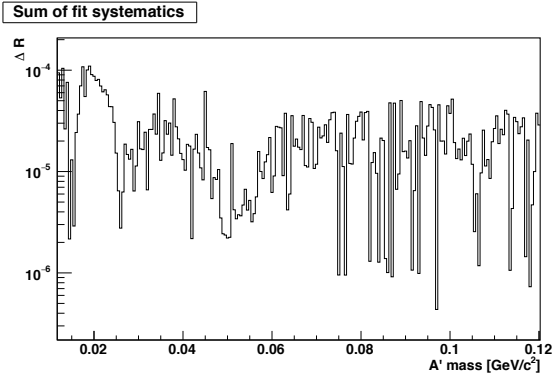


Figure 9.2: The fit systematics as a function of  $m_{A'}$ .

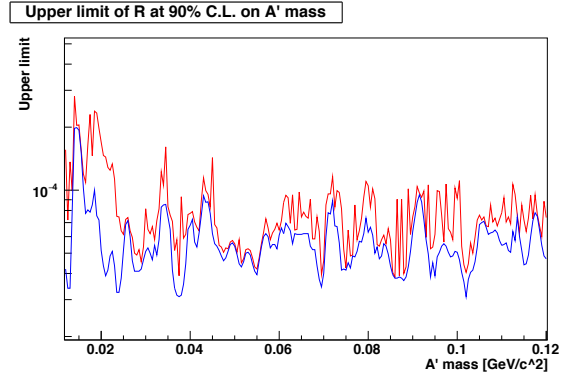


Figure 9.3: The upper limits of  $R$  obtained from the likelihood before (blue) and after (red) the smearing.

quarks, the upper limit to the coupling  $(2\epsilon_u + \epsilon_d)$  can be given as [82]

$$|2\epsilon_u + \epsilon_d| = |\epsilon_p| \lesssim \frac{0.8 - 1.2 \times 10^{-3}}{\sqrt{\text{BR}(X \rightarrow e^+e^-)}}. \quad (9.6)$$

The second most stringent upper limit on  $\epsilon$  given by BaBar is for  $e$  obtained as [82]

$$|\epsilon_e| \lesssim \frac{2 \times 10^{-3}}{\sqrt{\text{BR}(X \rightarrow e^+e^-)}}. \quad (9.7)$$

However, there are no measurements focused on the coupling to charm and this analysis give the first limit on the mixing parameter for charm.

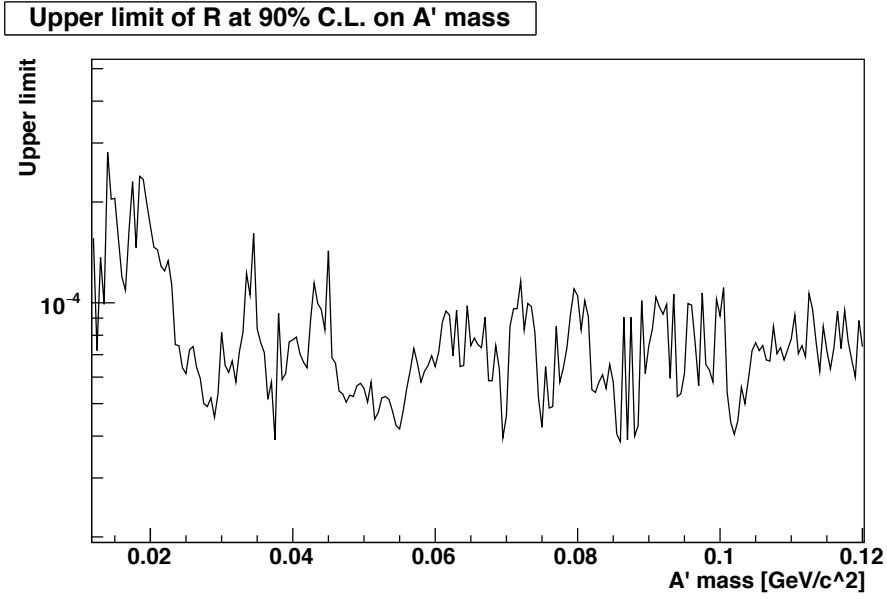


Figure 9.4: The upper limit of  $R$  at 90 % C.L. vs  $m_{A'}$  obtained from the simultaneous fit.

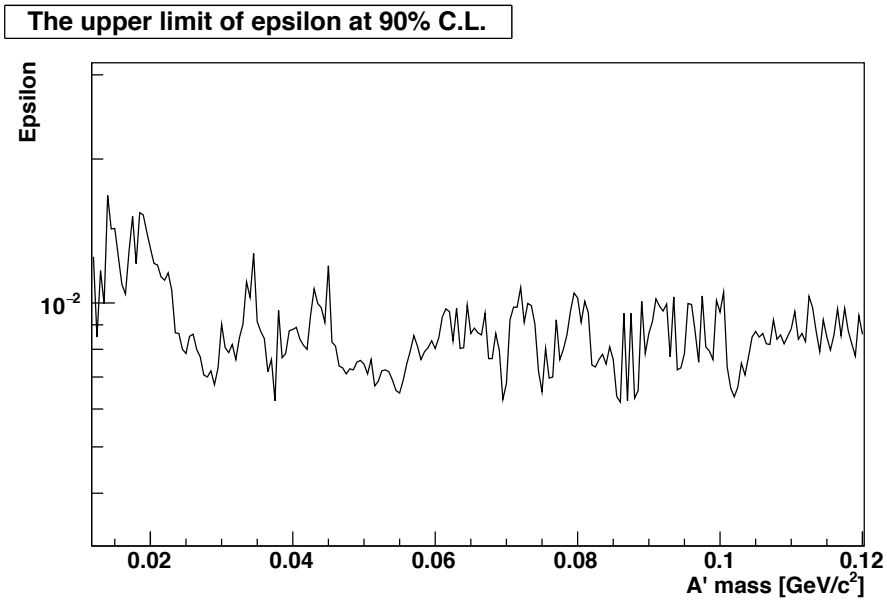


Figure 9.5: The upper limit of  $\epsilon$  at 90 % C.L. vs  $m_{A'}$  obtained from the simultaneous fit.

# Chapter 10

## Conclusion

We search for Dark Photon  $A'$  in the data sample of  $711 \text{ fb}^{-1}$  accumulated by the Belle spectrometer.

The target decay is  $D^{*0} \rightarrow D^0 A' (\rightarrow e^+ e^-)$  with  $D^0$  decays  $D^0 \rightarrow K^- \pi^+$ ,  $K^- \pi^+ \pi^0$  and  $K^- \pi^+ \pi^- \pi^+$ . Since the decay of  $D^{*0} \rightarrow D^0 A'$  is expected to occur by a mixing with the Standard Model process  $D^{*0} \rightarrow D^0 \gamma$ , we conduct the measurement of  $R = \text{B}(D^{*0} \rightarrow D^0 A') / \text{B}(D^{*0} \rightarrow D^0 \gamma)$ .

We determine the parameters for background suppression, optimize the selection criteria and formulate fit functions for signal and background distributions of the reconstructed  $m_{A'}$  using MC simulation. The fitting procedure is confirmed to be unbiased by the study using Toy MC. The value of  $R$  is determined by the simultaneous fit to the  $m_{A'}$  distributions for three  $D^0$  sub decay modes. To combine the three sub decay modes of  $D^0$ , the  $m_{A'}$  distributions of the three modes are fitted simultaneously using  $R$  as a common parameter.

The  $R$  is first measured assuming the  $A'$  mass is  $17 \text{ MeV}/c^2$  and obtained

$$R = (0.7 \pm 3.7 \pm 7.0) \times 10^{-5} \quad (10.1)$$

which is consistent with 0 and the existence of  $X(17)$  is not confirmed. The upper limit at 90 % C.L. in  $R$  is set at

$$R < 1.65 \times 10^{-4}. \quad (10.2)$$

The result is consistent with the other measurements that searched for  $A'$ .

We also perform a mass scan in the range  $12 < m_{A'} < 120 \text{ MeV}/c^2$  at a  $0.5 \text{ MeV}/c^2$  step. No signal event is observed in the low mass region and the upper limits are set on  $R$ .

Although the upper limit obtained in this analysis do not update those of previous results, this is the first search of Dark Photon using  $D^{*0}$  in this mass region. Therefore, this is the first search of Dark Photon which couples with  $c$  quark. Since the coupling of Dark Photon can be different among quark flavours, this analysis gives a new and important result for the Dark Photon search.

# Acknowledgement

First of all, I would like to express my gratitude to the supervisor Prof. Ryosuke Itoh for giving me an opportunity to be involved high energy physics. Thanks to his encouragement and advice, I got in the Belle and Belle II experiment and learnt many skills including hardware, software and computing techniques which are not only related to this analysis but also important for in many aspects. I also appreciate the supervisor Prof. Shohei Nishida who gives lots of supports and detailed advice not only for the analysis but also for the fundamentals of research.

This research was achieved by many helps from collaborators of the Belle experiment. I am especially thankful to timely reviewing and detailed feedback by my internal referees Dr. Alexander S. Kuzmin, Dr. Seokhee Park and Dr. Sven Vahsen; useful ideas and comments by Dr. Gianluca Inguglia, Dr. Igal Jaegle and the members of Belle dark sector group.

In my research for the performance evaluation of ARICH detector, discussions and helps with Dr. Luka Santelj, Dr. Tomoyuki Konno and the members of Belle II ARICH group are essential for me to complete the evaluation. In the development of the data quality monitor, the technical supports by Dr. Boqun Wang and feedbacks from Belle II DQM group much helped me.

Finally, I acknowledge the secretaries of SOKENDAI, especially Ms. Noriko Yamamura for much support regarding to administration and so on. Their support was significantly important for me to concentrate on and proceed my research smoothly.

Last but not least, I would like to express my sincere thanks to my family for the love, support and constant encouragement I have received throughout my life.

# Appendix A

## Appendix

### A.1 Efficiency of charged particle selection

After the selection, the selection efficiency is evaluated by comparing the identification and the MC truth. The efficiency  $e_{particle}$  is the fraction of the number of tracks generated in the MC  $N_{gen}$  and the number of tracks which are identified as the particle and whose MC truth matche the identified particle  $N_{id}$ .

$$e_{particle} = \frac{N_{id}}{N_{gen}} \quad (\text{A.1})$$

For kaon as an example,  $N_{gen}$  is the number of all generated kaon in MC not only from signal decay but also from the other sub products of  $c\bar{c}$ . And  $N_{id}$  is the number of tracks which are identified as a kaon and whose MC truth is kaon, too. Note that it is including not only PID efficiency but also tracking efficiency

The efficiency of the particle candidate selection described above is summarized in table (A.1).

Final state particle	Track efficiency in $D^0 \rightarrow K^\mp \pi^\pm$ mode	Track efficiency in $D^0 \rightarrow K^\mp \pi^\pm \pi^0$ mode	Track efficiency in $D^0 \rightarrow K^\mp \pi^\pm \pi^\mp \pi^\pm$ mode
Charged $K$	69.9%	68.7%	66.2%
Charged $\pi$	79.5%	79.0%	76.5%
$e$	40.6%	40.3%	38.7%

Table A.1: The track efficiencies of the final state particles by PID and impact parameters.

### A.2 The PDF of $D^{*0} \rightarrow D^0 e^+ e^-$ mode

The decay can be described by the matrix element of  $D^{*0} \rightarrow D^0 \gamma$ ;

$$\mathcal{M} = g \epsilon^{\mu\nu\alpha\beta} \epsilon^{D\mu} \epsilon^{g*\nu} p_\alpha k_\beta F(k^2) \quad (\text{A.2})$$

where  $g$  is a constant to describe  $D^*$  decay,  $\epsilon^{\mu\nu\alpha\beta}$  is a symmetric tensor,  $\epsilon^{D\mu}$  and  $\epsilon^{g^*\nu}$  are polarization vectors of  $D^{*0}$  and  $\gamma$ ,  $p^\alpha$  and  $k^\beta$  are the four momentum of  $D^{*0}$  and  $\gamma$ , and  $F(k^2)$  is form factor of  $D^{*0}$  which is considered  $F(k^2) = 1$  for small  $k^2$ , respectively. For  $D^{*0} \rightarrow D^0 e^+ e^-$  process, a virtual photon decays into  $e^+ e^-$  pair. So, the matrix element is

$$\mathcal{M} = g \epsilon^{\mu\nu\alpha\beta} \epsilon^{D\mu} p_\alpha k_\beta g_{\nu\rho} \frac{1}{q^2} e \bar{v}(p_+) \gamma_\rho u(p_-) \quad (\text{A.3})$$

where  $g_{\nu\rho}$  is a metric tensor,  $q^2$  is four momentum of the virtual photon,  $e$  is the electric charge of electron,  $\gamma_\rho$  is the gamma matrices, and  $\bar{v}(p_+)$  and  $u(p_-)$  are four spinor of  $e^+$  and  $e^-$ . Then, averaging the  $D^{*0}$  polarization, the branching fraction is derived as a function of  $q^2$  and the helicity angle  $\theta$ ;

$$\frac{p_{ee}^2}{q^4} \left( \left( \frac{q^2}{4} + m_e^2 \right) + \left( \frac{q^2}{4} - m_e^2 \right) \cos^2 \theta \right) \quad (\text{A.4})$$

where  $p_{ee}$  is 3-momentum of electron-positron pair,  $q$  is the momentum transfer,  $m_e$  is the electron mass, and  $\theta$  is helicity angle of  $ee$  system to  $D^{*0}$ . Finally, the branching fraction is integrated over the phase space, the distribution of probability density function used in generation is shown in Fig. A.1.

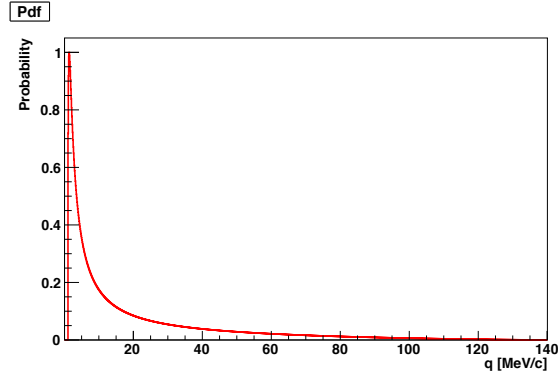


Figure A.1: The pdf for  $D^{*0} \rightarrow D^0 e^+ e^-$  decay model.

# Bibliography

- [1] J. H. Oort, “The force exerted by the stellar system in the direction perpendicular to the galactic plane and some related problems”, *Bull. Astron. Inst. Netherlands*, vol. 6, p. 249, 1932.
- [2] F. Zwicky, “Die Rotverschiebung von extragalaktischen Nebeln”, *Helvetica Physica Acta*, vol. 6, p. 110, 1933.
- [3] F. Zwicky, “On the Masses of Nebulae and of Clusters of Nebulae”, *Astrophys. J.*, vol. 86, p. 217, 1937.
- [4] V. C. Rubin, W. K. Ford Jr., and N. Thonnard, “Rotational properties of 21 SC galaxies with a large range of luminosities and radii, from NGC 4605 (R=4kpc) to UGC 2885 (R=122kpc)”, *Astrophys. J.*, vol. 238, p. 471, 1980.
- [5] F. Kahlhoefer, “Review of LHC dark matter searches”, *Int. J. Mod. Phys. A*, vol. 32, p. 1730006, 2017.
- [6] M. Campajola, *Dark Matter searches at Belle II*, Talk presented at CNNP2020, 2020, Cape Town.
- [7] R. Bernabei et al., “First model independent results from DAMA/LIBRA-phase2”, *Nucl. Phys. At. Energy*, vol. 19, p. 307, 2018.
- [8] E. Aprile et al., “Dark Matter Results from 225 Live Days of XENON100 Data”, *Phys. Rev. Lett.*, vol. 109, 2012.
- [9] R. Agnese et al., “Search for Low-Mass Weakly Interacting Massive Particles with SuperCDMS”, *Phys. Rev. Lett.*, vol. 112, p. 241302, 2014.
- [10] A. J. Krasznahorkay et al., “Observation of Anomalous Internal Pair Creation in  $^8\text{Be}$ : A Possible Indication of a Light, Neutral Boson”, *Phys. Rev. Lett.*, vol. 116, p. 042501, 2016.
- [11] J. R. Batley et al. (NA48/2 Collaboration), “Search for the dark photon in  $\pi^0$  decays”, *Phys. Lett. B*, vol. 746, p. 178, 2015.
- [12] ATLAS Collaboration, “Observation of a new particle in the search for the Standard Model Higgs boson with the ATLAS detector at the LHC”, *Phys. Lett. B*, vol. 716, p. 1, 2012.
- [13] CMS Collaboration, “Observation of a new boson at a mass of 125 GeV with the CMS experiment at the LHC”, *Phys. Lett. B*, vol. 716, p. 30, 2012.

- [14] Y. Fukuda et al. (Super-Kamiokande Collaboration), “Evidence for Oscillation of Atmospheric Neutrinos”, *Phys. Rev. Lett.*, vol. 81, p. 1562, 1998.
- [15] A. D. Sakharov, “Violation of CP in variance, C asymmetry, and baryon asymmetry of the universe”, *J. Exp. Theor. Phys.*, vol. 5, p. 24, 1967.
- [16] M. Kobayashi and T. Maskawa, “CP-Violation in the Renormalizable Theory of Weak Interaction”, *Prog. Theor. Phys.*, vol. 49, p. 652, 1973.
- [17] J. R. Primack and M. A. K. Gross, “Hot Dark Matter in Cosmology. In: Caldwell D.O. (eds) Current Aspects of Neutrino Physics”, in. Springer, 2001.
- [18] N. Jarosik et al., “Seven-Year Wilkinson Microwave Anisotropy Probe (WMAP) Observations: Sky Maps, Systematic Errors, and Basic Results”, *Astrophys. J., Suppl. Ser.*, vol. 192, p. 14, 2011.
- [19] M. Tegmark, A. de Oliveira-Costa, and A. J. S. Hamilton, “High resolution foreground cleaned CMB map from WMAP”, *Phys. Rev. D*, vol. 68, p. 123 523, 2003.
- [20] P. Fayet, “Spontaneously broken supersymmetric theories of weak, electromagnetic and strong interactions”, *Phys. Lett. B*, vol. 69, p. 489, 1977.
- [21] X. C. Vidal and R. C. Manzano, *Supersymmetry, Taking a closer look at LHC*. [Online]. Available: [https://www.lhc-closer.es/taking\\_a\\_closer\\_look\\_at\\_lhc/0.supersymmetry](https://www.lhc-closer.es/taking_a_closer_look_at_lhc/0.supersymmetry).
- [22] R. D. Peccei and H. R. Quinn, “CP Conservation in the Presence of Pseudoparticles”, *Phys. Rev. Lett.*, vol. 38, p. 1440, 1977.
- [23] T. D. Lee and C. N. Yang, “Question of Parity Conservation in Weak Interactions”, *Phys. Rev.*, vol. 104, p. 254, 1956.
- [24] B. S. Acharya, A. Maharana, and F. Muia, “Hidden Sectors in String Theory: Kinetic Mixings, Fifth Forces and Quintessence”, *J. High Energy Phys.*, vol. 2019, p. 48, 2019.
- [25] K. Petraki and R. R. Volkas, “Review of asymmetric dark matter”, *Int. J. Mod. Phys. A*, vol. 28, p. 1 330 028, 2013.
- [26] B. Holdom, “Two U(1)’s and  $\epsilon$  charge shifts”, *Phys. Lett. B*, vol. 166, p. 196, 1986.
- [27] N. Arkani-Hamed and N. Weiner, “LHC signals for a SuperUnified theory of Dark Matter”, *J. High Energy Phys.*, vol. 2008, p. 104, 2008.
- [28] R. Essig, P. Schuster, and N. Toro, “Probing dark forces and light hidden sectors at low-energy  $e^+e^-$  colliders”, *Phys. Rev. D*, vol. 80, p. 015 003, 2009.
- [29] M. Goodsell et al., “Naturally light hidden photons in LARGE volume string compactifications”, *J. High Energy Phys.*, vol. 2009, p. 27, 2009.
- [30] A. Prateek et al., “Relic abundance of dark photon dark matter”, *Phys. Lett. B*, vol. 801, p. 135 136, 2020.
- [31] R. Aaij et al. (LHCb collaboration), “Search for  $A' \rightarrow \mu^+\mu^-$  Decays”, *Phys. Rev. Lett.*, vol. 124, p. 041 801, 2020.

- [32] A. Bross et al., “Search for short-lived particles produced in an electron beam dump”, *Phys. Rev. Lett.*, vol. 67, p. 2942, 1991.
- [33] D. Banerjee et al. (NA64 Collaboration), “Search for a Hypothetical 16.7 MeV Gauge Boson and Dark Photons in the NA64 Experiment at CERN”, *Phys. Rev. Lett.*, vol. 120, p. 231 802, 2018.
- [34] E. M. Riordan et al., “Search for short-lived axions in an electron-beam-dump experiment”, *Phys. Rev. Lett.*, vol. 59, p. 755, 1987.
- [35] A. Konaka et al., “Search for Neutral Particles in Electron-Beam-Dump Experiment”, *Phys. Rev. Lett.*, vol. 57, p. 659, 1986.
- [36] M. Davier and N. H. Nguyen, “An unambiguous search for a light Higgs boson”, *Phys. Lett. B*, vol. 229, p. 150, 1989.
- [37] G. Bernardi et al., “Search for neutrino decay”, *Phys. Lett. B*, vol. 166, p. 479, 1986.
- [38] P. Astier et al., “Search for heavy neutrinos mixing with tau neutrinos”, *Phys. Lett. B*, vol. 506, p. 27, 2001.
- [39] J. Blumlein et al., “Limits on neutral light scalar and pseudoscalar particles in a proton beam dump experiment”, *Z. Phys. C*, vol. 51, p. 341, 1991.
- [40] J. Blumlein et al., “Limits on the mass of light (pseudo)scalar particles from Bethe-Heitler  $e^+ e^-$  and  $\mu^+ \mu^-$  pair production in a proton - iron beam dump experiment”, *Int. J. Mod. Phys. A*, vol. 7, p. 3835, 1992.
- [41] F. Bergsma et al., “Search for axion-like particle production in 400 GeV proton-copper interactions”, *Phys. Lett. B*, vol. 157, p. 458, 1985.
- [42] J. D. Bjorken et al., “Search for neutral metastable penetrating particles produced in the SLAC beam dump”, *Phys. Rev. D*, vol. 38, p. 3375, 1988.
- [43] M. Pospelov, “Secluded U(1) below the weak scale”, *Phys. Rev. D*, vol. 80, p. 095 002, 2009.
- [44] J. P. Lees et al. (BaBar Collaboration), “Search for a Dark Photon in  $e^+e^-$  Collisions at BaBar”, *Phys. Rev. Lett.*, vol. 113, p. 201 801, 2014.
- [45] F. Archilli et al. (KLOE collaboration), “Search for a vector gauge boson in  $\phi$  meson decays with the KLOE detector”, *Phys. Lett. B*, vol. 706, p. 251, 2012.
- [46] A. Anastasi et al. (KLOE collaboration), “Limit on the production of a new vector boson in  $e^+e^- \rightarrow U\gamma$ ,  $U \rightarrow \pi^+\pi^-$  with the KLOE experiment”, *Phys. Lett. B*, vol. 757, p. 356, 2016.
- [47] P. Ilten et al., “Serendipity in dark photon searches”, *J. High Energy Phys.*, vol. 2018, p. 4, 2018.
- [48] I. W. Stewart, “Extraction of the  $D^*D\pi$  coupling from  $D^*$  decays”, *Nucl. Phys. B.*, vol. 529, p. 62, 1998.
- [49] S. Bethke, “The 2009 world average of  $\alpha_s$ ”, *Eur. Phys. J. C*, vol. 64, p. 689, 2009.

- [50] S. Kurokawa and E. Kikutani, “Overview of the KEKB accelerators”, *Nucl. Instrum. Methods Phys. A*, vol. 499, p. 1, 2003, and other papers included in this Volume.
- [51] T. Abe et al., “Achievements of KEKB”, *Prog. Theor. Exp. Phys.*, vol. 2013, 03A001, 2013, and references therein.
- [52] N. Toge, “KEKB B-factory design report”, National Laboratory for High Energy Physics (KEK), Tech. Rep., 1995.
- [53] I. Abe et al., “The KEKB injector linac”, *Nucl. Instrum. Methods Phys. A*, vol. 499, p. 167, 2003.
- [54] A. Abashian et al., “The Belle detector”, *Nucl. Instrum. Methods Phys. A*, vol. 479, p. 117, 2002, Detectors for Asymmetric B-factories.
- [55] A. Abashian et al., “The  $K_L/\mu$  detector subsystem for the BELLE experiment at the KEK B-factory”, *Nucl. Instrum. Methods Phys. A*, vol. 449, p. 112, 2000.
- [56] H. Nakayama, “Precision measurement of the electroweak flavor-changing neutral current decays of B mesons”, Ph.D. dissertation, University of Tokyo, 2010.
- [57] T. Kuhr et al., “The Belle II Core Software”, *Comput. Softw. Big Sci.*, vol. 3, p. 1, 2019.
- [58] Belle tracking group, “Charged Particle Tracking in Belle”, Belle Note 327, 2000.
- [59] R. O. Duda and P. E. Hart, “Use of the Hough Transformation to Detect Lines and Curves in Pictures”, *Commun. ACM*, vol. 15, p. 11, 1972.
- [60] R. Fruehwirth, “Application of Kalman filtering to track and vertex fitting”, *Nucl. Instrum. Methods Phys. A*, vol. 262, p. 444, 1987.
- [61] S. Suzuki, “CDC cathode clustering and track matching”, Belle Note 246, 1998.
- [62] R. Harr, “Calculation of track and vertex errors for detector design studies”, *IEEE Trans. Nucl. Sci.*, vol. 42, p. 134, 1995.
- [63] S. Nagayama, “Monte Carlo study of ECL performance”, Belle Note 37, 1994.
- [64] E. Nakano, “Belle PID”, *Nucl. Instrum. Methods Phys. A*, vol. 494, p. 402, 2002.
- [65] K. Hanagaki et al., “Electron identification in Belle”, *Nucl. Instrum. Methods Phys. A*, vol. 485, p. 490, 2002.
- [66] B. Casey, “HadronB”, Belle Note 390, 2001.
- [67] B. Casey, “Measurement of the Number of  $B\bar{B}$  Events in Experiment 5 Data and the  $B\bar{B}$  Cross Section at KEKB”, Belle Note 296, 2000.
- [68] D. J. Lange, “The EvtGen particle decay simulation package”, *Nucl. Instrum. Methods Phys. A*, vol. 462, p. 152, 2001.
- [69] T. Sjostrand, S. Mrenna, and P. Skands, “PYTHIA 6.4 physics and manual”, *J. High Energy Phys.*, vol. 2006, p. 026, 2006.
- [70] R. Brun et al., “Geant3”, Preprint CERN DD/EE/84-1, CERN, 1987.

- [71] Particle Data Group, “Review of Particle Physics”, *Prog. Theor. Exp. Phys.*, vol. 2020, 2020.
- [72] S. Andreas, “Light Weakly Interacting Particles: Constraints and Connection to Dark Matter”, Ph.D. dissertation, Universität Hamburg, 2013.
- [73] G. Punzi, “Sensitivity of searches for new signals and its optimization”, *Proc. PHYSTAT2003*, 2003.
- [74] P. Avery, “Applied Fitting Theory VI: Formulas for Kinematic Fitting”, *CLEO Note CBX*, vol. 98, no. 37, 1998.
- [75] W. Verkerke and D. Kirkby, *The RooFit toolkit for data modeling*, arXiv:physics/0306116, 2003.
- [76] T. Aushev, “Study of  $\pi_{slow}^-$  efficiency using  $B^0 \rightarrow D^{*-}\pi^+$  decay”, Belle Note 480, 2002.
- [77] L. Hinz, “Lepton ID efficiency correction and systematic error”, Belle Note 954, 2006.
- [78] H. W. Kim, “Photon detection efficiency using radiative Bhabha sample”, Belle Note 499, 2002.
- [79] A. Matyja and M. RoSanska, “Search for  $B^0 \rightarrow D^{*-}\tau^+\nu\tau$  decay at Belle”, Belle Note 923, 2007.
- [80] M. Staric, “Measurement of  $y_{CP}$  in  $D^0 \rightarrow K^+K^-, \pi^+\pi^-$ ”, Belle Note 945, 2007.
- [81] K. Arinstein, S. Eidelman, and A. Kuzmin, “Measurement of the ratio  $\mathcal{B}(D^0 \rightarrow \pi^+\pi^-\pi^0) / \mathcal{B}(D^0 \rightarrow K^-\pi^+\pi^0)$  and the time-integrated asymmetry in  $D^0 \rightarrow \pi^+\pi^-\pi^0$ ”, Belle Note 947, 2007.
- [82] J. L. Feng et al., “Protophobic Fifth-Force Interpretation of the Observed Anomaly in  $Be^8$  Nuclear Transitions”, *Phys. Rev. Lett.*, vol. 117, p. 071 803, 2016.